Edge Preserving Image Reconstruction: Experimental Applications to Thoracic EIT

by

Peyman Rahmati

Thesis submitted to the
Faculty of Graduate Studies and Research
In partial fulfillment of the requirements
For the degree of Doctor of Philosophy in
Electrical Engineering

Ottawa-Carleton Institute for Electrical and Computer Engineering
Department of Systems and Computer Engineering
Faculty of Engineering
Carleton University

Abstract

Tomographic image reconstruction is an inverse problem, where unknown parameters describing an internal volume are estimated from a set of known measurements (observations). Tomographic images are increasingly used in diagnostic applications in medicine and other industries, such as seismology and non-destructive testing. In many biomedical applications, the underlying anatomy contains sharp interfaces between the different organs and tissue types. Classical linear formulations of tomographic image reconstruction tend to smooth these sharp interfaces and produce blurred, low contrast images. Alternatives to these linear image reconstruction algorithms are edge-preserving image reconstruction methods (EPIRM) which preserve the sharp interfaces by non-linear parameterizations.

The main aim of this thesis is to develop novel EPIRMs applied to reconstruct high contrast, edge-preserving images which are robust against noise and data outliers. This thesis proposes three novel variants of the EPIRM and evaluates the robustness of the proposed EPIRMs against measurement errors.

To show the implementation of the proposed EPIRMs, Electrical Impedance Tomography (EIT) as an instance of ill-posed, non-linear inverse problem is applied. It is desirable to have a reconstruction algorithm with sharp image and low vulnerability to spatial noise and data outliers, which are common measurement errors caused due to patient movement, sweating, and loose electrode connections, in clinical applications of EIT. This thesis investigates the first experimental results of applying difference EIT to produce EIT lung images for lung healthy and lung unhealthy patients. According to our clinical results for EIT lung data, the proposed EPIRMs offer sharper, lower noise and artifact lung image when compared with the competing methods. The proposed EPIRMs reconstruct changes in the lung volume during inhalation and exhalation cycles so that the shape of the venti-

lated regions inside the lungs alters, in accordance with the lung volume for a mechanically ventilated patient, from one time frame to another.

This thesis proposes an evaluation framework to qualitatively and quantitatively compare the performance of four competing methods (iterative Gauss-Newton (GN) with Tikhonov regularization term, GN with NOSER algorithm, Total Variation (TV), and the L1 norm based inverse problem solved using the Primal-Dual Interior Point Method (hereinafter referred to as the PDIPM) against that of the proposed EPIRMs over EIT simulated data. The simulation results show that the proposed EPIRMs offer the highest accuracy in the reconstruction of two low conductive inclusions with an overall average accuracy score of 2.57 (out of 3), vs. 1.78 for TV as the second best performing method. Moreover, the results show that the proposed EPIRM with the sum of absolute values (L1 norm) on the image and data terms of the inverse problem offers the highest robustness against measurement errors with an average robustness score of 3 (out of 3), averaged over three different measurement conditions. The PDIPM with the L1 norms on its inverse problem terms offers an average robustness score of 1.33 and is the second robust method in dealing with the uncertainties.

Acknowledgements

This thesis is the result of four years endeavour and diligence to create high quality research work and has not been possible without the support and encouragement of many people including my supervisor, colleagues, friends, and family. First and foremost, it is with immense gratitude that I acknowledge the support, guidance, and help of my supervisor Prof. Andy Adler, who continually and convincingly conveyed a spirit of adventure in regard to my research. I wholeheartedly appreciate his insight, creativity and friendship that have been the inspiration to complete this thesis. Thank you for trusting me. For the past four years that I have been working in his research lab, I have had the chance to work on several interesting research projects that I learned a lot from. I hope to continue work with him in near future.

I would like to thank my committee members Dr. Miodrag Bolic, Dr. Abijit Sarkar, Dr. Oliver Dorn, and Dr. Yu Ono for their constructive criticisms and helpful comments on this thesis. This list is incomplete without acknowledging Dr. Monique Frize, who wholeheartedly shared many experiences with us in the class and taught me how to present my research, Dr. Richard Dansereau who gave me the opportunity to give short lectures to his undergraduate students in his lab sessions and shared with me many life experiences, Dr. Doron Nussbaum who challenged me to become better in presenting my research and taught me advanced algorithms related to medical computing , Dr. James Green who is bestowed with a great smile and taught me many exciting topics regarding pattern recognition and classification, and again Dr. Yu Ono who is a great teacher and taught me how different imaging modalities function. I am indebted to all of you and I feel fortunate that I have had the chance to get to know you and learn from you.

It is my fortune to gratefully acknowledge the support of a warm hearted friend and

colleague Mr. David Dowson. I have been always inspired by David's passion, and diligence in conducting a research project. I have had the pleasure to work with David on a research project and found that he is a true gentleman who has been bestowed with a great source of perseverance and wisdom. He generously offered to help proofread this thesis. Thank you, David. Many thanks are due to a real friend Elizabeth (Libby) Sprigge who wholeheartedly proofread this thesis several times and helped format the entire thesis.

I would like to acknowledge Dr. Manuch Soleimani who has directly contributed to this thesis. Manuch's warmth and support from distance will always be remembered.

I take this opportunity to sincerely acknowledge Dr. Ghassan Hamarneh for his continual support and help during my Masters and PhD. Although Ghassan was at Simon Fraser University, he was always there to answer my emails with difficult questions in a short time notice. Also, Ghassan was there for me, to help finalize and improve my papers. Thank you, Ghassan. I learned a lot from you.

The clinical results described in this thesis would not have been obtained without a close collaboration with Department of Anaesthesiology and Intensive Care Medicine, University Medical Centre Schleswig-Holstein, Campus Kiel, Kiel, Germany, under supervision of Dr. Inez Frerichs, who provided me with EIT lung data. I hereby appreciate Dr. Inez Frerichs for her support and guidance.

I appreciate my best friends Alistair, Richard, Mamatjan, Ava, and Yanina for many rounds of helpful discussions on my research projects and their support. Thanks Alistair for being a great friend and educating me on geeky things, including Canadian beers. Thanks Richard for sharing your job experiences with me and being helpful and supportive. Mamatjan, thanks for exchanging ideas and life stories. Yanina, your diligence and insight in research always inspire me. Thanks for all the intelligent conversations, encouragements and of course for your unique taste in choosing great restaurants to try delicious foods,

dessert, and drinks. I wish you all the best in your new life at Harvard. A special thank you to Ava for all the support, trust, and encouragements. You have been always supportive, kind and just as excited as I am about my research and projects. Many thanks go to my friends in the lab Justin, Patrick, Libby, Adrian, Geoff, Queeny, and Daphne who help maintain a stimulating and fun filled environment. Thanks all of you for joining my summer events and being always smiley and cheerful. It is always fun to be with you.

The last but not the least, this thesis is lovingly dedicated to my mother, Parvin Nayebi. Her support, encouragement, and constant love have sustained me throughout my life. Thanks to my dad, older brother Farzad, twin brother Pouyan, and lovely sister Shima. Words are short to express my deep sense of gratitude towards my family. Although they have been thousands of miles away during my work on this thesis, their love and support have been always there.

Perhaps, I forgot someone: thank you to whom it concerns!

Contents

List of Abbreviations

Abbreviation	Details
CT	Computed Tomography
FEM	Finite Element Model
GN	Gauss-Newton
LMS	Least Mean Squares
MIT	Magnetic Induction Tomography
MRI	Magnetic Resonance Imaging
MSE	Mean Squared Error
NOSER	Newton's One-Step Error Reconstructor
PDIPM	Primal Dual Interior Point Methods
SNR	Signal to Noise Ratio
SVD	Singular Value Decomposition
TV	Total Variation
LSPDIPM	Level Set based Primal Dual Interior Point Method
SBRM	Shape based Reconstruction Method
VBRM	Voxel based Reconstruction Method
LS	Level Set
ALI	Acute Lung Injury
ARDS	Acute Respiratory Distress Syndrome
CT	Computed Tomography
EIDORS	Electrical Impedance and Diffuse Optics Reconstruction Software
EIT	Electrical Impedance Tomography
GREIT	Graz consensus Reconstruction algorithm for EIT
PEEP	Positive End-Expiration Pressure
VILI	Ventilator Induced Lung Injury

List of Primary Symbols

Symbols	Description
d	vector of desired signal
m	vector of unknown system parameters
h	system matrix or forward solution
δ	inter-frame delay
PD	primal-dual gap
I	identity matrix
J	Jacobian matrix
$\mathbf{J}$	current density
ϕ	the potential distribution
n_d	the order of the Gaussian distribution for the data term
n_m	the order of the Gaussian distribution for the parameter term
σ_{n_d}	the standard deviation for the data term
σ_{n_m}	the standard deviation for the parameter term
σ_{n_M}	the number of measurements
σ_{n_E}	the number of elements
m_0	a priori information of the model parameters
L	the Tikhonov regularization matrix
W	a diagonal weighting matrix
$f_d(m)$	a L1 norm based data mismatch term
$f_p(m)$	a L1 norm based regularization term
$g_d(m)$	a L2 norm based data mismatch term
$g_p(m)$	a L2 norm based regularization term
Ψ	level set function
Φ	a mapping function
$\Delta\Psi$	level set update function

Symbols	Description
P	primal problem
x	a dual variable
y	a dual variable
J_{LS}	the level set Jacobian matrix
J_{GN}	the GN Jacobian matrix
λ	regularization parameter, or hyperparameter
σ_0	a reference conductivity
m_{MAP}	maximum a posteriori (MAP) of the model parameters
n	noise sequence
n_E	number of electrodes
Ω	medium body under investigated
σ	conductivity, or standard deviation
σ_x	*a priori* amplitude of conductivity change
$\mathbf{\Sigma}_n$	covariance matrix of the measurement noise n
$\mathbf{\Sigma}_m$	covariance matrix of the desired image m
$\mathbf{\Sigma}_d$	covariance matrix of the data d
t	time index

List of Figures

List of Tables

Chapter 1

Introduction

This thesis is primarily concerned with the derivation, implementation and validation of edge-preserving image reconstruction methods (EPIRM) and proposes three novel variants of the EPIRM. The aim of the thesis is to propose mathematically sound numerical algorithms to solve the problem of reconstructing an 2D cross sectional image of the internal structures of an object so that the sharp edges of the internal structures are preserved. This chapter describes the problems to be addressed, the objective, and the contributions of this thesis. The review of the background materials is presented in chapters 2, 3, and 4, where detailed references to the literature are provided.

1.1 Classical tomographic image reconstruction

Tomography is a method of constructing a cross sectional image of the internal structures of a solid object through the measurement of a physical phenomena at the boundary of the object. Tomography has found widespread applications in many scientific fields including: physics, chemistry, astronomy, geophysics, and medicine. Tomographic image reconstruction often requires solving an inverse problem where the unknown image pixel

intensities are estimated from a small amount of measured data. An inverse problem is a process in which the unknown system parameters are inferred from a small amount of measured data where the measured data is affected by inevitable measurement noise which makes the estimation of the unknown parameters a hard task. The physical law governing a tomographic imaging modality can be either linear, such as CT, PET, and SPECT, or non-linear, such as near-infrared imaging, and electrical impedance tomography (EIT). The linear or non-linear relationship between the system parameters (image pixel intensities) and the measured data is defined using a forward model. In order to reconstruct an image, classical image reconstruction algorithms typically model a non-linear forward problem as: $d = h(m)$, where m is the image pixel intensities, d is the measured data, and h is the mapping function which relates the image pixel intensities m to the measured data d. In an inverse problem, the inverse solution m is not stable. Furthermore, the inverse solution m is sensitive to inevitable measurement noise from instrument readings. In order to stabilize the inverse solution, the a priori information about the desired solution in the form of one or several constraints is incorporated into the solution m to bias it. The algorithm which incorporates the a priori information into the solution is referred to as a regularization algorithm. To stabilize the inverse solution m, the classical regularization algorithm minimizes the following objective function:

$$\hat{m} = \underset{m}{\operatorname{argmin}} \left[D(h(m) - d_{real}) + P(m - m_{prior}) \right] \tag{1.1}$$

where $D(d - d_{real})$ is a data mismatch penalty function (or data mismatch term) that increases as the forward model $h(m)$ is less able to predict the real data d_{real}, $P(m)$ is a penalty (or regularization) function, which is also referred to as the image term, that increases as the inverse solution m is less likely, given the prior understanding of the model parameters m_{prior}. The regularization algorithm often contains a combination of residual

norms of the solution, e.g. quadratic norm (L2 norm), or sum of absolute values (L1 norm). For instance, the earliest approach to inverse problems was the Tikhonov regularization method, in which $D(h(m)-d_{real}) = \|h(m)-d_{real}\|^2$ and $P(m-m_{prior}) = \|m-m_{prior}\|^2$. In the Tikhonov reconstruction method, the inverse solution m can be obtained by minimizing the following quadratic norm based objective function:

$$\hat{m} = \underset{m}{\operatorname{argmin}} \left[\|h(m) - d_{real}\|^2 + \|m - m_{prior}\|^2 \right] \tag{1.2}$$

In the following subsection, the problems challenging the classical image reconstruction methods, such as the Tikhonov method, are briefly described.

1.1.1 Problems of the classical linear image reconstruction

The classical linear reconstruction algorithms, such as the Tiknonov method in (1.2), have shown good results in many cases; however, they have three main disadvantages: 1) The classical reconstruction methods smooth out the sharp edges present in the structure inside a medium (smoothness effect), 2) They are sensitive to measurement noise, and 3) They are sensitive to data outliers.

Figure 1.1 (a) shows the sensitivity of the Tikhonov method, as an instance of the classical image reconstruction method, to 14 dB measurement noise added to EIT simulated data. Comparing with the actual image in the first column of figure 1.1 (a), the sharp edges at the interface between the foreground and the background are smoothed out (problem#1). The quality of the reconstructed image using the Tikhonov method, in the second column of figure 1.1 (a), drops in the presence of measurement noise (problem#2). Figure 1.1 (b) shows the sensitivity of the Tikhonov method to data outliers. A data loss (data outliers) is generated by simulating an electrode, colored in red, with loose connection to the surface of the medium. The reconstructed image in the second column of figure

1.1 (b) is deformed due to sensitivity to the data outliers (problem#3). As an alternative reconstruction method, this thesis investigates EPIRMs which reformulate (1.2) to produce sharp images which are robust against the additional measurement noise and data outliers. EPIRMs are briefly introduced in the next section where their robustness against measurement noise and data outliers is demonstrated.

1.2 Edge-preserving image reconstruction methods

There are many situations in medical and industrial applications where the structures within a medium have high contrast against the background. For instance, in a CT scan, the contrast between different tissue types is seen as sharp interfaces because different tissue types have different X-ray attenuation coefficient. In such situations, it is desirable to be able to reconstruct the sharp transitions (sharp edges) at the interface between the structure and the background. However, the traditional reconstruction algorithms have difficulty in dealing with the sharp transitions and smooth the sharp edges. The EPIRMs, which are the focus of this thesis, are investigated as an alternative to the traditional reconstruction algorithms in order to deal with the discontinuities in the structure. In the literature, the EPIRMs have been studied through the concept of discontinuities reconstruction algorithms (Kaipio et al., 1999; Borsic et al., 2002) and shape reconstruction algorithms (Tamburrino and Rubinacci, 2002; Bruhl, 2001; Chan and Tai, 2004; Soleimani et al., 2006d; Dorn and Lesselier, 2009). Reconstruction using anisotropic-smoothness filters is an instance of the discontinuities reconstruction algorithms where the a priori information about the discontinuities in the structure is known and applied in the reconstruction algorithm (Kaipio et al., 1999). The discontinuities are reconstructed by relaxing the smoothness constraints in the direction normal to the discontinuities. The drawback of the reconstruction method using anisotropic-smoothness filters is that it demands a priori

information about the discontinuities. Another approach to reconstruct the discontinuities is to apply the total variation functionals in the reconstruction algorithm, which is referred to as the TV regularization method (Borchers, 2000). Unlike the traditional reconstruction algorithms which apply a discrete representation of differential operators in conjunction with the L2 norm in their regularization formulation, such as the one in (1.2), the TV functional is applied as a differential operator which leads to a L1 norm in a TV regularization method. The L1 norm based functional does not penalize the discontinuities, a trait absent in the L2 norm based functionals utilized in the traditional reconstruction algorithm. In chapter 2, the non-linear inverse problem in (1.2) is reformulated to contain the TV regularization term in order to preserve the edges in the reconstructed image.

The shape reconstruction algorithms are another sub domain of the EPIRMs which reconstruct the sharp edges in a profile. The shape reconstruction methods have been studied in the context of monotonicity based shape reconstruction (Tamburrino and Rubinacci, 2002), linear sampling algorithms (Bruhl, 2001), and level set (LS) (Chan and Tai, 2004; Soleimani et al., 2006d; Dorn and Lesselier, 2009). This thesis investigates the shape reconstruction methods in the context of the LS approach. The LS technique was originally proposed to model fast changing interfaces (Osher and Sethian, 1998; Osher and Paragios, 2003). In recent years, the application of the LS technique in scattering inverse problems was investigated (Chan and Tai, 2004; Soleimani et al., 2006d; Dorn and Lesselier, 2009). The level set based regularization methods (LSRM) have been studied to reconstruct the sharp transitions (sharp edges) in a profile (Soleimani et al., 2006d). The main difference between the LSRMs and the discontinuities reconstruction algorithms, such as the TV regularization algorithm, is that the LSRMs apply a LS based regularization term which constrains the shape of the structure instead of the amplitude of the pixel intensities. The LSRMs assume that the contrast at the interface between the structure and the back-

ground is high (sharp transition) and consider two different known intensity values for the image pixels which belong to the structure and the background. In an LSRM, the shape of the structure is unknown and is calculated as an inverse solution. To solve the non-linear inverse problem in (1.2) for the shape of the structure, the inverse problem is reformulated to contain a shape based regularization term which is defined based on a level set function (LSF). The LSF is a signed distance function representing the shape of the structure. The LSF is negative inside the structure, positive outside, and zero at the boundary. Therefore, the shape of the structure, or the boundary, is achieved at the zero level of the LSF. The minimization of the level set based regularization problem requires the evolution of the LSF such that in each iteration the structure moves from an initial guess toward an optimum shape, which is close to the actual profile. The LS evolution is stopped when the shape of the structure is sufficiently close to the actual profile. At the final iteration, the pixels at which the LSF is zero constitute the boundary of the structure (shape reconstruction). The level set approach can be applied in situations where approximate values of the parameters inside the structures with sharp interfaces are available; however, the sizes, shapes, locations and geometry of the structures are unknown (Soleimani et al., 2006d). The shape reconstruction methods have mostly been applied over simulated data in the past. This thesis proposes two novel shape reconstruction methods, referred to as the LSRM, and the LSPDIPM, and applies them on EIT simulated and experimental data. The mathematical procedures to derive the proposed LSRMs are presented in chapter 5 and 7.

1.2.1 Thesis motivation

The EPIRM is considered as an alternative reconstruction algorithm to resolve the three main problems of the traditional image reconstruction algorithms, discussed in subsection 1.1.1. This thesis explores the EPIRMs which reformulate (1.2) to contain the sum of

absolute values (L1 norm) on either the data mismatch term, the image term or both. In the remainder of this subsection, the aim is to illustrate the motivation of the thesis by comparing the ability of an EPIRM and the Tikhonov method, as a classical image reconstruction method, in preserving the sharp edges of a high contrast structure in a 2D circular medium when there is measurement errors. Figure 1.1 shows that the EPIRM does not smooth out the sharp edges present in the medium and indeed produces sharp reconstructed images with high robustness against measurement noise and data outliers. In figure 1.1, an EIT system, described in detail in chapter 3, was applied to reconstruct the conductivity of two low conductive, high contrast objects placed in the lower and upper regions of a 2D circular phantom. EIT data was simulated and perturbed by measurement errors. The first column in figures 1.1 (a) and (b) shows the actual image as well as a cross section profile along the bigger object, representing sharp transitions in the conductivity amplitudes at the interface between the foreground and the background. A successful reconstruction method retrieves these sharp transitions at the interface in the reconstructed image when there are measurement errors in the EIT data. Figure 1.1 (a) and (b) show the robustness comparison between the classical image reconstruction method in (1.2) and the EPIRM under the following two measurement conditions: 1) When there is 14 dB zero-mean Gaussian noise added to the EIT simulated data (figure 1.1 (a)), 2) When the connection of one electrode to the medium is loose and a data loss, or data outliers, occurs (figure 1.1 (b)). The data outliers are a non-Gaussian noise which was generated by simulating a loose connection for an electrode at the surface of the medium. The EIT reconstructed images using the Tikhonov method (the second column in the figures) and the EPIRM (the last column in the figures) as well as a cross-section profile of the bigger object (the second row in the figures) are demonstrated. In figure 1.1 (a), it is shown that the application of the L1 norm over the image term ($\|m - m_{prior}\|_1$) benefits the EPIRM

in terms of the robustness against the additional 14 dB zero-mean Gaussian noise to the data (measurement condition #1). The reconstructed image using the EPIRM with the L1 norm based image term preserves the sharp edges at the interface and offers similar cross section profile to the actual profile. However, the reconstructed image using the Tikhonov method containing the L2 norms over the image term ($\|m - m_{real}\|_2$) smooths out the sharp edges and does not offer a similar cross section profile to the actual profile. Figure 1.1 (b)

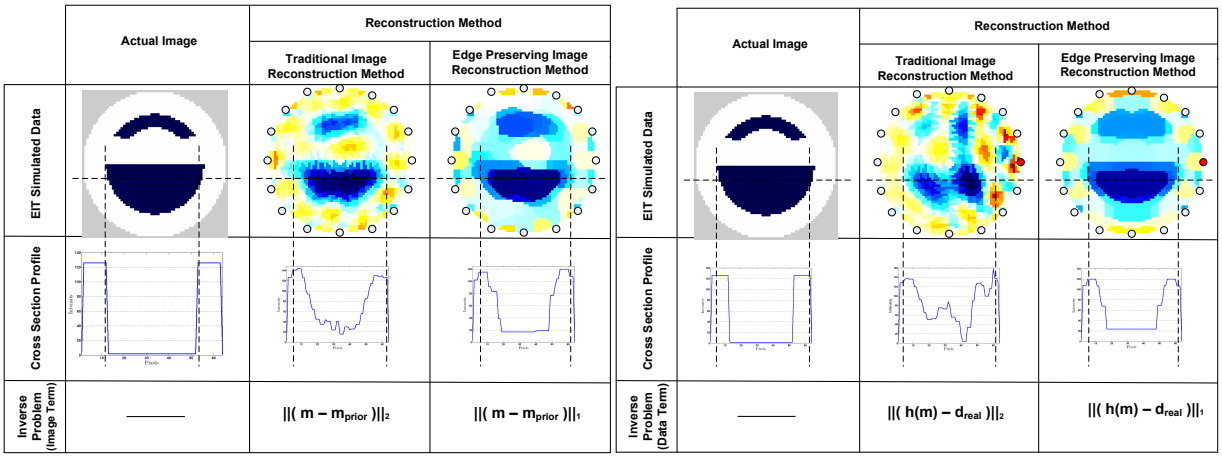

Figure 1.1: The robustness comparison between the traditional image reconstruction method and the edge preserving image reconstruction method. (a) In the presence of 14 dB zero-mean Gaussian noise. (b) In the presence of data outliers. The edge preserving image reconstruction method retrieves the sharp edges as shown in its cross-section profile; however, the cross-section profile of the traditional image reconstruction method is smoothed out and does not rebuild the sharp edges presented in the actual profile.

demonstrates the robustness of the EPIRM and the Tikhonov method against data outliers (measurement condition #2). An electrode, colored in red, is not completely attached to the surface of the medium and generates a data loss (data outliers). The results in figure 1.1 (b) offer that the application of the L1 norm over the data term ($\|d - d_{real}\|_1$) causes the EPIRM to become robust against the generated data outliers and able to reconstruct an image with an edge profile similar to the profile of the actual image. However, the

Tikhonov regularization method with the L2 norm on the data term ($\|d - d_{real}\|_2$) does not produce a sharp profile and its cross section profile is noisy and rippled. In figure 1.1 (a) and (b), one can define the resolution as the area underneath the cross section profile. It can be seen that the proposed EPIRMs have higher resolution (bigger area) than the traditional image reconstruction method with smaller area under its cross section profile.

1.2.2 Proposed edge-preserving image reconstruction methods

This thesis proposes three novel EPIRMs to produce sharp reconstructed images with high robustness against noise and data outliers. The EPIRMs can be derived from a proposed generalized regularization formulation. The proposed generalized regularization formulation differs the classical regularization methods, such as the Tikhonov method in (1.2), in the following aspects: 1) It independently applies the L1 and L2 norms over the data mismatch, the regularization terms, or both, 2) To offer sharp reconstructed images, it combines the smooth properties of the L2 norm based objective functionals with the blocky effect of the L1 norm based objective functionals. Chapter 5 proposes a novel LSRM, which belongs to the bigger domain described as shape reconstruction methods in subsection 1.2, in conjunction with the L2 norms (contribution#1). Chapter 6 discusses the proposed generalized inverse problem and derives its general inverse solution (contribution#2). Chapter 7 formulates a novel L1 norm based shape reconstruction method using the LS approach, which is referred to as LSPDIPM, and shows the derivation of the LSPDIPM using the proposed generalized inverse problem (contribution#3).

1.2.3 Applications of the proposed EPIRMs

The three proposed EPIRMs are useful in either medical or industrial applications where it is important to reconstruct the interfaces between several region of interests. In medical

application, the EPIRM is used for treatment planning, disease monitoring, or clinical studies. In many hospitals and health providers, the standard of practice is a double reading procedure, where a computer aided diagnostic (CAD) system helps physicians or radiologists interpret a diagnostic image. The EPIRM can be applied in a CAD system to reconstruct a sharp diagnostic image to assist the physicians or radiologists to plan the treatment or to monitor the condition of a patient in intensive care unit (ICU).

The proposed EPIRMs can be applied on many imaging modalities, such as PET, and CT scan, to preserve the sharp edges at the interface between different tissues. EIT is an imaging modality that introduces energy to the medium and measure its interaction with the medium in order to investigate the structure or function of the medium (Adler and Guardo, 1996). EIT reconstructs the conductivity distribution inside the medium using surface measurements. This thesis applies EIT as an instance of an inverse problem to show the implementation of the proposed EPIRMs. The proposed EPIRMs are applied to EIT to monitor the air distribution inside the lungs during the incremental positive end-expiratory pressure (PEEP) trial for mechanically ventilated patients. The objective is to reconstruct the area of the ventilated regions inside the lungs during the incremental PEEP trial. The applied clinical data contains EIT data of 8 lung healthy patients and 18 acute lung injury (ALI) patients. The CT equivalents of the applied clinical data were not available to be applied as ground truth; and therefore, qualitative comparisons between the clinical results of the proposed EPIRMs and those of the competing methods are provided. The quantitative and qualitative comparisons are accomplished over EIT simulated data in chapter 8.

1.3 Objectives of this thesis

This thesis investigates novel approaches to the EPIRMs in order to improve the quality and the contrast of the reconstructed image, as well as to enhance its robustness against measurement noise and data outliers, which are two common issues in clinical applications of the tomography. The assessment of the proposed EPIRMs is accomplished over EIT simulated data and EIT real data of human breathing, where the latter has been of high importance in the EIT community in recent years. The realization of aforementioned objectives was achieved in terms of: 1) Developing the LSRM in difference mode, 2) Investigating the applicability of an independent combination of the L1 and L2 norms for defining an inverse problem, 3) Developing a novel variant of the LSRM to allow for all possible combinations of the L1 norms and L2 norms over the inverse problem terms, 4) Proposing a sophisticated evaluation framework to compare the performance of the competing image reconstruction algorithms with that of the proposed image reconstruction algorithms in this thesis.

1.4 Contributions of this thesis

1.4.1 Contributions by Objectives

- *Level Set based Reconstruction Method for EIT Lung Images: First Clinical Results*
  The previously established LSRMs were applied only to simulated data and proposed in absolute mode where the absolute conductivity value for each element in the medium was calculated. Whereas the systematic errors of EIT stay constant from one frame to another, the reconstruction of conductivity changes between two subsequent frames reduces image artifacts in difference EIT. The difference EIT provides the conductivity changes, rather than the absolute conductivity value, and is more

suitable for EIT clinical applications. Therefore to bring high contrast EIT into routine clinical applications, it is necessary to develop a LSRM using a difference solver. This thesis formulates a novel LSRM using a difference solver and demonstrates the first clinical results of applying difference LSRM for EIT lung image in chapter 5. The performance of the proposed LSRM is assessed over simulated and clinical data.

This study is presented in chapter 5 and has been published as "Level Set based Reconstruction Algorithm for EIT Lung Images: First Clinical Results", Peyman Rahmati, Manuchehr Soleimani, Sven Pulletz, Inez Frerichs, and Andy Adler, *Journal of Physiological Measurement*, **33**(5):739-50, 2012.

- *A Generalized Inverse Problem with Weighted L1 and L2 Norms*

  The traditional inverse problems are usually defined by penalty terms which are based on square fittings (L2 norms). However in practice, the L2 norms ($\|...\|$) smooth out the sharp edges present in the internal structures of a medium. An effective alternative to the L2 norms, which does not smooth out the sharp edges, is the L1 norms ($|...|$). This thesis formulates a novel generalized inverse problem which mixes the L1 norms and the L2 norms on both the data and the regularization terms of an inverse problem. An iterative minimization framework, such as primal-dual interior point method (PDIPM), is utilized to estimate the inverse solution of the proposed generalized inverse problem. The aim of this study is to investigate the effect of different combination of the L1 and L2 norms on the inverse solution so that different inverse problem applications raised in engineering, system biology, seismology, soil study, and life science can take advantage of the achieved results.

  This work is presented in Chapter 6. This work has been presented in *The 36th Annual Conference of the Canadian Medical and Biological Engineering Society.* This

study was published as "Weighted L1 and L2 Norms for Image Reconstruction: First Clinical Results of Electrical Impedance Tomography Lung Data", Peyman Rahmati, Andy Adler, *The 36th Annual Conference of the Canadian Medical and Biological Engineering Society*, May 2013. An extended version of these papers is presented in chapterchap:GPDIPM.

- *Level Set Technique for High Contrast Image Reconstruction.*

  The LSRM offers high contrast image reconstruction which is desirable in many applications including medical and industrial imaging applications. This thesis formulates a novel optimization framework, referred to as level set based primal-dual interior point method (LSPDIPM), to estimate the inverse solution of a general inverse problem which independently contains a combination of both the L1 norms and the L2 norms. The reconstructed images of the proposed LSPDIPM offer high contrast and quality when compared with those of four competing methods, GN with Tikhonov regularization term, GN with Newton's one-step error reconstructor (NOSER) algorithm, TV, and the L1 norm based inverse problem solved using the PDIPM framework, referred to as the PDIPM in this thesis, over the same EIT simulated and real data. Also, the proposed LSPDIPM is successful in dealing with measurement noise (14 dB zero-mean Gaussian noise) and strong outliers.

  This work is presented in chapter 7 and has been presented in two conferences: *The 36 Annual Conference of the Canadian Medical and Biological Engineering Society (CMBES), Ottawa, Canada* and *XV Int. Conf. Electrical Bio-Impedance & XIV Electrical Impedance Tomography, Germany.* The results of this work were published as"Level Set Technique for High Contrast Image Reconstruction", Peyman Rahmati, and Andy Adler, *The 36 Annual Conference of the Canadian Medical and Biological Engineering Society*, 2013 and " A Level Set based Regularization Framework for EIT

Image Reconstruction", Peyman Rahmati, and Andy Adler, *XV Int. Conf. Electrical Bio-Impedance & XIV Electrical Impedance Tomography*, Heilbad Heiligenstadt, Germany, 2013.

- *Evaluation Framework*

  This thesis also proposes an evaluation framework to compare the performance of four competing reconstruction algorithms with the proposed EPIRMs. The EIT data for two low conductive inclusions with different shapes located in the upper and lower regions of a 2D circular phantom is simulated in MATLAB using EIDORS toolbox developed by Adler and Lionheart (2005). A feature vector, including five morphological metrics and two shape descriptors, is considered to assess the image reconstruction accuracy for each competing method. The euclidean distance between the feature vector of a reconstruction method and that of the ground truth is calculated. The reconstruction method with the smallest euclidean distance is selected as the best performing method with the highest reconstruction accuracy.

  Moreover, the robustness of the competing image reconstruction methods against potential uncertainties, such as measurement noise and data outliers, is evaluated. A robustness metrics (noise measurement) is defined to quantitatively assess a method's robustness against measurement errors. Chapter 8 discusses the proposed evaluation framework and shows the achieved qualitative and quantitative comparison results.

Chapter 2

Inverse Problems

2.1 Summary

This chapter introduces inverse problems through the concept of forward problem and its inverse solution. The existence, uniqueness, and the stability of the inverse solution is discussed. The inverse solution of an inverse problem with quadratic functionals (L2 norms) for linear and non-linear cases is presented. Iterative GN method is derived for a non-linear inverse problem. The focus of this thesis is on the EPIRMs which are non-linear inverse problem containing absolute value based functionals (L1 norms). As an instance of the EPIRMs, the total variation (TV) regularization method which applies the sum of absolute values (L1 norm) on its regularization term is discussed.

2.2 Introduction

In many applications, it is desirable to relate the physical parameters m of a system to the measured observation or data d. The unknown system parameters define the properties of the system and are not directly measurable. The experimental observations are easily

measurable and their values depend on the value of the unknown parameters through a linear or non-linear relationship, depending on the physical laws governing the system. If the fundamental physics governing the system are sufficiently understood, a function h can be specified to relate m and d as follows:

$$d = h(m), \tag{2.1}$$

where h is a linear or non-linear function that links the system parameters vector m to the measured data or observations vector d. The equation in (2.1) is referred to as a forward problem. In a forward problem, the data vector d is computed, given the system parameters vector m. The inverse problem occurs when unknown or hard to determine parameters vector of the system (m) are determined from the experimental observations or data vector d. For example, consider a tomography problem where the velocity of the ray ($s(x)$) at point x is determined from the travel time of the ray (t) in the medium. If the velocity $s(x)$ and the ray path l are known, the forward problem to compute the travel time of the ray t can be written as follows:

$$t = \int_l s(x(l))dl \tag{2.2}$$

In the case that the ray path l does not depend on the velocity $s(x)$ and can be approximated as a straight line, the forward problem in (2.2) is linear.

The inverse problem is hard, when compared to simple problems with hard to measure parameters, because it is possible to find many parameters vectors that mathematically fit the observations or data points vector but indeed are not physically plausible. The difficulty of the inverse problem, when compared with the simple problems, is that one needs to find the optimal inverse solution m that 1) fits to the data vector, 2) is plausible in terms of

the physics governing the system, 3) is stable and consistent in the presence of noise. A practical issue is that data vector d may contain some amount of noise, due to unexpected influences on instrument readings or numerical round-off. Therefore, it makes sense to formulate the data as two components: 1) The noiseless data vector $d_{true} = h(m_{true})$ which is achieved from an ideal instrument, 2) A noise component vector n. The forward model can be rewritten as follows:

$$d = h(m_{true}) + n, \tag{2.3}$$

It is mathematically feasible that there are an infinite number of parameters vectors m that fit the actual data d_{true}. Also, it is possible to find a solution m which is affected by a very small amplitude noise n and has a little or no correspondence to m_{true}. If any of the following cases happen, the inverse solution m is ill-posed based on the Hadamard rules: 1) The solution does not exist, which means there is no parameters vector m that satisfies the data vector d in (2.1), 2) The solution is not unique, which means the exact solution exist but it is not unique and there are other solutions, aside from m_{true}, that satisfy the forward problem in (2.1), or 3) The solution is not stable and is sensitive to noise, which is the case in many inverse problems where a small amplitude noise n in (2.3) is magnified in the inverse solution. It is possible to stabilize the inversion by biasing the solution through applying additional constraints, which is referred to as a regularization. To stabilize the inverse solution, there are several regularization methods which are formed in terms of a penalty norm. As it is shown in chapter 1, a generalized regularization method can be written as:

$$\hat{m} = \underset{m}{\operatorname{argmin}} \left[D(h(m) - d_{real}) + P(m - m_{prior}) \right] \tag{2.4}$$

where the data mismatch term $D(h(m) - d_{real})$ and the image term $P(m - m_{prior})$ are linear or non-linear penalty functions which can be defined based on either quadratic based functionals, sum of absolute values based functionals, or both. According to the

applied penalty functions in the definition of a regularization method, this thesis assigns the regularization methods to one of the following two groups : 1) Regularization for inverse problem with quadratic functionals, 2) Regularization for inverse problem with absolute values based functionals. Section 2.3 discusses the regularization for inverse problem with quadratic functionals for the linear and non-linear inverse problems. Section IP-absolute discusses the regularization for non-linear inverse problem with the sum of absolute values based functionals through the concept of TV and presents the TV regularization method as an iterative regularization method. The application of the primal-dual interior point method (PDIPM) in order to minimize the sum of absolute values based functionals in the TV regularization method is shown.

2.3 Regularization for inverse problem with quadratic functionals

2.3.1 Linear inverse problem

In a linear case, the forward model in (2.1) is written as follows:

$$d = Hm \tag{2.5}$$

where $H = \frac{\partial d}{\partial m}$ is a matrix of all first-order partial derivatives of measured data d with respect to model parameters m, which is also referred to as Jacobian matrix or the sensitivity matrix. In practice, the inverse solution m is not stable and is sensitive to inevitable measurement noise from instrument readings. Also, the inversion is ill-posed according to Hadamard rule, which is described in the beginning of this chapter. The ill-posedness of the inversion can be discussed through the concept of singular value decomposition (SVD).

2.3.2 Singular value decomposition

In the singular value decomposition (SVD), an n_M by n_E matrix, such as the sensitivity matrix H, is factored as follows:

$$H = USV^T, \tag{2.6}$$

where U is an n_M by n_M orthogonal matrix, referred to as left singular vector, V is a an n_E by n_E orthogonal matrix, referred to as right singular vector, and S is an n_M by n_E diagonal matrix with diagonal elements referred to as singular values of matrix H. The singular values of matrix S are arranged in a decreasing order such that:

$$\lambda_1 \geq \ldots \geq \lambda_n \geq 0, \tag{2.7}$$

The condition number (CN) is defined as the ratio of the largest to smallest singular values of matrix H as follows:

$$CN = \frac{\lambda_1}{\lambda_n}, \tag{2.8}$$

The ill-posedness of a problem can be demonstrated by the singular values abruptly decaying to zero, which generates a very large CN. A large CN indicates that an inversion will magnify any errors in the data. In an ill-posed inverse problem, there are significant number of small singular values, close to zero, in matrix S. When matrix H is inverted to compute the unknown system parameters m in (2.5), these small singular values become very large, resulting in large fluctuations in the solution (unstable inverse solution). Matrix H is usually rank deficient, meaning that there is a substantial gap between the largest of these small singular values and the first nonzero singular value, and has very large CN. To diminish or truncate the effect of the small singular values in the inverse solution, a regularization method is required. Truncated SVD (TSVD) is a simple regularization method which truncates a certain number of the smallest singular values to remove their effect

on the inverse solution. However, TSVD does not allow to model constraints applied in the solution, and therefore may not guarantee a stable solution in many situations. Least square (LS) inversion can be applied to estimate the inverse solution. In the following, the LS inversion for a linear inverse problem is described.

2.3.3 Linear least square inversion

A classical solution to estimate the unknown parameters m can be achieved using LS inversion as follows:

$$m = \text{argmin} \, \|Hm - d\|^2, \tag{2.9}$$

However, the inverse solution of the equation in (2.9) is ill-posed according to the Hadamard rule. In order to stabilize the inverse solution, Tikhonov regularization algorithm can be applied to bias the solution through the incorporation of the a priori information about the desired solution. The a priori information is added in the form of one or several LS based objective functionals (constraints) into the solution m to resolve the ill-posedness of the inverse solution. The Tikhonov regularized linear inverse problem is written as: (Tikhonov, 1963)

$$m = \text{argmin} \, \|H \; m - d\|^2 + \alpha \|R(m - m_0)\|^2, \tag{2.10}$$

where H is the sensitivity matrix, R is the regularization matrix, $\alpha > 0$ is the regularization factor, m_0 is a priori estimate of the solution m. Matrix R is prior information about the inverse solution and compensates for the missing information because of the rank deficiency of matrix H. The first term in (2.10) is called the data mismatch term and the second term is referred to as the regularization term or the image term. The regularization factor α increases or decreases the effect of matrix R. The inverse solution of (2.10) can be

calculated by minimizing the following error function:

$$e = \|(d - Hm)\|^2 + \alpha\|R(m - m_0)\|^2, \tag{2.11}$$

To minimize the error function, the first derivative of the error function with respect to m is taken as follows:

$$\begin{aligned} \frac{de}{dm} &= \tfrac{d}{dm}[(d - Hm)^t(d - Hm) + (m - m_0)^t R(m - m_0)] &= 0, \\ &= \tfrac{d}{dm}[d^t d - 2H^t H + (m - m_0)^t R(m - m_0)] &= 0, \end{aligned} \tag{2.12}$$

we have:

$$\begin{aligned} \frac{de}{dm} = -2H^t d + 2H^t H + 2R(m - m_0) &= 0, \\ H^t H + R(m - m_0) &= H^t d, \end{aligned} \tag{2.13}$$

It can be written:

$$\begin{aligned} (H^t H + R)m &= H^t d + Rm_0, \\ m &= (H^t H + R)^{-1}(H^t d + Rm_0), \end{aligned} \tag{2.14}$$

where the last equation is the inverse solution to (2.10).

2.3.4 Non-linear inverse problem

A non-linear inverse problem with Tikhonov regularization term can be written as follows:

$$e = \|d - h(m)\|^2 + \|R(m - m_0)\|^2, \tag{2.15}$$

where h is a non-linear function of the model parameter m. To minimize the least square error function in (2.15), the first derivative of the error function with respect to m is taken as follows:

$$\begin{aligned} \frac{de}{dm} &= \tfrac{d}{dm}[(d-h(m))^t(d-h(m)) + (m-m_0)^t R(m-m_0)] &= 0, \\ &= \tfrac{d}{dm}[d^t d - 2h(m)^t h(m) + (m-m_0)^t R(m-m_0)] &= 0, \end{aligned} \tag{2.16}$$

where the Jacobian matrix (J) is defined as: $J = \frac{\partial d}{\partial m}$, thus we have:

$$\begin{aligned} \frac{de}{dm} = -2J^t(m)d + 2J^t(m)h(m) + 2R(m-m_0) &= 0, \\ J^t(m)h(m) + R(m-m_0) &= J^t(m)d, \end{aligned} \tag{2.17}$$

An iterative regularization method, such as iterative GN, is applied to derive the inverse solution of the non-linear inverse problem in (2.15) using the successive linearisation. The following shows the minimization of the non-linear inverse problem using an iterative GN. For the non-linear case, if $h(m)$ starts at estimate m_k, then:

$$h(m) = J(m_k)(m - m_k) + h(m_k), \tag{2.18}$$

Applying the notation changes of $h(m_k) = h_k$, and $J(m_k) = J_k$:

$$\begin{aligned}
J^t(m)h(m) + R(m - m_0) &= J^t(m)d, \\
J_k^t(J_k(m - m_k) + h_k) + R(m - m_0) &= J_k^t d, \\
J_k^t J_k(m - m_k) + J^t h_k + R(m - m_0) &= J_k^t d, \\
J_k^t J_k(m - m_k) + R(m - m_0) &= J_k^t(d - h_k), \\
J_k^t J_k(m - m_k) + R(m - m_0 + m_k - m_k) &= J_k^t(d - h_k), \\
J_k^t J_k(m - m_k) + R(m - m_k) + R(m_k - m_0) &= J_k^t(y - h_k), \\
J_k^t J_k(m - m_k) + R(m - m_k) - R(m_0 - m_k) &= J_k^t(y - h_k), \\
J_k^t J_k(m - m_k) + R(m - m_k) &= J_k^t(y - h_k) + R(m_0 - m_k), \\
(J_k^t J_k + R)(m - m_k) &= J_k^t(d - h_k) + R(m_0 - m_k), \\
m - m_k &= (J_k^t J_k + R)^{-1}(J_k^t(d - h_k) + R(m_0 - m_k))
\end{aligned} \tag{2.19}$$

The solution (m) to (2.19) is described as m_{k+1}. Therefore, $\Delta_{k+1} = m_{k+1} - m_k$.

2.4 Inverse problem with absolute values based functionals

In recent years, the application of the absolute values (L1 norm) in the definition of inverse problem have received noticeable attention. The L1 norm functionals are well understood in the framework of *Total Variation* concept. Total Variation (TV) functionals are first proposed by Rudin et al. (1992) for noise restoration or denoising applications. By defini-

tion, TV measures the oscillations of a function (f) over its domain(Ω) and is formulated as (Borchers, 2000):

$$TV(f) = \int_{\Omega} |\nabla\ f|, \tag{2.20}$$

The popularity of TV in the context of inverse problem, when applied as a regularization term to reduce the oscillations in a continuous or discrete function, comes from its desirable property to selecting a distribution of the unknown parameters that has the least total variation from all possible parameter distributions that are consistent with the measured data. When applied as a regularization term in an inverse problem, TV can reconstruct sharp profiles (non-smooth transitions) in the model space. A blocky effect in the reconstructed image using the TV is produced. The blockiness occurs because the system unknown parameters are piecewise constant coefficients and are reconstructed as sharp edges. In contrast, L2 norm functionals, discussed in subsection 2.3.1, only minimize continuous functions with the smoothest oscillations. Hence, the L2 norms smooth sharp edges and create smooth profiles in image reconstruction applications even if the actual profile changes are sharp. The non-linear Tikhonov functional with TV as the regularization term can be written as (Borsic et al., 2001):

$$m = \text{argmin}\, \|h(m) - d\| + \alpha \int_{\Omega} |\nabla\ m|, \tag{2.21}$$

The use of TV as the penalty term in (2.21) poses computational difficulties at the points of non-differentiability where $|\nabla\ m| = 0$. There are several numerical methods to minimize the sum of absolute values or L1 norms in the literature. The Markov Chain-MonteCarlo Method (MCMC) uses central estimators, such as MAP estimates, to minimize the L1 norm in TV regularized inverse problems (Somersalo et al., 1997; Kaipio et al., 2000; Borsic and Adler, 2012). The advantage of the MCMC is that it does not need to take

the differentiation of the objective functional to minimize the functional and instead the minimization is accomplished through sampling the posterior probability density. However, the sampling involves high computational effort (Borsic and Adler, 2012). A non-smooth L1 norm based inverse problems can be formulated in a deterministic form according to the traditional Tikhonov regularization formulation as follows (Borsic and Adler, 2012):

$$m = \text{argmin} \left\{ \|W(h(m) - d)\|^2 + \alpha \sum_{i=1}^{M} |L_i(m - m_0)| \right\}, \tag{2.22}$$

where W is a weighting matrix to weight the reliable observations in the measured data. It is shown the non-smooth L1 optimization problem in (2.22) can be smoothed as (Acar and Vogel, 1994; Dobson and Vogel, 1997):

$$m = \text{argmin} \left\{ \|W(h(m) - d)\|^2 + \alpha \sum_{i=1}^{M} \sqrt{(L_i(m - m_0))^2 + \beta} \right\}, \tag{2.23}$$

where $\beta > 0$. The smoothed inverse problem in (2.23) is differentiable everywhere for $\beta > 0$. With the applied smoothing condition in (2.23), it is possible to use the traditional minimization algorithms, such as the steepest Descent or the Newton method, to numerically solve the smoothed inverse problem (Borsic and Adler, 2012). However, the traditional minimization methods are either slow in convergence or sensitive to the selection of the auxiliary variable β (Borsic and Adler, 2012). One of the most efficient optimization method for L1 penalty problems is the Primal-Dual Interior Point (PDIPM) method (Andersen et al., 2000). The following describes the application of the PDIPM framework to the non-linear TV regularization method in (2.22). The assumption is that there is no prior information about the structure and $m_0 = 0$. A primal problem is written as follows:

$$min_m \left\{ \|(h(m) - d)\|^2 + \alpha \sum_{i=1}^{M} |L_i m| \right\}, \tag{2.24}$$

where,

$$|L_i m| = max_{x:|x|\leq 1} x L_i m, \tag{2.25}$$

where x is referred to as dual variable. By applying the (2.25) in (2.24), a dual problem, which is equivalent to the primal problem, can be written as follows:

$$max_{x:|x|\leq 1} min_m \left\{ \|(h(m) - d)\|^2 + \alpha x^T L m \right\}, \tag{2.26}$$

An optimal point for the optimization problem $min_m \left\{ \|(h(m) - d)\|^2 + \alpha x^T L m \right\}$ can be achieved by the first order conditions as below:

$$J^T (h(m) - d) + \alpha L^T m = 0, \tag{2.27}$$

where J is the Jacobian matrix. The dual problem can be rewritten as follows:

$$\begin{aligned} max_{x:|x|\leq 1} & \left\{ \|(h(m) - d)\|^2 + \alpha x^T L m \right\}, \\ & x : |x| \leq 1, \\ & J^T (h(m) - d) + \alpha L^T m = 0, \end{aligned} \tag{2.28}$$

An optimal point is the one which satisfies the optimality of the primal and dual problems simultaneously. A primal-dual gap is defined so that it is zero at the optimal point and positive elsewhere:

$$\|(h(m)-d)\|^2 + \alpha \sum_{i=1}^{M} |L_i m| - \|(h(m)-d)\|^2 - \alpha x^T L m = \alpha \left\{ \sum_{i=1}^{M} |L_i m| - x^T L m \right\}, \tag{2.29}$$

The condition that nulls the primal-dual gap is referred to as complementary condition and is written as:

$$\sum_{i=1}^{M} |L_i m| - x^T L m = 0, \tag{2.30}$$

By applying the dual feasibility $|x| \leq 1$, the following is obtained:

$$L_i m - x_i |L_i m| = 0; i = 1, \ldots, M \tag{2.31}$$

Therefore, the PDIPM framework for the non-linear TV regularization problem in (2.24) can be written as follows:

$$\begin{aligned} x : |x| &\leq 1, \\ J^T(h(m) - d) + \alpha L^T m &= 0, \\ L_i m - x_i |L_i m| &= 0; i = 1, \ldots, M \end{aligned} \tag{2.32}$$

The above system of equations has to be solved iteratively using an iterative method, such an iterative GN method. However, the system is not differentiable at points where $L_i m = 0$. The centering condition is applied to resolve the non-differentiability issue through replacing $|L_i m|$ by $(\|L_i m\|^2 + \beta)^{1/2}$. Borsic and Adler (2012) show the efficiency of the PDIPM framework in minimizing a TV regularized inverse problem; four different types of inverse problems were solved using the PDIPM framework: 1) L2L2 problem, which is the traditional Tikhonov regularization problem solved using the Newton method, 2) L1L2 problem, which uses the L1 norm on the data mismatch term of an inverse problem and the L2 norm on the regularization term, 3) L2L1 problem, which uses the L2 norm on the data mismatch term and the L1 norm on the regularization term, and 4) L1L1 problem, which uses the L1 norm on the data mismatch and the L2 norm on the regularization

term. Borsic and Adler (2012) show the implementation of the aforementioned four inverse problems over the EIT system. They report that the L1 norm on the data mismatch brings the highest robustness to the data outliers (loss of data), and the L1 norm on the regularization term makes the system robust against the spatial noise. Chapter 6 in this thesis aims to discuss a broader perspective of the possible deterministic inverse problems by proposing a generalized non-linear inverse problem solved using the PDIPM framework. The PDIPM framework as an iterative minimization method to solve a non-linear ill-posed inverse problem is applied in chapter 6.

Chapter 3

Electrical Impedance Tomography

3.1 Summary

This chapter discusses the background of Electrical Impedance Tomography (EIT) in terms of history, theory, and applications. In section 3.3, EIT image reconstruction method using Tikhonov regularization is described. Finally in section 3.4, EIT current streamlines, equipotentials, and sensitivity to conductivity changes are discussed.

3.2 Electrical Impedance Tomography

Inverse problems intend to identify the unknown or hard to determine parameters in a system from a set of measurement or observations. There are many instances of an inverse problem in geophysics, systems biology, life science, bioinformatics, engineering, and many other sciences. This thesis applies EIT as a standard instance of inverse problem. EIT is an imaging modality founded in 1978 which uses simple physics rules to non-invasively reconstruct useful images of inner structures of an object. EIT is a non-invasive, non-ionizing and relatively inexpensive imaging modality. EIT is capable of producing a 2D or

3D image of the conductivity distribution of a medium. EIT systems come with various numbers of surface electrode arrays, such as 8, 16, 32, 64, depending on the application. In a typical EIT system, one pair of electrodes injects low frequency current to the medium and the other pairs of the electrodes collect the difference voltage on the surface of the medium. Figure 3.1 shows the block diagram of a typical EIT system. There are five main blocks: the phantom thorax, the current source, the amplifiers, the data acquisition, and the monitor. The phantom thorax includes the left and the right lungs with the resistivity of 1000 ohm-cm, the heart with resistivity of 150 ohm-cm, and the background saline with resistivity of 330 ohm-cm. The current source injects a current of about 300 micro amps with low frequency of 10 kHz into the tank. The current is applied across two electrodes and distributed through the tank. The resulting voltages at the surface of the tank are magnified by the difference amplifiers. The measured difference voltages are fed to the data acquisition system. A frame of the measured data is then transferred to the imaging system and the data is monitored on the screen.

3.2.1 EIT applications

EIT has been first applied in many geophysics applications to image the inner structures of geological objects. The electrical conductivity of geological objects such as rocks, soils, the flow of contaminants, can differ by several orders of magnitude depending on the nature of the object. EIT uses inverse problem techniques to measure the electrical conductivity distribution of an object based on a set of surface measurements. In geophysics, the surface measurements are collected using several electrode arrays mounted in the ground around the excavation zone. In biomedical imaging applications, the surface measurements are collected using typically 16 electrodes around a patient's thorax to image the air distributions inside the lungs. In studies of volcanoes, high conductivity zones under volcano

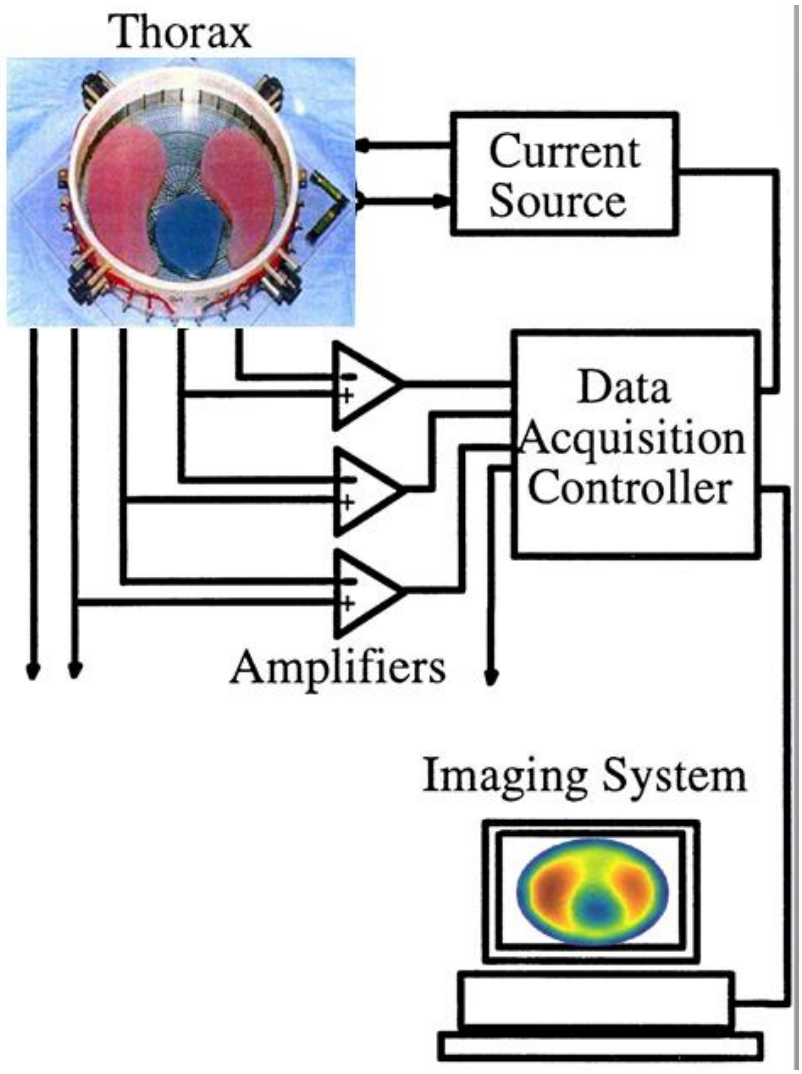

Figure 3.1: EIT block diagram.

shows a geophysical area altered by a hydrothermal system. In soil studies, the porosity and the degree of saturation of soil are calculated using the measured EIT electrical conductivity values (Reynolds, 1997). In fluid studies, the flow of contaminants, location of contamination sources can be monitored using EIT electrical conductivity values (Ogilvy et al., 2002; Binley and Daily, 2004). And in biomedical imaging applications, the low conductivity values indicate the location of the inhaled air inside the lungs. The application of EIT in monitoring the human body first occurred in the mid 1980s. Soon after the first

applications in the medical imaging, EIT showed promising results with acceptable image quality.

3.2.2 EIT difficulties

As discussed in chapter 2, Hadamard, in 1902, defined a problem as ill-posed if it does not meet any of the following three criteria: has one solution, unique solution, and solution depends on measurements or data. The latter often happens in EIT and causes EIT to be an ill-posed problem. In EIT, small changes in the solution (conductivity values) will cause noticeable changes in the resulting potentials at the boundary. There are still other issues challenging the imaging using an EIT systems, such as electrode movement, high sensitivity of the solution to spatial noise and outliers, convergence to the optimal solution does not follow a pre-defined pattern and highly depends on the measurement conditions (signal to noise ratio, and data quality). To stabilize the solution, a regularization technique is applied which converts an ill posed inverse problem to a well-defined one. Chapter **??** discusses about linear or non-linear regularization methods to stabilize the inverse solution of a linear or non-linear ill-posed inverse problem, respectively. In the following, Tikhonov regularization method, which is one of the most common regularization techniques, is described for EIT image reconstruction.

3.2.3 EIT current stimulation patterns

In EIT, the pattern of collecting difference voltages depends on the application. There are several predefined patterns shown to be effective in reconstructing high quality images. Adjacent current pattern, opposite stimulation, zigzag stimulation, and trigonometric current pattern are some of the most common stimulation approaches. The adjacent is applied widely in many different applications. In an adjacent stimulation pattern, two stimulating

electrodes located next to each other inject current to the medium and the other pairs of adjacent electrodes measure the surface difference voltage. To achieve one complete frame of image data, EIT injects currents as many times as there are electrodes attached around the medium. The adjacent current pattern offers low spatial resolution as its sensitivity to the potential changes in the middle of the medium is lower than its sensitivity to the potential changes at the boundary of the medium where there are surface electrodes. The opposite current pattern is when two electrodes, located at 180 degree from each other, inject current to the medium and the resultant different voltages are measured by the remaining electrodes. The trigonometric stimulation pattern is the most complex current pattern where there are 32 to 64 electrodes simultaneously injecting current to the medium. The high number of electrodes in this pattern provide higher spatial resolution and the simultaneous current injection causes highly uniform sensitivity matrix, meaning that the spatial resolution does not depend on the location and is highly uniform across the image plane.

In EIT, the number of differential measurements depends on the current stimulation pattern and the number of the electrodes. For example, $n_E - 3$ measurements are taken in an adjacent current stimulation where n_E is the number of electrodes. The measurements of the stimulation electrodes themselves are removed from the differential measurements. The total number of differential measurements (n_M) to construct one data frame is $n_M = n_E(n_E - 3)$.

3.3 EIT image reconstruction

EIT image reconstruction is the process to produce a conductivity distribution image of a medium using the injection of current into the medium and the collection of the resulting difference voltages at the boundary of the medium. EIT image reconstruction is challenging

because the reconstruction of conductivity changes within a medium requires solving a severely ill-posed, nonlinear inverse problem. To resolve the ill-posedness of the EIT image reconstruction, a regularization technique is utilized, where the complexity of the applied regularization framework depends on the requirements of the applications. The following key challenges in EIT image reconstruction have been identified:

1. **Problems related to the physics of the EIT system**

   EIT stimulates the medium through an alternating current injected from a pair of electrodes. The challenge is that the current stays close to the electrodes and this causes low sensitivity of the measurements to changes inside the medium, which makes the EIT image reconstruction an ill-posed problem.

2. **Problems related to the image reconstruction algorithms**

   There are several other problems challenging the scientists in a variety of fields regarding the high contrast tomographic image reconstruction. The a priori information about the inclusions can be applied to reformulate the inverse problem to contain additional constraints based on the a priori information, referred to as regularization terms. Many applications deal with the reconstruction and optimization of geometries, such as shapes, and topologies; however, there is no natural a-priori information on shapes or topological structures of the solution, such as number of connected components, star-shapedness, and convexity.

   Another problem is that most of the classical reconstruction algorithms, such as the well-known Gauss-Newton (GN) method, are based on the quadratic formulations, such as mean square errors (MSE), or equivalently the L2 norms. The L2 norms impose smoothness constraints on solutions thereby prohibiting the reconstruction of sharp edges in the recovered conductivity distribution. Besides, it has been shown that the L2 norms are sensitive to measurement noise and data outliers.

3.3.1 Solutions in the literature

- **Solution for the problems related to the physics of the EIT system**

  To resolve the ill-posedness of EIT, a regularization technique is applied to stabilize the inverse solution by imposing additional constraints, containing *a priori* knowledge about the inverse solution. Regularization techniques usually incorporate the noise model, conductivity and movement priori to reformulate the inverse problem for a stable solution. There are different regularization techniques, such as Tikhonov Regularization, truncated Singular Value Decomposition (TSVD), and TV, which have been discussed in chapter 2 in details.

- **Solutions for the problems related to the image reconstruction algorithms**

  To resolve the lack of shape related a priori knowledge in the inverse problem, there is the need to be flexible in representing the shapes of the unknown structures. One promising approach to flexibly represent shapes is the level set technique which has also been applied in this thesis. The LS technique has gained a noticeable attention in a variety of different applications ranging from computer vision, image enhancement and segmentation to microchip fabrication. The LS has been applied for image reconstruction in linear inverse problems, such as x-ray CT, PET, SPECT as well as in nonlinear inverse problems, such as microwave imaging, nondestructive imaging, near-infrared imaging, and EIT. The representation of LS as part of a solution scheme for ill-posed inverse problems is desirable because of the high potential of LS in reconstructing 2D or 3D images from minimal available data. The LSRM considers the topological information of structures unknown, without the need for knowing the number and the origin of the structures, and rebuilds the structures using the evolution of a level set function. In chapter 5 of this thesis, a new variant of the LSRM in difference mode is proposed and its performance is assessed over EIT simulated

and human lung data.

To resolve the smoothness of the reconstructed image, the sum of absolutes, or L1 norms, can be considered as an alternative to the least squares, or the L2 norms. The L1 norms provide higher robustness against outliers and noise when compared with a L2 norm based regularization method, such as the Tikhonov regularization method. However, the application of the L1 norms is not without cost. Indeed, the computational cost for the minimization of a L1 norm based optimization problem is high. The challenge is that the L1 norms are not differentiable at the points where their arguments are equal to zero. Therefore, it is necessary to apply a minimization framework in order to reformulate the minimization of the L1 norm based regularization methods in a way to make the derivative possible. The primal-dual interior point method (PDIPM) was currently proposed as a minimization framework for the L1 norms (Borsic and Adler, 2012). In chapter 7 of this thesis, a novel variant of the PDIPM, named LS based PDIPM (LSPDIPM), to minimize the L1 norm based functionals in an LSRM is proposed.

There are two primary reconstruction types in EIT: 1) Absolute (static) imaging which attempts to recover an estimate of the absolute conductivity of the medium from the measured data frame, and 2) Difference imaging which attempts to recover an estimate of the change in conductivity between two times based on the change between two data frames. Because of the advantage of the difference EIT in producing fairly robust image against the measurement noise, the difference EIT image reconstruction has been used throughout this thesis. There is a reference conductivity σ_0 and a current conductivity σ_t at time t. Difference EIT reconstructs $\sigma_t - \sigma_0$. To reconstruct a difference image, the difference potentials are calculated as $\mathbf{y} = \mathbf{v}_t - \mathbf{v}_0$, where $\mathbf{v}_t$ is the voltage measured at time t, t is the time index, and $\mathbf{v}_0$ is the voltage average over the several number of measurements

taken when there is no movement in the medium and the noise level is considerably low.

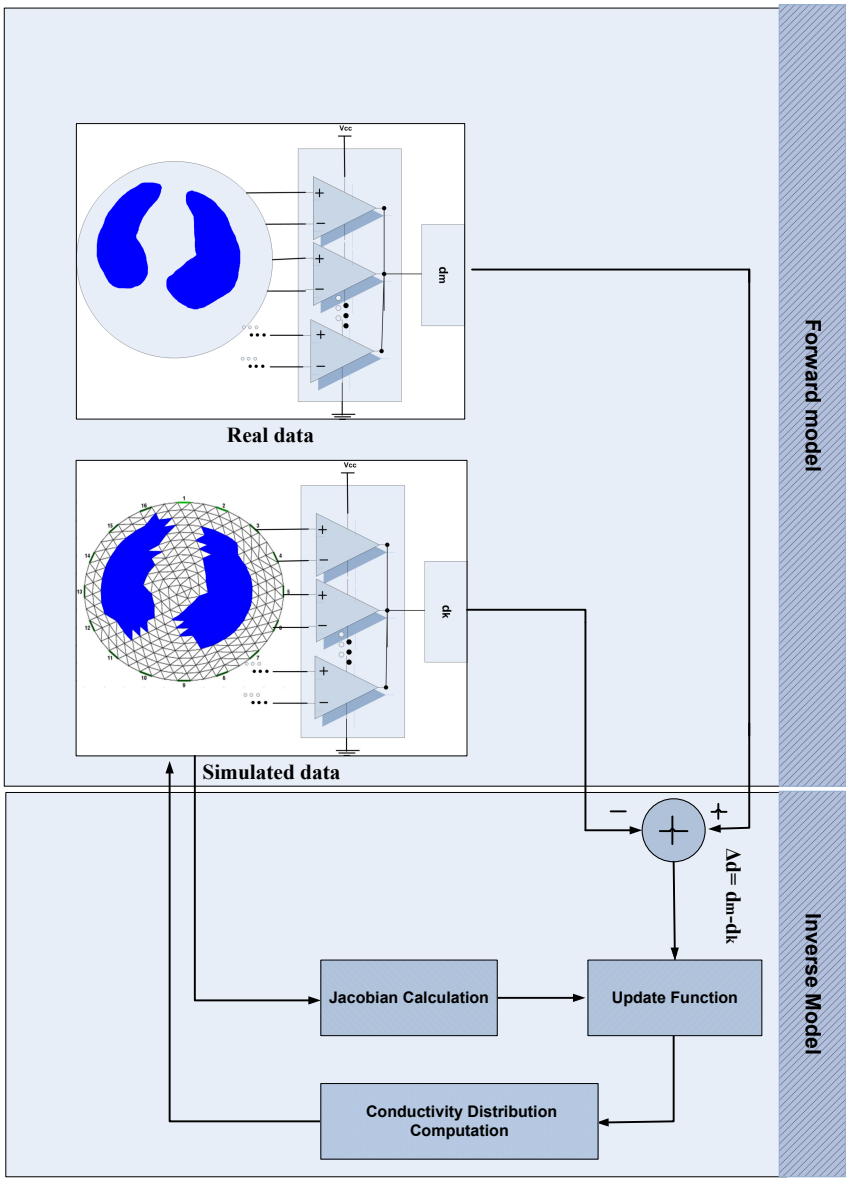

Figure 3.2: EIT difference image reconstruction algorithm.

3.3.2 Forward model

The EIT forward problem is defined over a medium Ω with a closed boundary $\partial\Omega$, an isotropic conductivity distribution $\sigma(x, y, z) = \sigma(r)$, and the potential distribution of $\phi(r)$ (Tarantola, 2005). An elliptic partial differential equation (PDE), or equally a Laplace's equation, relates $m(r)$ and $\phi(r)$ with the assumption of no internal current source inside the medium:

$$\nabla \cdot m\nabla \phi = \nabla \cdot (\mathbf{J}) = 0 \tag{3.1}$$

where $\mathbf{J}$ is the current density. A numerical technique is required to solve (3.1). Finite Element Method (FEM) as an advanced numerical method is used in EIT to convert the problem in (3.1) into a system of linear equations. In FEM, the domain of the problem is divided into several smaller regions, called elements. The connected elements are named a mesh. A node is the cross point of two or more elements. The problem is solved within the region of each element and therefore each element incorporates a portion of the whole solution over its domain. An expansion function, controlled by a set of node values, determines the values over an element and is zero elsewhere. A system matrix h is constructed from the integration of element matrices which includes the value over each element. Given the conductivity distribution inside the medium and the injecting current, the forward solution of an EIT, which is the voltage distribution within the medium, can be calculated using FEM. The forward solution (potential distribution) shows the expected voltage values at the boundary and anywhere inside the medium, given the injecting current and the conductivities. In EIT data simulation, the forward model is first solved for the voltage distribution and then the inverse problem is solved to determine the conductivity distribution when knowing the applied currents and the voltage distribution, achieved from the forward model. By solving (3.1) for the potential distribution ϕ, the EIT nonlinear

forward model is written as follows (Tarantola, 2005):

$$d = h(\sigma) \tag{3.2}$$

where $\sigma \in \mathbb{R}^N$, N is the number of the elements in the mesh, σ is the vector of the conductivity quantities inside the medium, and d is the forward solution (potential values at the boundary), and h is the system matrix or the forward conversion function.

A linearized forward problem is written when there is a small variation around σ as follows (Tarantola, 2005):

$$d = J\sigma + n \tag{3.3}$$

where n is the uncorrelated, white Gaussian noise in the medium, J is the Jacobian matrix (sensitivity matrix), σ is the conductivity distribution in the medium, and d is the forward solution which are the voltage values at the boundary of the medium. The Jacobian matrix has a dimension of n_M by n_E. Jacobian matrix J can be calculated as follows: A small conductivity change $\delta\sigma_j$ at the j^{th} element in the mesh is formed to capture the voltage change δd_i caused on the i^{th} measurement at the boundary of the medium. The entry indexed as i, j in the Jacobian matrix is calculated as follows (Tarantola, 2005):

$$J_{ij} = \frac{\delta d_i}{\delta \sigma_j}|_{m_0} \tag{3.4}$$

where σ_0 is the background conductivity.

3.3.3 Inverse model

Inverse model intend to identify unknown parameters in a system from a set of measurement. In EIT, the electrical conductivities of a medium are the unknown parameters

and the known measurements are the surface potentials at the boundary of the medium, achieved from the forward model. EIT uses FEM to determine the optimal solution (conductivity distribution within the medium). EIT divides the medium into small elements, and looks for the solution within the small elements. The inverse solution is the value of the conductivity for each element when the stimulating current and the surface voltages are known.

The EIT inverse problem occurs when the conductivity distribution σ is calculated by inversing the forward problem in (3.3). Therefore, the EIT inverse problem can be written as follows (Tarantola, 2005):

$$\hat{\sigma} = J^{-1}d \tag{3.5}$$

The inverse solution in (3.5) is not available because the Jacobian matrix is not a square matrix and invertible. A least squares error function $\|J\sigma - d\|$ can be minimized to linearly find the inversion solution in (3.5) as below (Tarantola, 2005):

$$\hat{\sigma} = \left(J^T J\right)^{-1} J^T d \tag{3.6}$$

The inverse solution in (3.6) is rank-deficient, meaning that the number of the unknown conductivity values is much higher than that of voltage measurements at the boundary. The rank-deficiency in EIT reconstruction makes the problem to be under-determined, meaning that the problem has infinite solutions. The regularization techniques help producing stable inverse solutions which are discussed in the following.

The regularization techniques usually incorporate the noise model, conductivity and movement prior to reformulating the inverse problem for a stable solution. Chapter 2 discusses different regularization techniques, such as Tikhonov Regularization, GN, and TV. Tikhonov regularization is one of the most common regularization technique which is

also applied in EIT image reconstruction applications. In the following subsection, EIT image reconstruction using Tikhonov regularization is described.

3.3.4 EIT image reconstruction using Tikhonov regularization term

Tikhonov regularization is one of the most common regularization techniques using the sum of quadratic norms of the data mismatch and the regularization term. In the linear case, the inverse solution using Tikhonov regularization method is determined by minimizing the following quadratic norm over the data mismatch and the regularization term with respect to the conductivity change (Tarantola, 2005):

$$\hat{\sigma} = \underset{\sigma}{\operatorname{argmin}} \left[\|J\sigma - d\|^2 + \lambda^2 \|\sigma - \sigma_0\|^2 \right] \tag{3.7}$$

where $\lambda = \frac{\sigma_n}{\sigma_\sigma}$ is a hyperparameter (or regularization parameter) that determines the trade-off between the spatial resolution and noise. σ_σ and σ_n are standard deviation of the unknowns σ and standard deviation of the noise, respectively. σ_0 is the "reasonable" image known*a priori*. As shown in chapter 2, the inverse solution is achieved by taking derivative of the above equation as follows:

$$\hat{\sigma} = \left(J^T J + \lambda^2 I \right)^{-1} J^T d \tag{3.8}$$

where I is the unit matrix. In (3.8), $\hat{\sigma}$ is the solution of Tikhonov regularization. EIT image reconstruction using iterative GN for a non-linear inverse problem is derived in subsection 2.3.4 in chapter 2.

3.4 EIT current streamlines, equipotentials, and sensitivity to conductivity changes

In this section, the EIT potential, current streamlines, equipotentials, and sensitivity to conductivity changes (Jacobian) within a homogeneous medium are studied.

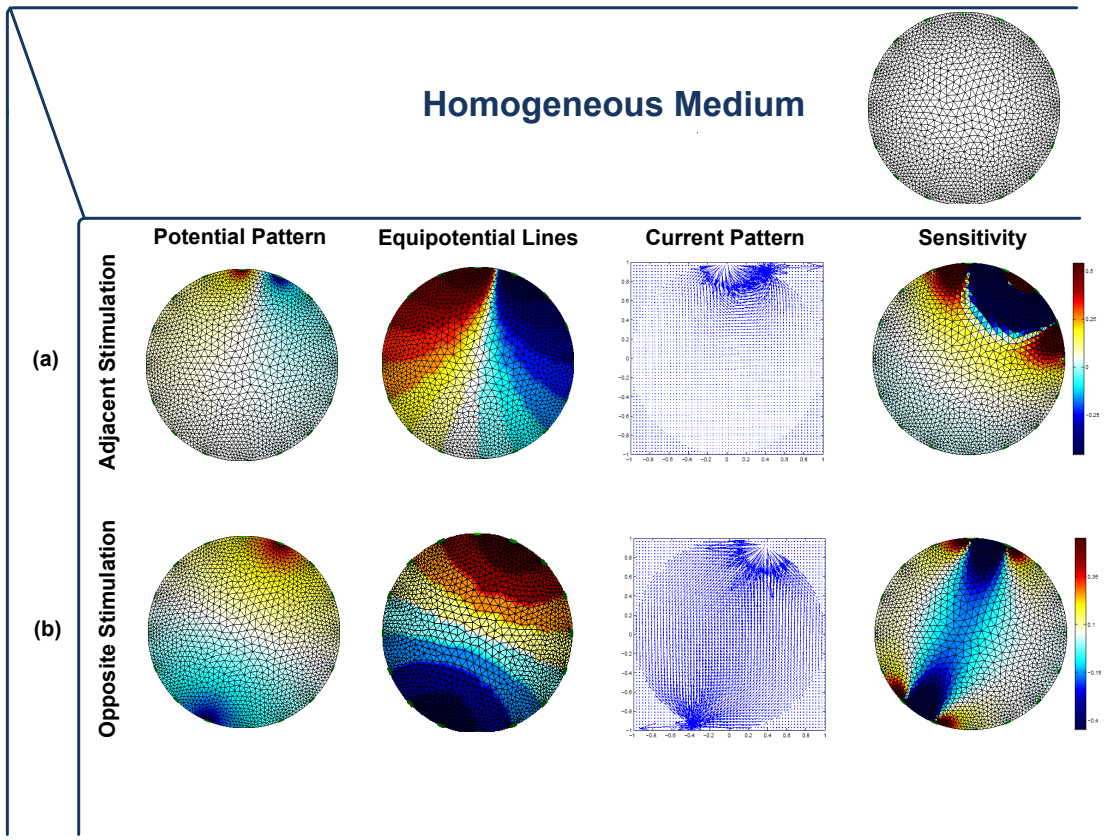

Figure 3.3: EIT potential, current streamlines, and sensitivity patterns calculated for adjacent and opposite current stimulation in a homogeneous medium.

Figure 3.3 shows the potential pattern, current streamlines, the equipotentials, and the EIT sensitivity for the adjacent and opposite current stimulation patterns in a homogeneous medium. The color map used to show the potential distribution within medium shows the high potential values in dark red and the lowest ones in dark blue. As it is shown, the potential distribution within the medium depends on the current stimulation pattern. The

current stimulation pattern also affects the distribution of the equipotential lines inside the medium. The EIT sensitivity is higher in the center of the medium for the opposite current stimulation when compared with the sensitivity pattern for the adjacent current stimulation. This is because in the adjacent current stimulation, the current streams close to the injecting electrode pairs at the surface of the medium. Therefore, the sensitivity of the EIT system to conductivity changes in the center of the medium becomes low. For instance in an experiment to monitor a small object moving from the boundary of the medium to the center, the EIT reconstructed image becomes highly blurred when the object approaches the center of the medium.

In figure 3.4, the current patterns are shown for a low conductive object when either an adjacent stimulation pattern (figure 3.4(a)) or an opposite stimulation pattern (figure 3.4 (b)) is applied. Due to the sharp conductivity gradient between the background and the inclusion, the current streamlines are deviated at the interface. The first column of figure 3.4 shows both the EIT signal for a homogeneous medium (v_h) in blue and the EIT signal for a non-homogeneous medium (v_i) in green. The EIT difference signal (v_h-v_i) is shown in red. The EIT difference image reconstruction algorithm measures the EIT difference signals and applies them in an inverse problem to reconstruct the conductivity changes within the medium. The EIT difference signals for an opposite current stimulation are shown in figure 3.4 (b).

Figure 3.5 shows the same measurements, calculated for figure 3.4, for a highly conductive object in the medium. The current patterns show that the density of the current streamlines is higher at the boundary of the highly conductive object than that of the current streamlines in the background. The general pattern of the EIT difference signals for the conductive and non-conductive objects shows small changes; however, the amplitude of the difference signal differs according to the conductivity quantity of the object.

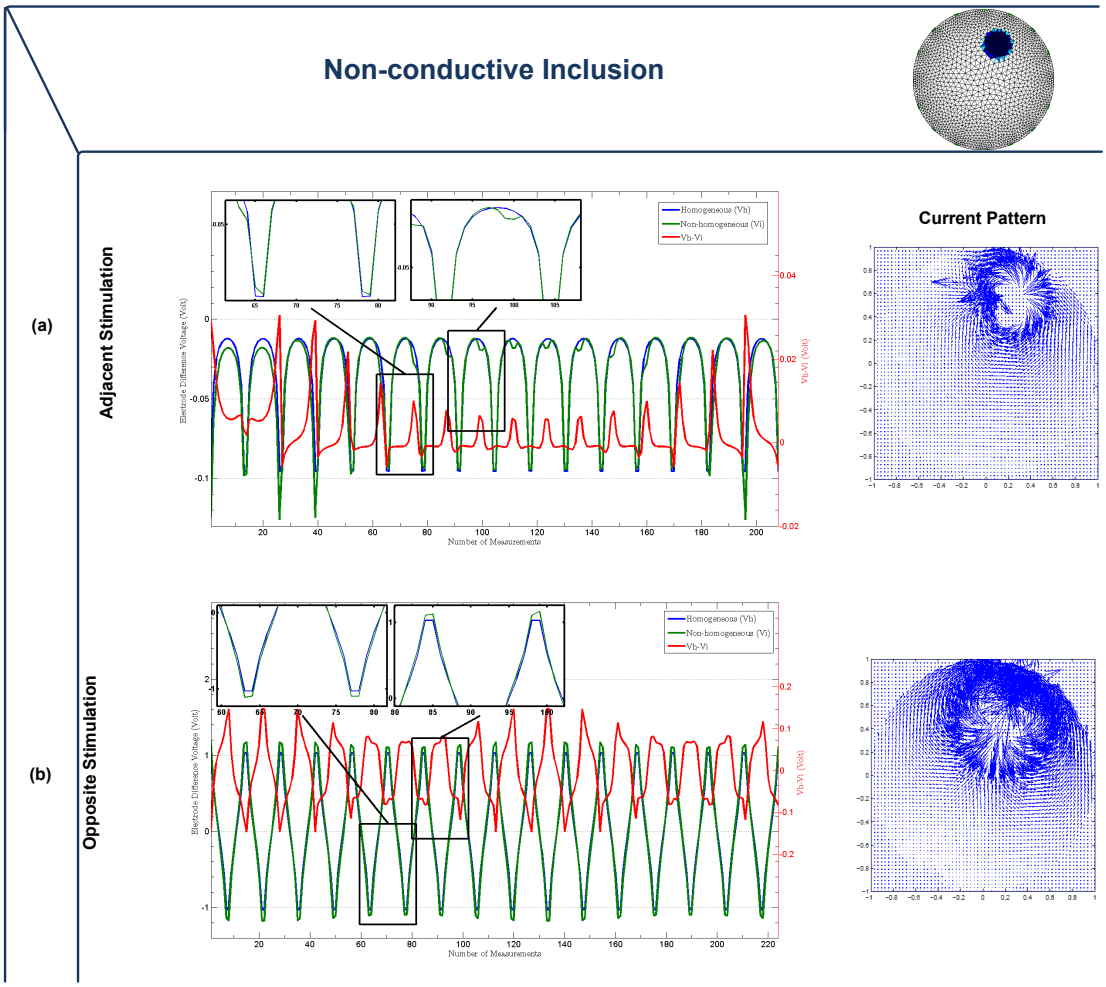

Figure 3.4: EIT potential, current streamlines, and sensitivity patterns calculated for adjacent and opposite current stimulation in a medium with low conductive inclusion.

Figure 3.6 represents a cross section of a human thorax taken using X-ray CT. The current stream lines through the lungs and the heart are calculated and shown with the blue lines. The current stream lines are bent at the interface between the lungs and the heart because of the change in the conductivity of the tissues. The calculated equipotentials are also demonstrated with black lines.

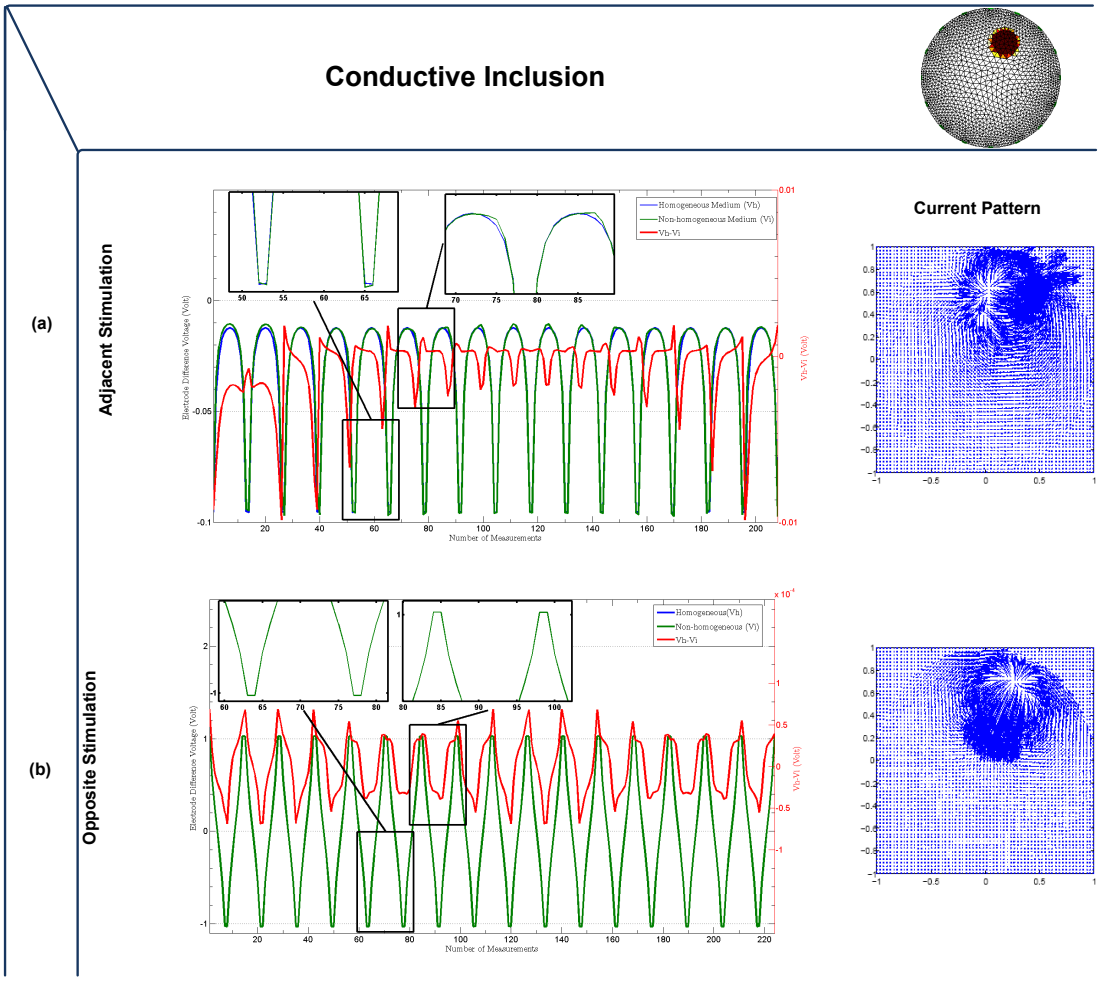

Figure 3.5: EIT potential, current streamlines, and sensitivity patterns calculated for adjacent and opposite current stimulation in a medium with highly conductive inclusion.

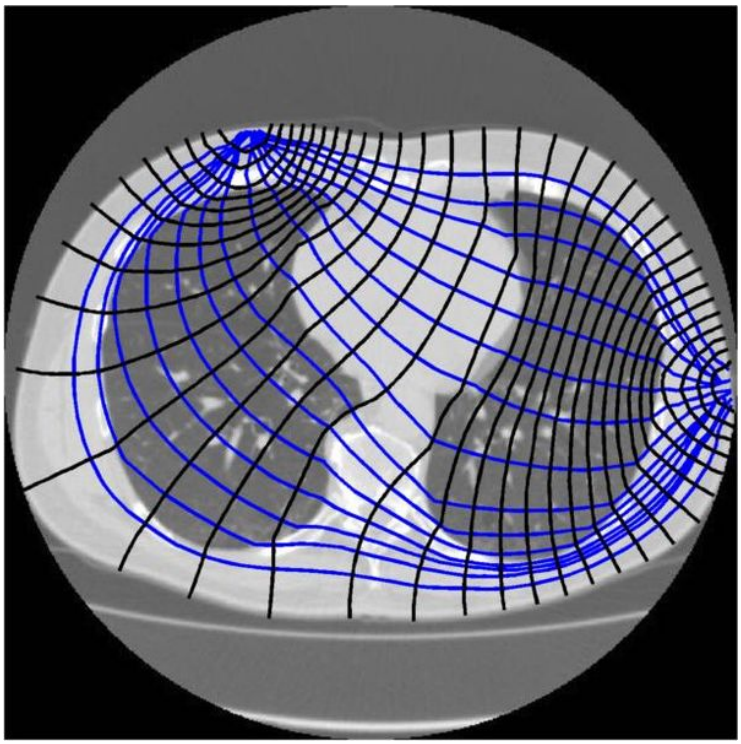

Figure 3.6: The equipotentials (black lines) and current stream lines (blue lines) calculated for a human thorax.

Chapter 4

Lung Physiology

4.1 Summary

This thesis shows the first clinical results of applying the proposed EPIRM to reconstruct the air distribution inside the lungs during the incremental Positive End-Expiratory Pressure (PEEP) trial. The clinical data applied in this thesis was acquired from mechanically ventilated patients with healthy lungs and ALI. The aim of this chapter is to review related topics regarding the human respiratory system in order to explore the mechanical and physiological behaviour of the lungs. To realize the aforementioned objective, the following topics are discussed in this chapter: Lung physiology, lung mechanics, lung function tests, and lung related diseases, such as acute respiratory distress syndrome (ARDS), its pathophysiology, treatment options, and the obstacles.

4.2 Lung physiology

The respiratory system consists of two portions: 1) the upper respiratory system, 2) the lower respiratory system (Grabowski, 2000). The upper respiratory system filters, warms and moistens air and conducts the air into the lungs. The upper section of the respiratory system includes the nose, and the pharynx. The lower respiratory system includes larynx, trachea, bronchi, and lungs. The functional respiratory portion consists of the respiratory bronchioles, alveolar ducts, alveolar sacs, and alveoli, where the gas exchange between air and blood occurs. The pharynx, or throat, is a funnel shaped tube approximately 13 cm in length. The function of the pharynx is to conduct the air and food as well as to act as a resonating chamber for speech sounds. The tonsils in the pharynx reinforce the immunity system of the body against foreign invaders. The larynx, or voice box, is a short passageway that connects the pharynx to the trachea. The duty of the larynx is to produce the voice. The trachea is a 12 cm long tubular passageway to conduct the air to the right and left primary bronchi. Figure 1 shows the anterior view of the upper respiratory system and the lower respiratory system.

Figure 2 represents the anterior view of the airway branching from the trachea to the terminal bronchioles. The right primary bronchus is shorter, more vertical and wider than the left primary bronchus (Grabowski, 2000). The right primary bronchus goes into the right lung and the left primary bronchus goes into the left lung. The carina is the point where the trachea divides into right and left primary bronchi. For each lobe of the lung, the smaller bronchi are called secondary bronchi. The right lung has three lobes while the left lung has two (Grabowski, 2000).

The tertiary bronchi are smaller than secondary ones and divide into several smaller branches called terminal bronchioles. The extension of the bronchioles into smaller branches is referred to as the bronchial tree, which resembles an inverted tree. The lungs are lo-

cated in the thoracic cavity and are separated from each other by the heart. The pleural membrane encloses and protects the lungs. The parietal pleura are the layer that lines the wall of the thoracic cavity and the visceral pleura cover the lungs. The pleural cavity is the small space between the visceral and parietal pleurae. To reduce the friction between the membranes during the breathing, there is some lubricating fluid, secreted by the membranes, in the pleural cavity (Grabowski, 2000).

Figure 3 represents the lung lobes from different views. The broad inferior portion of the lung which fits over the convex area of the diaphragm is the base (Grabowski, 2000). The narrow superior portion of the lung is the apex. Fissures divide the lungs into lobes. The oblique fissure extends inferiorly and anteriorly. The superior lobe is separated from the inferior lobe by the oblique fissure in the left lung. The horizontal fissure only exists in the right lung. The superior lobe of the right lung is subdivided by the horizontal fissure, forming a middle lobe. Each lobe of the lungs receives a separate secondary bronchus. Thus, the right primary bronchus has three secondary bronchi: the superior, middle, and inferior secondary bronchi. The left primary bronchus has two secondary bronchi: superior and inferior secondary bronchi. The secondary bronchi give rise to the tertiary bronchi in each lung. Lobules are very small compartments wrapped in elastic connective tissue and include a lymphatic vessel, an arteriole, a venule, and a branch from a terminal bronchiole (Lumb, 2005). The terminal bronchioles subdivide into microscopic branches called respiratory bronchioles. The respiratory bronchioles subdivide into several alveolar ducts. There are about 25 orders of branching from trachea to the alveolar ducts including primary bronchi (first order branching), secondary bronchi (second order branching), and so on down to the alveolar ducts (Lumb, 2005).

Figure 4 (a) shows a diagram of the lower part of lung. Figure 4(b) depicts alveolar sac and the components of an alveolus. The alveolar ducts are connected to numerous alveoli

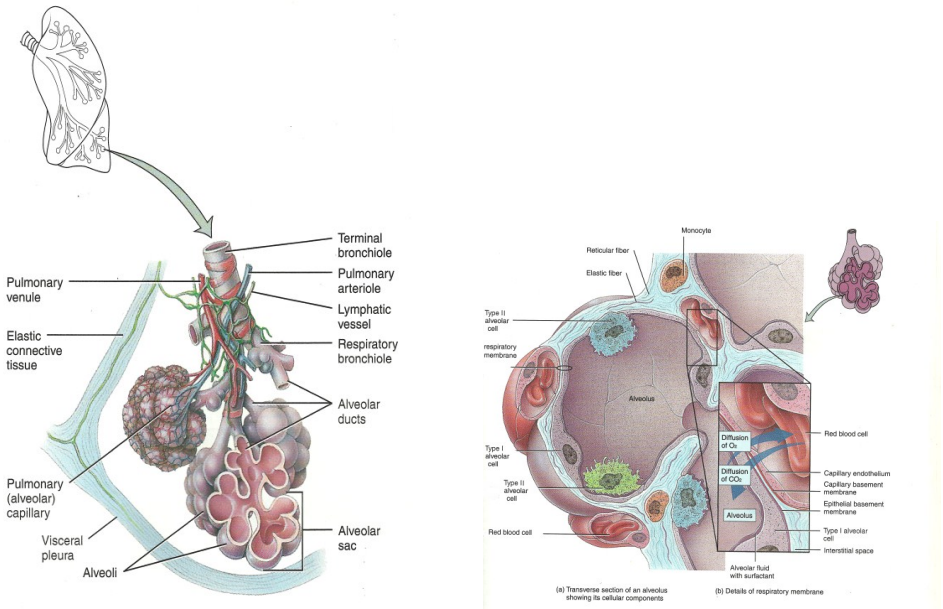

(a) (b)

Figure 4.1: Representation of alveolus structure. a) Diagram of a portion of the lung. b) Alveolus structural components applied in gases exchange. The image is reproduced from (Grabowski, 2000).

and alveolar sacs. An alveolus is a cup-shaped membrane with very thin wall. The wall of the alveoli consists of two types of alveolar epithelial cells (Grabowski, 2000). Type I alveolar cells create the lining of the alveolar wall, and the main site of gas exchange occurs in this type of cells (Grabowski, 2000). The alveolar wall is occasionally interrupted by type II alveolar cells, which are also called septal cells. The alveolar fluid decreases the friction between the surface of the cells and the air (Lumb, 2005). Surfactant, included in the alveolar fluid, keeps the alveoli elastic, reducing the tendency of the alveoli to collapse (Grabowski, 2000). The reticular fiber and elastic fiber are in the alveolar spaces to keep the elasticity of the alveoli. Alveolar macrophages (dust cells) remove fine dust particles which may be in the alveolar spaces (Grotberg, 2004). The diffusion across alveolar and capillary walls causes the exchange of oxygen and carbon dioxide in the interface of the alveoli and the capillary (Grotberg, 2004). The respiratory membrane, which is the site of

gas diffusion, consists of four layers: The first layer contains the type I and type II alveolar cells and associated alveolar macrophages, which constitutes the alveolar wall (Grabowski, 2000; West, 2005). The second layer is an epithelial basement membrane located under the alveolar wall. The third layer is a capillary basement membrane which is fused to the epithelial basement membrane, and the last layer is the endothelial cells of the capillary. Nevertheless, the thickness of the respiratory membrane is very small, about one sixteenth the diameter of a red blood cell. The thin respiratory membrane allows rapid gas diffusion and also allows having 300 million alveoli in the lungs, giving alveoli surface area of 70 square meters for gas exchange (Grabowski, 2000).

The lungs receive the deoxygenated blood from the right ventricle, one of the two lower chambers of the heart, through pulmonary arteries. The oxygenated blood, after gas exchange in the capillaries, drains into the left atrium, one of the two upper chambers of the heart, through the pulmonary veins. In the case of low oxygen level in the body tissue (hypoxia), the dilation of blood vessels causes the increase in the blood flow to the tissue with low oxygen intake (Kutz et al., 2003). However in the case of hypoxia in the lungs, the vasoconstriction diverts pulmonary blood from poorly ventilated areas, or collapsed regions, to well-ventilated regions of the lungs (Kutz et al., 2003).

The process of gas exchange between the atmosphere and lung alveoli is called pulmonary ventilation, breathing (Grabowski, 2000). The air always flows from a region of higher pressure to a region of lower pressure. The respiratory muscles produce an alternating pressure difference between the atmosphere and the lungs. The change in the pressure between the atmosphere and the lungs causes the air flows in and out of the lungs (breath in and out) (Grabowski, 2000).

The process of breathing in is called inspiration or inhalation. Inspiration occurs when the air pressure inside the lungs is less than the air pressure outside in the atmosphere.

Inspiration causes an increase in the volume of the lungs. The main respiratory muscle is called the diaphragm. The diaphragm is a dome-shaped muscle located in the bottom of the thoracic cavity. The contraction of the diaphragm causes it to flatten, creating an increase in the volume of the cavity which allows the lungs to expand for breathing in. A normal quiet inspiration descends the diaphragm about 1 cm with a pressure difference of 1-3 mm Hg and the inhalation of 500 mL of air. While a vigorous inhalation causes the diaphragm to descend for 10 cm with a pressure different of 100 mm Hg and the inhalation of 2-3 liters of air.

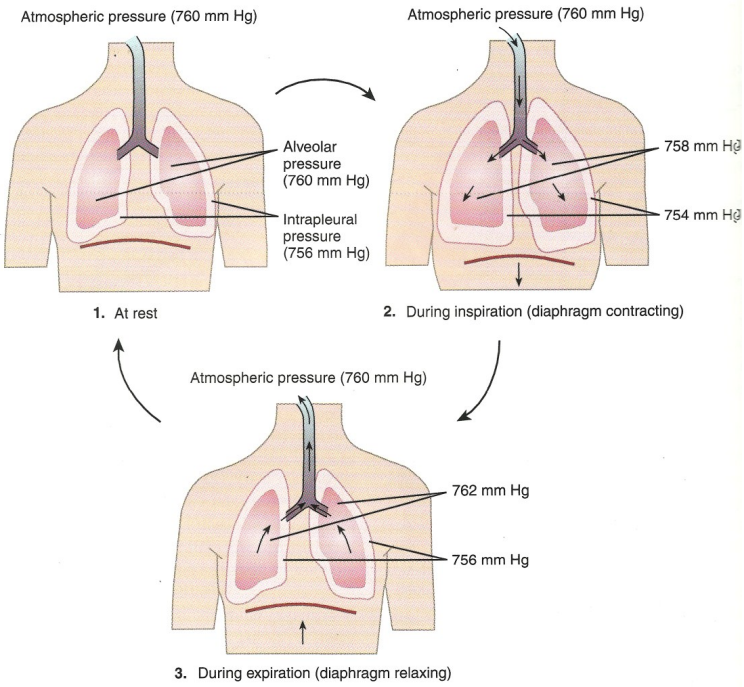

Figure 4.2: Pressure changes in the pulmonary ventilation in three different conditions: at rest, inspiration and expiration. The image is reproduced from (Grabowski, 2000).

Expiration (exhalation) occurs when the pressure in the lungs is greater than the pressure of the atmosphere. Air flows from the area of higher pressure in the alveoli to the area of lower pressure in the atmosphere. Unlike an inhalation, there is no muscular contraction in the normal, unforced expiration. Instead there exists elastic recoil. The elastic recoil

happens in the chest wall and lungs to spring back the expanded chest in the inhalation phase. There are two forces contributed to the elastic recoil: the recoil of the stretched elastic fibers, located in the alveoli spaces, during the inhalation phase, and the inward pull of surface tension due to the layer of alveolar fluid. Figure 5 shows the pressure changes in pulmonary ventilation at three stages: at rest, inspiration, and expiration.

The alveolar surface tension, the amount of the alveoli elasticity (compliance of the lungs) , and the resistivity of the air passageway (air resistance) are three main components which determine the rate of air flow and the amount of effort needed for breathing. The alveolar surface tension is because of the strong molecular attachment of the alveolar fluid when compared to the molecular attachment of the air around the alveoli. The molecular attachment gradient in the interface of air-water in the alveolar causes an inwardly directed force which enforces the alveoli to take the smallest possible diameter in the rest. The surfactant in the alveolar fluid reduces the surface tension of the alveolar fluid to be lower than that of pure water. A common disease in premature infants is respiratory distress syndrome where a deficiency of surfactant causes the surface tension of alveolar fluid to become very high. The increase of the alveoli surface tension leads to the production of so many collapsed regions in the lungs due to the incapability of the alveoli to spring back after an exhalation.

Compliance is a measure of lung elasticity and depends on two factors: elasticity and surface tension. The elastic fibers present in the lung tissue cause the lung to easily expand, and the surfactant in the alveolar fluid prevents the alveoli to collapse through reducing the surface tension.

The wall of the airways, for example in the trachea and the bronchioles, shows resistivity to the normal flow of air into and out of the lungs. Airflow is proportional to the pressure

difference between the atmosphere and the lungs and is inversely associated to the airway resistance. This means that to have a higher airflow, there needs to be either lower air resistance or a higher pressure gradient. The diameter of the airways mainly determines the amount of resistivity. In the inhalation phase, the diameter of the bronchioles increases to easily conduct the air into the alveoli. However in the exhalation phase, the airway resistance of the bronchioles increases as the diameter of the bronchioles decreases.

The blood transfers oxygen and carbon dioxide in the body. Oxygen is not dissolvable in water and about 1.5 % of oxygen is dissolved in the blood plasma (Grabowski, 2000). The remaining oxygen contributes in chemical combination with haemoglobin inside red blood cells. Four molecules of oxygen can bind to one haemoglobin molecule. The combination of oxygen and haemoglobin forms oxyhemoglobin. The haemoglobin is fully saturated when it is completely converted to oxyhemoblobin, meaning that all four capacities of the hemoglobin are bound with oxygen molecules. One of the most important factors determining how much oxygen combines with hemoglobin is the pressure of oxygen in the pulmonary capillaries. The higher the pressure of oxygen, the more oxygen will combine with hemoglobin (Kutz et al., 2003). The oxygen-hemoglobin dissociation curve is shown in figure 6. The curve profile represents the relationship between hemoglobin saturation and the pressure of oxygen at normal body temperature. In the pulmonary capillaries, the pressure of oxygen is in its highest value during the inhalation phase and therefore, a large amount of oxygen binds with hemoglobin to produce fully saturated hemoglobin (Kutz et al., 2003). In the tissue cells, the pressure of oxygen is low and the hemoglobin releases oxygen molecules through diffusion (Grabowski, 2000; Kutz et al., 2003). A large drop in the oxygen pressure leads to a maximum delivery of oxygen to highly active muscles. A small amount of carbon dioxide flows in its original form in the blood stream and a slightly larger amount of carbon dioxide enters the plasma and bonds with hemoglobin, forming

bicarbonate. In the tissue cells, the pressure of carbon dioxide is high and this leads to having higher carbonate. However in the pulmonary capillaries, the pressure of carbon dioxide is low, thus there are a lot of molecules of released carbon dioxide diffusing into the alveoli for exhalation (Kutz et al., 2003).

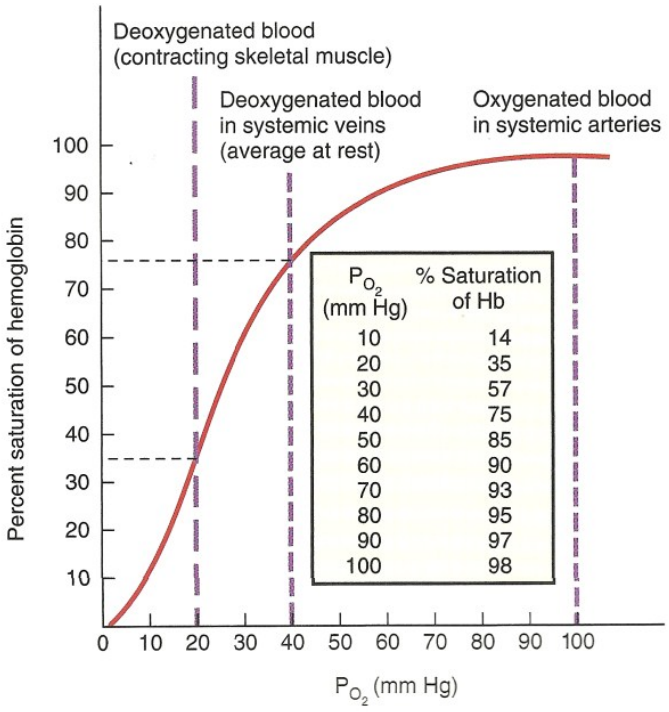

Figure 4.3: The oxygen-hemoglobin dissociation curve. The image is reproduced from (Grabowski, 2000).

4.3 Lung mechanics

Airway resistance and lung compliance are the two most commonly used variables to assess the mechanics of the lungs (Moussavi, 2006). The health condition of the respiratory system depends on these parameters and they maybe affected by different diseases, disrupting the normal function of the respiratory system. The corresponding variables for the airway

resistance, the pressure, and the airflow in the electrical equivalent circuit are as follows: the electrical resistance, the voltage, and the electrical current (Moussavi, 2006). Therefore, the airway resistance is the pressure (voltage) over the airflow (current). The airway resistance is inversely proportional to the fourth power of the radius of the airway. The airway resistance is defined as follows (Moussavi, 2006; Grotberg, 2004):

$$R_{airway} = \frac{P_{mouth} - P_{alveoli}}{\hat{V}}, \tag{4.1}$$

where P_{mouth} is the pressure at the mouth (cmH_2O), $P_{alveoli}$ is the pressure at the alveoli (cmH_2O), and $\hat{V}$ is the airflow (liter/sec). The airway resistance increases as the radius of the airway decreases. Nevertheless, the airway resistance of the alveoli is much lower than that of the trachea. This is because the bronchi tree has many branches in parallel making the net effective resistance of the tree to be much less than that of the trachea (Moussavi, 2006).

Obstructive lungs diseases, such as asthma and bronchitis, mostly affect the alveoli and the smaller bronchi and bronchioles, increasing the airway resistance (Grotberg, 2004). In chronic asthma, the inflammation of the bronchial epithelial cells, the accumulation of fluid in the alveoli (edema), and the increased secretion of mucus in the air passageway (fibrosis) are common effects. In chronic bronchitis, the increased mucus secretion blocks the airway and increases the airway resistance to the air flow (Grotberg, 2004).

The lung compliance C ($liter/cmH_2O$), indicating how elastic the lung is to be expanded or retracted, is defined as follows (Moussavi, 2006):

$$C = \frac{\delta V}{\delta P}, \tag{4.2}$$

where V is the change in the volume in liters, and P is the change in the pressure in cmH_2O. Fibrosis causes the lungs to become stiff, decreasing the lung compliance (Bourke, 2003a). The diffused liquid in the alveoli makes the alveoli walls thicker with low compliance. To keep a normal lung volume, there will be larger pressure required (Bourke, 2003a). The normal breath demands more effort and the patient commonly experiences shortness of breath. In contrast, emphysema, which is a smoking related disease, causes the alveolar walls to break down, making the lung compliance high. This enlarges the alveoli and inflates the lungs by small increases in the pressure. In chronic emphysema, part of the alveoli is degenerated and can not contribute to ventilation (Bourke, 2003a). The enlarged alveoli do not inflate during inspiration, and therefore collapse during expiration.

Because of the gravitational effect on the lungs, the upper parts of the lungs are less receptive (compliant) to air entry during the inhalation, compared to the dependent parts (lower parts) of the lungs. The difference in the lung compliance and the airway resistance to airflow for upper and lower parts of the normal lungs is small; however, the difference increases for diseased lungs (Bourke, 2003b). Therefore, the lower parts of the lungs contribute more in ventilation. The relationship between the volume-pressure is different during the inspiration and expiration so that the volume-pressure curve represents a hysteresis loop, shown in figure 7. The reason for the hysteresis is firstly because of the inherent behaviour of the lung tissue in the expansion and the retraction, and secondly the fact that the intrapleural pressure in the apex and in the bottom part of the lungs (dependent region) is different (Bourke, 2003a). The lower part of the lungs has smaller intrapleural pressure, because of the different effect of the gravity on the different regions of the lungs, than the upper part (Bourke, 2003a). Therefore, the lower part of the lungs expands first with the increase in the pressure and the upper part inflates with the lower part after the pressure is higher than the apex intrapleural pressure. Lung compliance has

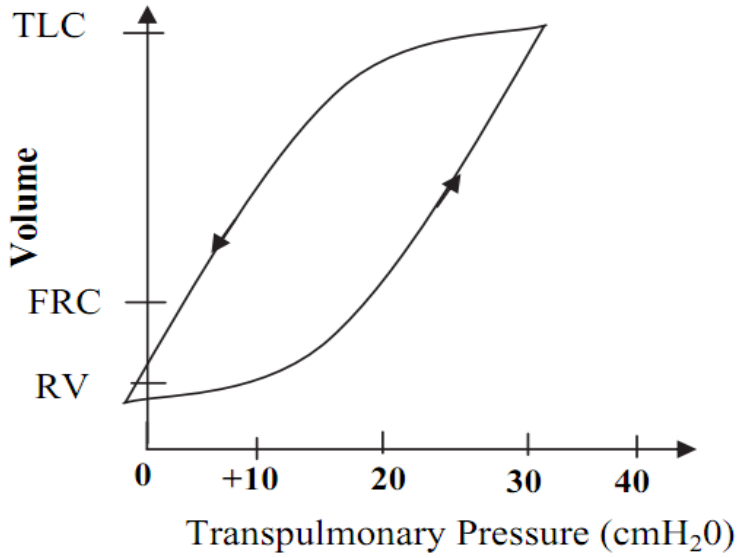

Figure 4.4: The hysteresis in the volume-pressure curve for the inspiration and the expiration. The image is reproduced from (Moussavi, 2006).

its highest value at rest and becomes smaller as the volume increases with the increase in the pressure (Moussavi, 2006). Therefore, it is easier to breathe in the volume where the lungs experience the high values for compliance.

4.4 Lung function tests

The quality of breathing is checked through lung function tests (also called pulmonary function tests) (West, 2005; Lumb, 2005). The objective of the tests are 1) determining how much air lungs can hold, 2) how quickly air can move in and out of lungs, 3) how well the gas exchange between the alveoli and the vessels is (the quality of putting oxygen into and removing carbon dioxide from your blood), and 4) how strong the breathing muscles are (West, 2005; Lumb, 2005). The common lung function tests include: spirometry, residual volume, gas diffusion tests, body plethysmography, inhalation challenge tests, and exercise stress tests (West, 2005; Lumb, 2005).

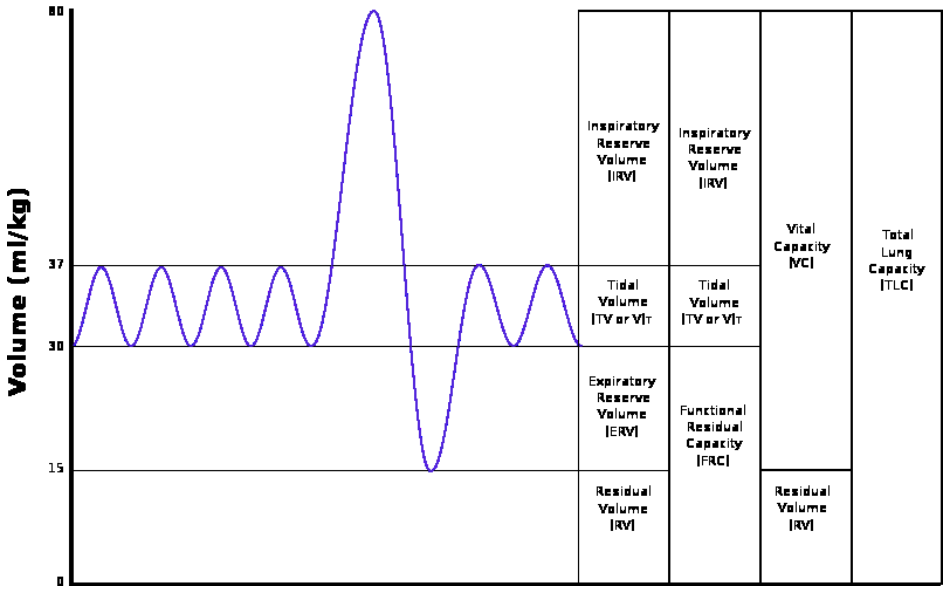

Figure 4.5: The different lung volume during the normal ventilation and maximally ventilation. The image is reproduced from (Lumb, 2005).

Spirometry is one of the most commonly performed lung function tests (Lumb, 2005). It measures both the amount and the speed of air moving out of the lungs (Lumb, 2005). The patient breathes into a mouthpiece while his breathing is recorded by the spirometer. A spirogram shows the recorded breathing information. The spirometry measures the following lung function values (West, 2005; Lumb, 2005): 1) Forced vital capacity (FVC), which measures the air amount one can exhale after as deep inhalation as possible. 2) Forced expiratory volume (FEV), which measures the maximum air amount one can exhale in one breath. 3) Forced expiratory flow (FEF), which measures the air amount halfway through an exhale. 4) Peak expiratory flow (PEF), which is the amount of air exhaled in one breath with force which is measured at the same time as forced vital capacity (FVC). 5) Maximum voluntary ventilation (MVV), which is the highest air amount one can breathe in and out during one minute. 6) Slow vital capacity (SVC), which is the measurement of air amount one can slowly exhale after as deep inhalation as possible. 7) Total lung capacity (TLC), which is the air amount inside lungs after a maximally deep inhalation.

8) Functional residual capacity (FRC), which is the amount of air in the lungs after a normal exhalation. 9) Residual volume (RV), which is the amount of air in the lungs after a maximally deep exhalation, The RV can be measured through helium or nitrogen gas dilution. 10) Expiratory reserve volume (ERV), which is the difference between the FRC and the RV. The graphical demonstration of the lung volumes during the normal breathing in and out as well as maximally breathing is depicted in figure 4.5.

4.4.1 Gas diffusion tests

Gas diffusion tests measure the amount of oxygen and other gases traveling through alveoli per minute as well as the quality of the gas exchange between the alveoli and the blood vessels. Gas diffusion tests include (West, 2005; Lumb, 2005): 1) Arterial blood gases, which measures the amount of oxygen and carbon dioxide in the blood circulation system. 2) Carbon monoxide diffusion capacity (DLCO), which measures how well the lungs transfer the carbon monoxide (CO) into the blood vessels. The patient breathes through a mouthpiece containing a small amount of CO (West, 2005; Lumb, 2005). The amount of the CO in the breath the patient takes out is measured and the oxygen diffusion capacity of the lungs, how well the gas exchange happens, is estimated by knowing the CO quantity of the inhaled air and that of the exhaled air (West, 2005; Lumb, 2005).

4.4.2 Body plethysmography

This test is common when either the total lung capacity, which is the maximum air the lungs can take, or the absolute lung capacity is measured.

The patient sits inside a room called plethysmograph while breathing through a mouthpiece measuring the pressure and the air flow (West, 2005; Lumb, 2005). The TLC and the RV can be measured using the plethysmography test (Grotberg, 2004). Figure 9 shows

Figure 4.6: Body plethysmography. The image is reproduced from (Moussavi, 2006).

a plethysmography in the research laboratory of Manitoba university.

4.4.3 Inhalation challenge test

The patient who is suffering from asthma or wheezing is commonly required to complete the test (West, 2005; Lumb, 2005). The purpose of the test is to measure the response of the airways to substances that may have caused the patient to breath heavily. An increasing amount of methacholine or mannitol is inhaled by the patient through a nebulizer, which is a device used to gradually deliver the substance to the patient via a mouthpiece (West, 2005; Lumb, 2005). The lung function is monitored and recorded by the spirometer during the test (West, 2005; Lumb, 2005).

4.4.4 Exercise stress tests

The test is to monitor the lungs function during intense exercise (West, 2005; Lumb, 2005). The spirometer monitors and evaluates the breathing of the patient during exercise (West, 2005; Lumb, 2005). The function of the lungs is evaluated during the patient resting period after exercise.

4.5 Pathophysiology of acute respiratory distress syndrome (ARDS)

Diffuse alveolar damage is the main consequence of the ARDS (Bourke, 2003a). The lung epithelial cells (type I and II cells) become inflamed, and the malfunction of the epithelial cells causes the migration of the white blood cells into the inflamed alveoli, producing pulmonary edema which increases the thickness of the alveoli walls (West, 2005; Lumb, 2005). The inflamed alveoli are not able to exchange oxygen and carbon dioxide properly, leading to hypoxia (a lack of oxygen in the body, and eventually the fibrosis) (West, 2005; Lumb, 2005). The inflamed alveoli do not contribute to the lung ventilation and will eventually collapse. The collapsed alveoli are mostly seen to be distributed in the lower lobes of the lungs; however, the distribution of which is not even in the pruama (sepsis)-induced ARDS, where the collapsed alveoli are scattered and less likely to be dense in a small area (Bourke, 2003a; West, 2005; Lumb, 2005). The lung mechanics (lung compliance and airways resistance) change dramatically due to the ARDS (Bourke, 2003a). The transpulmonary pressure will be higher due to the ARDS as the airspace is less than the normal condition in the diseased alveoli. This high pulmonary pressure creates high stress on the aerated alveoli, which contributes to the lung ventilation (Bourke, 2003a). The ARDS is a form of respiratory failure causing excessive leakiness of the respiratory membranes and severe hypoxia (Grabowski, 2000).

The ARDS is a common life-threatening condition with a high mortality. Mechanical ventilation (MV) is the main means for ARDS treatment in hospitals and health care providers (Bourke, 2003a). However, improper applications of MV easily leads to mechanical ventilator-associated lung injury (VALI) and increase mortality. The setting of the MV system is different for every patient and depends on the type of the ARDS causing the

problem and the characteristics of the symptoms. An unsuccessful setting of the MV system may worsen the ARDS, inducing more fluid into the alveoli, making breathing harder at a lower tidal volume (Bourke, 2003a).

There are several lung protective ventilation strategies (LPVS) to prevent the VALI in patients in need of the MV (Bourke, 2003a). There is still the need to investigate further into an easy to use and maintain LPVS. A continuous, non-invasive monitoring of the air distribution in the lungs over prolonged periods of time (hours to days) can be an adequate tool to prevent the VALI. While lung images from X-ray CT are available, dynamic changes in the lungs cannot be monitored and also the usage of X-ray exposure to patient for the long term can causes further complications. One promising technology to continuously monitor the ventilated patients is EIT, which has recently seen a significant and growing clinical interest for its ability to provide real time images of regional lung ventilation. EIT applies an elastic band of surface electrodes fastened around the thorax of patient to continuously measure the physiological parameters of the ventilation at the bedside. The volume of the EIT system is small, making it very portable. EIT is easily installed by a nurse or physician at the bedside and its electrode band is comfortably attached to the patient chest. The patient breathes through the ventilator while his breathing cycle, lung images, and physiological measures of ventilation are monitored on the screen in real time. The real time measurement of the physiological parameters of the ventilation by EIT helps avoid the VALI. The physician can be alarmed for further care in case of the prognosis of a possible complication, such as the VALI. The superiorities of the EIT based LPVS, against other imaging modalities such as CT, MRI, and PET, are the advantage of being non-invasive over long term usage (hours to days), minimally cumbersome (using electrodes and wires for the patient interface), very portable and light, and potentially, reasonably low-cost (using largely low-cost electronic components). The potential users of

the EIT based lung protective ventilation system are the children in pediatric intensive care unit and long-stay patients in hospitals.

The positive end expiratory pressure (PEEP) is a technique to continuously produce a positive airway pressure throughout the respiratory cycle (Bourke, 2003a; Shapiro et al., 1982). The PEEP maximizes the mean airway pressure to recruit the slow, collapsed/diseased alveoli in the ventilation by keeping them open during the whole trial (inspiration and expiration); however, it may cause more stress on the normal alveoli by frequent opening and closing them (Shapiro et al., 1982).

Chapter 5

Level Set based Reconstruction Algorithm for EIT Lung Images: First Clinical Results

5.1 Summary

This chapter is based on the paper – *Level Set based Reconstruction Algorithm for EIT Lung Images: First Clinical Results*, published in *Physiol. Meas.* by *Peyman Rahmati, Manuchehr Soleimani, Sven Pulletz, Inez Frerichs, and Andy Adler* (Rahmati et al., 2012b).

This chapter shows the first clinical results using the level set based reconstruction algorithm for electrical impedance tomography data. The level set based reconstruction method allows reconstruction of non-smooth interfaces between image regions, which are typically smoothed by traditional voxel based reconstruction methods. A time difference formulation of the level set based reconstruction method for 2D images is developed. The proposed reconstruction method is applied to reconstruct clinical EIT data of a slow flow inflation pressure-volume manoeuvre in lung healthy and adult lung injury patients. Images from the level set based reconstruction method (LSRM) and the voxel based reconstruction

method (VBRM) are compared. The results show comparable reconstructed images, but with an improved ability to reconstruct sharp conductivity changes in the distribution of lung ventilation using the level set based reconstruction method.

5.2 Introduction

Tomographic imaging systems seek to see the inside objects, by introducing energy and measuring its interaction with the medium. EIT measures the internal impedance distribution using surface measurements (Adler and Guardo, 1996; Adler et al., 1997). Electrical current is applied to the medium and the voltage at the surface is measured using electrodes. The impedance distribution is then estimated based on the measured voltages and medium geometry (Adler et al., 1994). Some of typical applications of these techniques are for geophysical imaging (Loke and Barker, 1996a,b; Church et al., 2006), process monitoring (Soleimani et al., 2006a; Manwaring et al., 2008), and functional imaging of the body (Frerichs, 2000; Frerichs et al., 2001; Gao et al., 2006; Adler et al., 2009; Frerichs et al., 2010; Rahmati et al., 2012b; Pulletz et al., 2011).

In this chapter, the focus is on image reconstruction in EIT using the level set (LS) approach. The LS approach has become popular because of its ability to track propagating interfaces (Osher and Sethian, 1998; Sethian, 2002; Rahmati et al., 2012a), and more recently it has been applied in variety of applications in inverse problems and in image processing (Santosa, 1996; Litman et al., 1998; Dorn et al., 2000; Osher and Paragios, 2003). The LSRM is a nonlinear inversion scheme using Gauss-Newton (GN) optimization approach to iteratively reduce a given cost functional, which is the norm of the difference between the simulated and measured data. In comparison to the VBRM (Polydorides et al., 2002), the LSRM has the advantage of introducing the conductivity of background and that of inclusions as known priori information into the reconstruction algorithm, enabling

it to reconstruct sharp contrasts (Soleimani et al., 2006d,a). The unknown parameters to be recovered from the data are the size, number, shapes of the inclusions. These unknown parameters are given as the zero LS of a higher dimensional function, called level set function (LSF). In every iteration, the LSF is modified according to an update formula to modify the shape of the inclusion at its zero LS (see figure 5.1 on page 72).

The LS method for shape based reconstruction is well studied in electrical and electromagnetic imaging for simulated and experimental tank data (Santosa, 1996; Litman et al., 1998; Dorn et al., 2000; Boverman et al., 2003; Chan and Tai, 2004; Soleimani et al., 2006c; Soleimani, 2007; Boverman et al., 2007; Banasiak and Soleimani, 2010); however, it has been never shown to be used for clinical data. This study, along with our previous work (Rahmati et al., 2012b) are the first implementations of the LSRM using time difference data for EIT clinical data. In this study, we use a difference formulation of the LSRM to reconstruct a 2D image of the distribution of lung ventilation over an inflation manouevre (figure 5.4 on page 78 and figure 5.5 on page 80).

The remainder of the chapter is organized as follows: In the next subsection, the formulation of the image reconstruction algorithm using difference and absolute solvers for EIT (subsection 5.3.1) is introduced. In subsection 5.3.2, the introduction to the LS technique employed for solving the inverse problem of EIT lung images is discussed. The applied human data and the setting of the EIT system are described in the introduction chapter (chapter 1). In section 5.5, the experimental results are shown for the LSRM and the VBRM; and the performance of the difference mode LSRM for monitoring human lungs data is qualitatively and quantitatively compared with that of the VBRM.

5.3 Methods

5.3.1 Difference and absolute reconstruction methods

As discussed in the previous chapter, there are two primary reconstruction types in EIT: “absolute (static) imaging" which attempts to recover an estimate of the absolute conductivity of the medium from the achieved data frame, and “difference imaging" which attempts to recover an estimate of the change in conductivity between two times based on the change between two data frames, v_2 and v_1. Difference EIT can compensate for measurement errors which do not change between data frames. Difference EIT is based on a difference data vector, $[y]_i = [v_2]_i - [v_1]_i$, where i is the number of the measurements,or, to increase sensitivity to small measurements, the normalized difference data $[y]_i = ([v_2]_i - [v_1]_i)/[v_1]_i$. Using a finite element model (FEM), the medium is discretized into N elements with conductivity σ. The conductivity change vector $x = \sigma_2 - \sigma_1$ is the change between the present conductivity distribution, σ_2, and that at the reference measurement, σ_1. The linearized difference forward solution for small changes in conductivities over time is given by (Adler et al., 1996; Adler and Lionheart, 2006; Adler et al., 2007):

$$d = Jm + n, \tag{5.1}$$

where J is Jacobian or sensitivity matrix around the reference conductivity distribution, defined by $\frac{\partial d}{\partial m}|_{\sigma_1}$ and n is the measurement noise, typically assumed to be an uncorrelated white Gaussian noise. In EIT, we need to solve an inverse problem to find an estimate of the conductivity, refered to as $\hat{m}$. The most common approach to find $\hat{m}$ is the use of the Gauss-Newton (GN) algorithm for EIT reconstruction (Cheney et al., 1990). The GN method solves the EIT inverse problem by minimizing the the following quadratic residue

(Adler et al., 2007):

$$\|d - J\hat{m}\|^2_{\sum_n^{-1}} + \|\hat{m} - m_0\|^2_{\sum_m^{-1}}, \tag{5.2}$$

where $\sum_n^{-1}$ and $\sum_{\hat{m}^{-1}}$ are the covariance matrix of measurement noise and that of conductivity vector ($\hat{m}$), respectively; and m_0 represent the expected value of element conductivity changes. By solving (5.2) for $\hat{m}$, the linearized EIT inverse solution is obtained as (see Appendix A):

$$\hat{x} = (J^T J + R)^{-1}(J^T d + R m_0), \tag{5.3}$$

where R is the regularization matrix and m_0 is the initial guess of the solution, which can be assigned to zero. In the remainder of this chapter, the GN approach is considered the reference technique. GN image reconstruction typically results in smoothed images with blurred edges, since the regularization matrix is based on a penalty filter for non-smooth images.

5.3.2 Level set method

One effective method to allow the reconstruction of sharp images is the LS method (Dorn et al., 2000). The classic formulation of this method assumes that the reconstructed image can take only two conductivity values: one for background with value σ_b and another one for inclusions with value σ_i. The regions which form the background and the inclusions are defined by the LSF, Ψ: a signed distance function to identify the unknown interface between the two conductivities. The value of the LSF is zero on the interface, negative inside the interface, and positive outside.

Compared to the more typical VBRMs, the LSRMs allow more accurate reconstruction of the boundary shape of step changes of conductivity (high contrast objects). This is because most regularization schemes for the traditional methods, which are necessary for

stabilizing the inversion, have the side-effect of artificially smoothing the reconstructed images. Therefore, these schemes are not well-suited for reconstructing high contrast objects with sharp boundaries.

In order to arrive at a robust and efficient shape-based inversion method, there is a requirement to computationally model the moving shapes. The LS technique is capable of modeling the topological changes of the boundaries (Osher and Sethian, 1998; Sethian, 2002). Figure 5.1 on page 72 shows a two phases image reconstructed using the LSRM. The LSF Ψ has separated the zero LS surface into two regions: foreground (inclusions) and background. The mapping function Φ projects the LSF to a 2D mesh to be applied for inverse solution calculation using FEM. Figure 5.1 on page 72, right panel, shows the conductivity of the inclusions in black where the LSF is negative and that of background in white where the LSF is positive. To begin with, we need to define an initial LSF, which may be a circle on level zero; and then deform this inital LSF using a predefined energy functional iteratively. Figure 5.2 on page 75 represents the steps as k represents the iteration number. After defining the initial LSF, the mapping function Φ projects the LSF to a 2D mesh to be fed to difference solver block to calculate the system senitivity matrix, Jacobian (J_k), as well as differential potential vectors, $\Delta d_i = [d_{real}]_i - [d(simulated)]_i$. The next step is to update the energy functional via a Gauss-Newton formula, ΔLSF_k. The initial LSF is then deformed by ΔLSF_k generating a new LSF. This new LSF is fed again to difference solver block for another iteration if the current iteration number (k) is not bigger than a maximum iteration number (K). In the following, the mathematical presentation of the LSRM is discussed.

In the LSRM, the shapes which define the boundaries, are represented by the zero LS of a LSF Ψ. If D is the inclusion with conductivity σ_i embedded in a background with conductivity σ_b, the boundary of the inclusion, which is also an interface between two

materials, is given by the zero LS (Soleimani et al., 2006c):

$$\partial D := \{r : \Psi(r) = 0\}, \tag{5.4}$$

where the image parameter at each point r is (Soleimani et al., 2006c)

$$\sigma(r) = \begin{cases} \sigma_i & \text{for } r : \Psi(r) < 0 \\ \\ \sigma_b & \text{for } r : \Psi(r) > 0 \end{cases}, \tag{5.5}$$

If this LSF is changed, for example by adding an update, the shapes are moved accordingly. This update to a given LSF causes the shapes being deformed in a way which reduces an error residue (cost functional).

The LSRM combines the general idea of GN optimization approach with a shape-based inversion approach. To derive the LSRM, the mapping (Φ) is defined which assigns a given LSF Ψ_D to the corresponding parameter distribution by $\sigma = \Phi(\Psi_D)$. The parameter distribution σ has the same meaning as in the traditional GN inversion scheme. The only difference is that in the shape-based situation it is considered as having only two values, namely an “inside" value and an “outside" value. In shape-based reconstruction approach, the LSF Ψ_D which divides the image into two separate areas as foreground (inclusion) and background is looked for.

Having defined this mapping Φ, one can replace the iterated parameter σ_k, with the following definition: $\sigma_k = \Phi(\Psi_D) = \Phi(\Psi_k)$. Instead of the forward mapping $F(\sigma)$, where function F maps the electrical conductivity distribution to the measured data, the new GN type approach needs to be considered in the combined mapping (Soleimani et al., 2006c):

$$d(\Psi) = G(\Phi(\Psi)), \tag{5.6}$$

where d is data point matrix, G is system matrix, and $\Phi(\Psi)$ stands for conductivity, see figure 5.1.

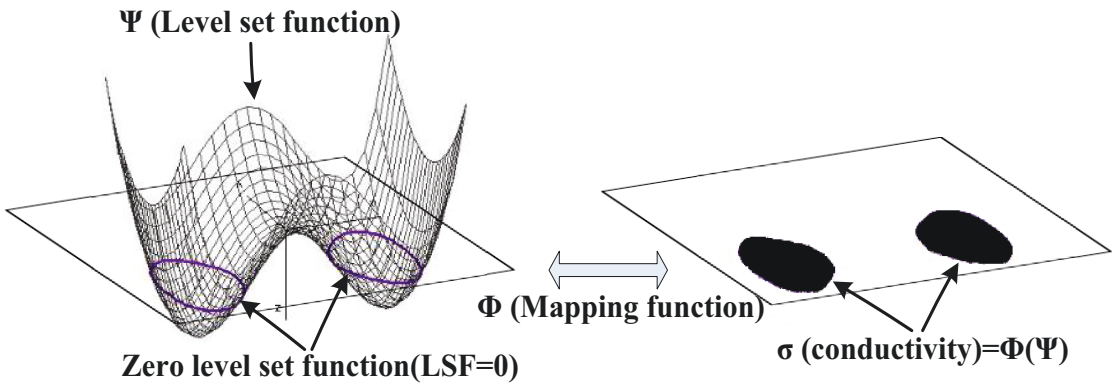

Figure 5.1: Level set function mapping to a 2D plane. From left to right columns, The 3D representation of an arbitrary level set function and its zero level set function crossing zero level set surface, and 2D mapping of the level set function on the zero lever set surface.

According to the chain rule, the LS sensitivity matrix (J_{LS}) can be written as below:

$$\begin{aligned} J_{LS} = \frac{\partial d}{\partial \Psi} &= (\tfrac{\partial G}{\partial \Phi(\Psi)})(\tfrac{\partial \Phi(\Psi)}{\partial \Psi}) \\ &= (J_{GN})(M), \end{aligned} \tag{5.7}$$

where $\frac{\partial G}{\partial \Phi(\Psi)}$ stands for the traditional GN sensitivity matrix (J_{GN}), and $\frac{\partial \Phi(\Psi)}{\partial \Psi} = M$. The mapping function Φ can be defined as a step function. Therefore, its first derivative matrix M is an impulse function, which is hard to be directly implemented. The implementation of the matrix M can be accomplished through applying the idea of a narrow band level set function. In a narrow band level set function, the sensitivity matrix J_{LS} is calculated for a narrow band with a predefined width around the evolved boundary. The level set function is defined over the whole image plane. However, the sensitivity matrix J_{LS} is calculated only for a narrow band in order to implement the matrix M. The width of the narrow band can be defined based on the length of the element edge in the applied FEM. In our

implementation, a coarse FEM was applied and the narrow band contained one element on the inner side and outer side of the evolved boundary. In the case of a coarse FEM, the increase in the width of the narrow band did not affect the quality of the reconstructed image.

The new GN update (Soleimani *et al*, 2006b) is as follows (see Appendix A) :

$$\begin{aligned}\Psi_{k+1} = \Psi_k + \lambda \left[(J^T_{(LS,k)} J_{(LS,k)} + \alpha^2 L^T L)^{-1} (J^T_{(LS,k)} (d_{real} - d(\Psi_k)))\right] \\ - \left[\alpha^2 L^T L(\Psi_k - \Psi_{int})\right] = \Psi_k + GN_{update} \\ = LSF(k) + \Delta LSF, \end{aligned} \tag{5.8}$$

where Ψ_{int} in the update term corresponds to the initial estimate of the LSF. There are two parameters λ and α to be tuned in this LS formulation. Figure 5.2 on page 75 illustrates the algorithm to calculate the above update formula. The optimal choice of the two parameters, λ and α, depends on the mesh density, the conductivity contrast and the initial guess (Soleimani et al., 2006a). The length parameter λ and the α both affect the magnitude of the LSF displacement; however, λ makes the main effect on the displacement, changing the shape of inclusion, in a given update. The higher the value of λ, the higher the LSF displacement will be.

Depending on the complexity of the internal inclusion, the evolution of the level set function can be trapped into one or multiple local minima. The displacement parameter (λ) can be adjusted using a genetic algorithm, which is less prone to local minima (Augusto et al., 2009). Genetic algorithm is a computational search technique which can be applied to estimate solutions to optimization problems (Augusto et al., 2009). Each unknown parameter value (genes) of the initial solution (initial level set function) is generated randomly. As the evolutionary process of the level set progresses, the most optimum solution is selected using the genetic algorithm. In the next iteration of the level set function, a

new optimum solution (generations) is generated from the previous optimum solution (reproduction) (Augusto et al., 2009). Also, shape derivatives and topological derivatives can be formulated with level set methods in order to prevent the shape optimization algorithm to get stuck in multiple local minima (He et al., 2007). The shape derivative measures the sensitivity of boundary perturbations and the topological derivative measures the sensitivity of the level set functional to creating a small ball with the center of x and the radius of r in the interior domain (He et al., 2007). The combination of the shape derivatives and topological derivatives in the definition of the energy functional of a level set based image reconstruction method can lead to a shape reconstruction algorithm with more flexibility to topological changes and less sensitivity to local minima. In the implementation of the proposed LSRM, a big value of the displacement parameter prevents the LSRM to stick on the local minima. Also, the narrow band has been selected to be wide enough in order to prevent the algorithm to be prone to the local minima.

The effect of the regularization parameter α depends on the choice of the regularization operator L. An identity matrix for L increases the stability of the inversion by reduced smoothing of the LSF. However, a first order difference operator for L will smooth the LSF (Soleimani et al., 2006a). As α increases, the final LSF tends to become smoother. A large value for α prevents the reconstruction algorithm from being able to separate close objects (low distinguishibility). In the experiments, the choice of L as the identity operator was made to improve distinguishibility between separate inclusions. In this implementation, a value of zero has been considered for the initial guess of Ψ_{int} in the above shape-reconstruction form.

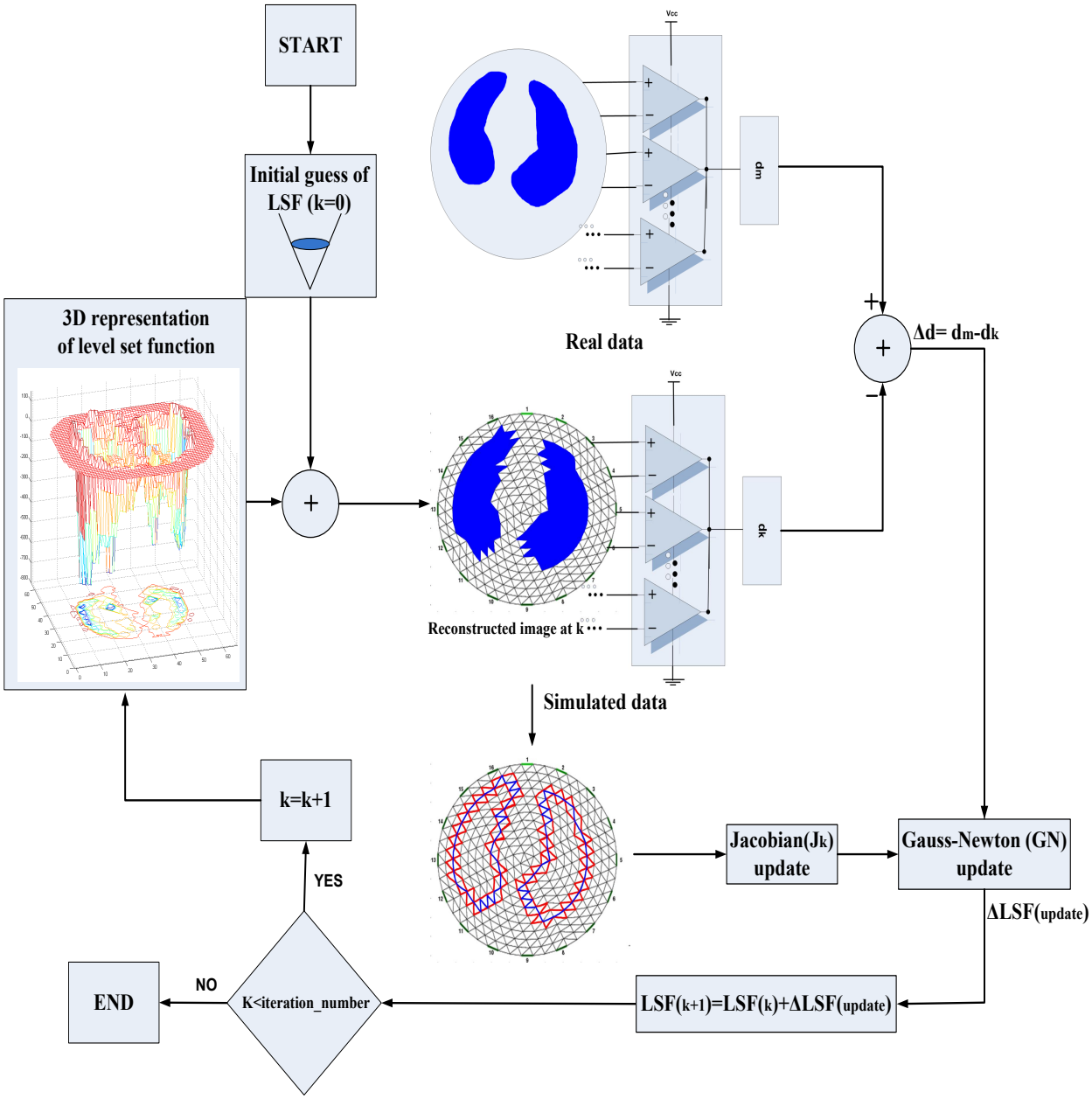

Figure 5.2: The level set based reconstruction algorithm using difference solver. The level set based reconstruction method comprises the following steps, respectively: level set function initial guess, inverse difference solver, Gauss-Newton update, level set function displacement by the given update, and iteration number increment.

5.4 Experimental data

In this thesis, the experimental data was obtained in the study described by Pulletz *et al*, (2011). Briefly, human breathing data was acquired from eight patients with healthy lungs

(age: 41 ± 12 years, height: 177 ± 8 cm, weight: 76 ± 8 kg, mean ± std.) and eighteen patients (age: 58 ± 14 years, height 177 ± 9 cm, weight: 80 ± 11 kg) with acute lung injury (ALI).

All patients were intubated and mechanically ventilated. The experimental procedure consisted of a low flow inflation pressure-volume manoeuvre applied by the respirator (Evita XL, Draeger, Luebeck, Germany), starting at an expiratory pressure of 0 cmH_2O and ending when either a) the gas volume reached 2 L, or b) the measured airway pressure reached 35 cmH_2O. Airway gas flow, pressure and volume were recorded at a sampling rate of 126 Hz. EIT data was acquired on sixteen self-adhesive electrodes (Blue Sensor L-00-S, Ambu, Ballerup, Denmark), placed at the 5th intercostal space in one transverse plane around the thorax, while a reference electrode was placed on the abdomen. EIT data was acquired at 25 frames per second, with an adjacent stimulation and measurement protocol, using current stimulation at 50 kHz and 5 mArms. Overall, 477 EIT data frames are acquired per inflation manoeuvre.

5.5 Experimental results

Images were reconstructed on a mesh roughly conforming to the anatomy of the subject, and the two different reconstruction algorithms (the VBRM and the LSRM) were tested on the clinical data (figure 5.3 on the following page - figure 5.6 on page 81). Figure 5.3 on the following page shows the reconstructed images of ventilation in a lung healthy patient measured based on the difference signal between start and end inflation. As inspired air increases, the resistivity of the lungs increases which has been shown as blue regions in the reconstructed images in figure 5.3 on the next page. The reconstructed images clarify the difference between LSRM and VBRM in terms of creating sharper reconstructions with larger contrasts at the interface between the inclusion and the background, presenting step

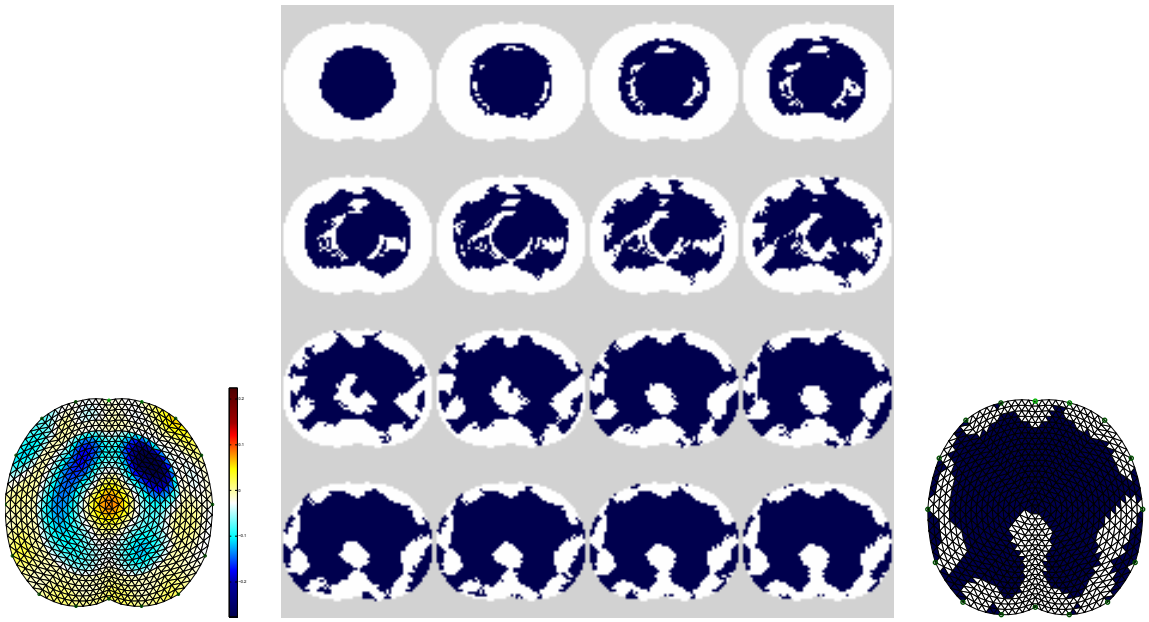

(a) (b) (c)

Figure 5.3: The qualitative comparison between the level set based reconstruction method and the voxel based reconstruction method in difference mode at the maximum airway pressure of the inflation manouevre for a patient with healthy lungs . (a) The lung reconstructed image using the voxel based reconstruction method. (b) The first sixteen iterations of the level set based reconstruction method for the same data as (a). (c) The final human lungs reconstructed image using the level set based reconstruction method at iteration 30.

change of conductivity. The final reconstructed image by the LSRM represents the air distribution inside the lungs after 30 iterations (figure 5.3(c)). The convergence happens quickly because the objects in the phantom are big and the initial level set function encloses the inclusions at iteration 0. A high value of the displacement parameter (λ) speeds up the convergence.

Figure 5.4 on the next page shows the LSRM reconstruction images for a patient with healthy lungs over the inflation manoeuvre measured for three different times from start of the inflation manoeuvre: 5.17s, 10.34s, and 17.24s. The measurement times are selected to show an initial airway pressure, a middle airway pressure, and a high airway pressure. The reconstruction algorithms for the LSRM and the VBRM used a finite element mesh (1600

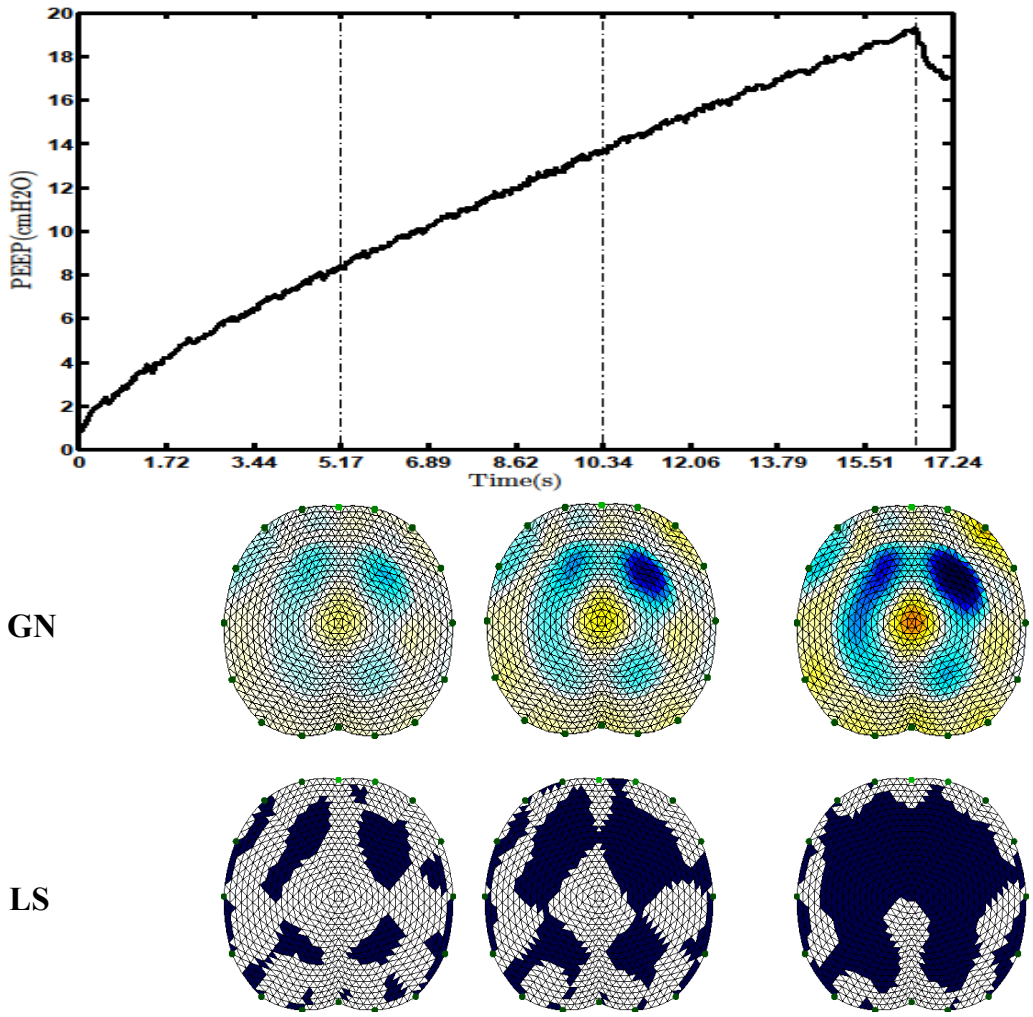

Figure 5.4: The clinical results of the level set based reconstruction method over the inflation manouevre of a patient with healthy lungs. The first row represents the inflation manoeuvre of the patient with healthy lungs, the second row is the results from the voxel based reconstruction method, and the third row is the clinical results of the level set based reconstruction method for the same patient. The reconstructed images are shown for three different measurement times: 5.17s (an initial airway pressure) , 10.34s (a middle airway pressure), and 17.24s (a high airway pressure).

elements). For all images of the VBRM for the patients (figure 5.3 on the preceding page - figure 5.5 on page 80), the colour axis (color map) was scaled to the same maximum value to maximize the displayed contrast. The LSRM results, when compared with the VBRM outcomes, show more details about the shape of the air distribution inside the lungs. The

shape of the air distribution of the VBRM images for different frames are very similar to each other (circular shapes). However, the LSRM images clearly show the difference in the shape of the air distribution for different time frames. In an incremental PEEP trial for a patient with ALI, the ventilation of the upper lung is different than that of the lower lung. This is because the mechanical properties of the lungs of patients with ALI are not uniform, with diseased and non-distensible alveoli that may be open and ventilated or collapsed and partially recruitable. In the case of a patient with ALI, the upper lung expands at the onset of the incremental PEEP trial and the lower part of the lung starts to contribute to the ventilation after the air pressure at the mouth reaches to a certain threshold. Therefore, the shape of the ventilation should not be the same at the upper and lower part of the lungs. The proposed LSRM shows different shape representation of the lungs ventilation for the upper and lower part of the lungs during the incremental PEEP trial, a trait absent in the traditional VBRM.

Figure 5.5 on the following page shows the LSRM reconstruction images for an ALI patient along the inflation manouevre measured for the same measurement times as figure 5.4 on the previous page. The density of the meshes are the same as in figure 5.4 on the preceding page (1600 elements). The VBRM offers less changes in the shape of the air distribution inside the lungs for the ALI patient, the second row of Figure 5.5 on the next page. However, the LSRM better show the changes of the air distribution for different frames, the third row of Figure 5.5 on the following page.

For the VBRM, a region of interest (ROI), describing the lungs, was identified as 25% of the maximum conductivity change (Pulletz *et al*, , 2011). For the LSRM, the ROI is the region with negative LSF, where there exists the inclusion. The VBRM and the LSRM were compared by calculating the normalized summation of elements conductivities (NSEC) over the ROI as follows:

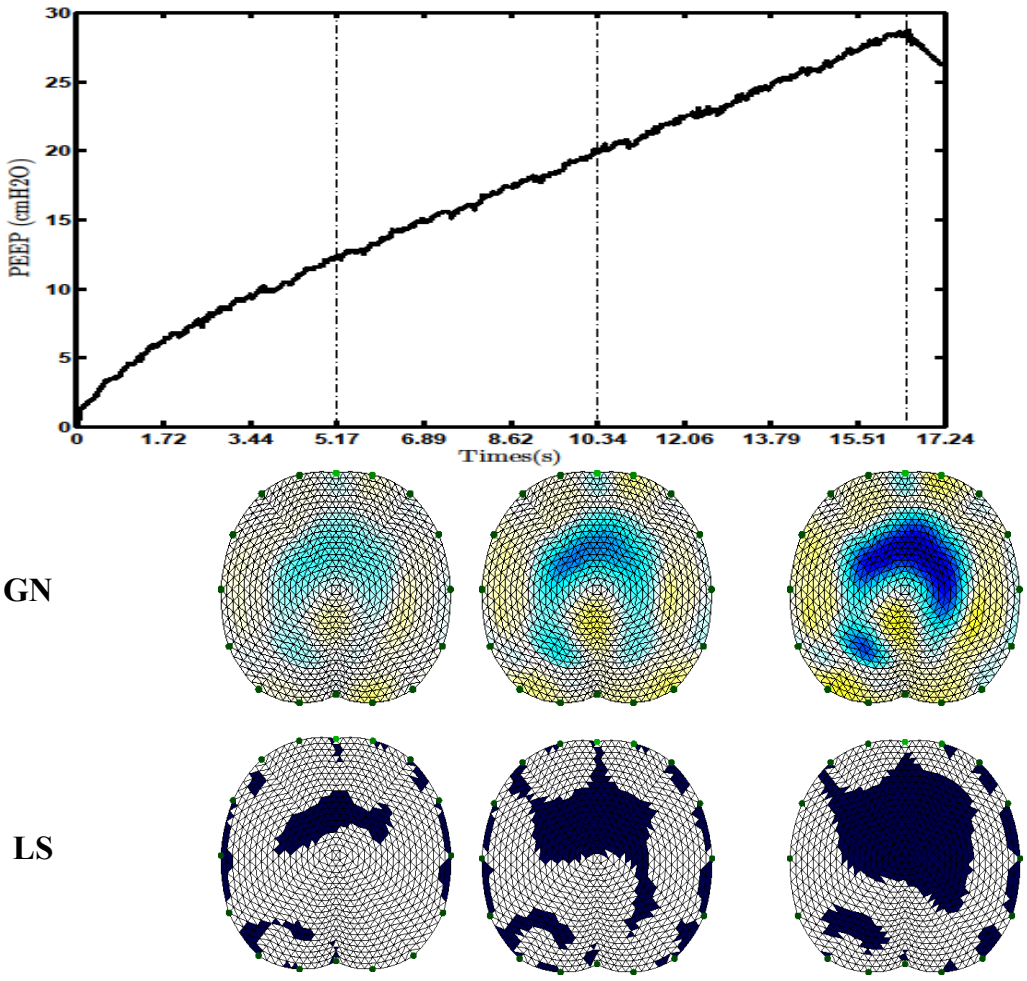

Figure 5.5: The clinical results of the level set based reconstruction method over the inflation manouevre of a patient with a heterogeneous lung disease. (a) The first row represents the inflation manouevre, the second row shows the voxel based reconstruction method results, and the third row is the clinical results of the level set based reconstruction method for the same patient. The reconstructed images are shown for three different measurement times: 5.17s (an initial airway pressure) , 10.34s (a middle airway pressure), and 17.24s (a high airway pressure).

$$NSEC(j) = \frac{\sum_{i=1}^{P} \sigma_{ij}}{\sum_{i=1}^{Q} \sigma_{ij_{max}}} \tag{5.9}$$

where j is the frame at which the NSEC is calculated, P is the number of the elements

inside the ROI for the frame j, j_{max} is the frame at which the maximum lung inflation happens (maximum lung volume), and Q is the number of the elements inside the ROI for the frame j_{max}. The NSEC was calculated at seven evenly spaced time points along the inflation manouevre. Results were presented for lung healthy (figure 5.6(a)) and ALI (figure 5.6(b)) patients. For both algorithms, the NSEC increases with pressure as the lung volume increases. The results show the NSEC curve is more non-linear for both algorithms for the ALI than lung healthy patients, which is consistent with the higher opening pressure of dependent lung regions in ALI patients.

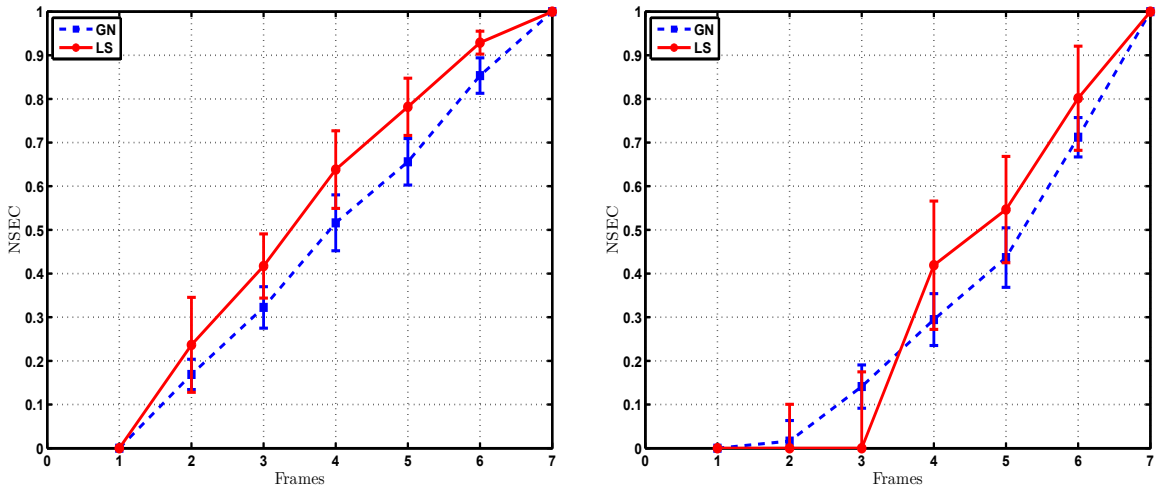

Figure 5.6: Normalized sum of element conductivities as a function of fraction of the inflation manouevre: (a) lung-healthy patients (b) Acute lung injury patients. In each case, the solid lines show example patients, while the distributions show the standard deviation over all patients in that class.

Chapter 6

A Generalized Inverse Problem with Weighted L1 and L2 Norms on Data and Regularization Terms

6.1 Summary

This chapter is based on the paper –*Weighted L1 and L2 Norms for Image Reconstruction: First Clinical Results of Electrical Impedance Tomography Lung Data*, *The 36th Annual Conference of the Canadian Medical and Biological Engineering Society*, by Peyman Rahmati, and Andy Adler, May 2013. An extended version of the published paper is presented in this chapter and is to be submitted to the Journal of Inverse Problems.

Many inverse problems can be formulated in terms of either quadratic objective functionals (Least Square fittings or L2 norms), the sum of absolute values (L1 norms), or a combination of both (L1 and L2 norms). The L1 and L2 norms can be independently applied over the data mismatch and the regularization terms (image term) of an inverse prob-

lem to constitute four classical inverse problems (L2L2, L1L2, L2L1, and L1L1 problems). The numerical solution and the implementation of the four classical inverse problems are most currently studied by Borsic and Adler (2012). The minimization of the L1 norm based penalty terms has been accomplished using primal-dual interior point method (PDIPM). This chapter formulates a generalized inverse problem solved using the PDIPM framework, hereinafter referred to as GPDIPM, to mix the smooth properties of the L2 norm based objective functionals with the blocky effect of the L1 norm based objective functionals on a element by element basis through a weighting strategy. The PDIPM is applied to numerically solve the proposed generalized inverse problem. In the implementation, EIT is used as an instance of an ill-posed, non-linear inverse problem. This chapter investigates the effectiveness of different combinations of weighted L2 and L1 norms in dealing with measurement uncertainties such as measurement noise and data outliers using both EIT simulated data and EIT human lung data. The simulated data is produced for a 2D circular mesh and EIT conductivity images are reconstructed for different weighting parameters for the L1 and L2 norms. The first clinical results of applying weighted L1 and L2 norms to reconstruct 2D lungs image from EIT lung data using a 2D thorax-shape mesh are shown.

6.2 Introduction

This chapter proposes a generalized inverse problem (GPDIPM) to independently mix the quadratic functionals (least square fittings or the L2 norms) and the absolute value based functionals (L1 norms) over the whole model space, which is the whole domain of the image plane in image reconstruction applications. The aim of this chapter is to mix the smooth properties of the L2 norm based regularization techniques with the blocky effect of the L1 norm based regularization methods on a element by element basis through a weighting strategy. The numerical solution of the proposed generalized inverse problem

through applying the PDIPM framework is shown. The selection of weighting parameters can be accomplished adaptively according to the prior information about the unknown parameters; however, the weighting strategy is beyond the scope of this chapter. In the following, the most common L2 norm based inverse problem applied for the linear and non-linear cases are introduced. Then, the advantages of using L1 norm based minimization problems along with the most commonly applied minimization techniques for the L1 norms are discussed.

This chapter proposes a generalized inverse problem which mixes the L1 norms and the L2 norms on both the data and the regularization terms of an inverse problem. The proposed generalized inverse problem contains a big range of possible inverse problems by introducing weighting parameters in its formulation. For instance, this chapter shows the inverse solutions of 16 different inverse problems in figure 6.1. The classical inverse problems such as L2L2, L1L2, L2L1, and L1L1 problems are a sub-domain of the proposed generalized inverse problem where the weighting factors are selected accordingly. The generalized solution of the proposed inverse problem is derived using the PDIPM framework. EIT is selected as an instance of ill-posed non-linear inverse problem. In the implementation, the EIT data is simulated for a 2D circular phantom. The EIT conductivity images are reconstructed by applying the proposed generalized inverse solution.

This chapter discusses the effectiveness of different combination of weighted norms (the L1 and L2 norms) under the following four different measurement conditions: 1) Without data outliers and synthetic added noise to EIT simulated data, 2) To account for the possible systematic and random errors occurring in EIT data acquisition process, a zero mean Gaussian noise was added to EIT simulated data to produce a signal to noise ratio (SNR) of 14 dB, 3) With strong data outliers, 4) With added zero mean Gaussian noise and data outliers.

The remaining of the chapter is organized as follows: In the next section, the proposed generalized inverse problem is formulated and its numerical solution using the PDIPM framework is derived. The applied experimental data are described in section 6.4. The experimental results are presented in section 6.5. Finally, the discussion is presented in section 6.6.

6.3 Generalized Inverse Problem with weighted L2 and L1 norms

This section formulates a general solution for a general inverse problem using the PDIPM framework. A general primal minimization problem can be written as set of error functions as follows:

$$(P) = \text{argmin} \left\{ \zeta \sum_{i=1}^{D_1} |f_{d_i}(m)| + \eta \sum_{j=1}^{D_2} |f_{p_j}(m)| + (1-\zeta) \|g_d(m)\|^2 + (1-\eta) \|g_p(m)\|^2 \right\}; \tag{6.1}$$

where ζ and η are weighting variables in the range $[0,\ 1]$. $f_d(m)$ is a L1 norm based data mismatch term, $f_p(m)$ is a L1 norm based regularization term, $g_d(m)$ is a L2 norm based data mismatch term, and $g_p(m)$ is a L2 norm based regularization term. A primal minimization problem can be formed through any combination of the error terms defined in (6.1). In the following, the general solution for the general primal problem in (6.1) is

derived using the PDIPM framework. One can consider the following objective functions:

$$
\begin{aligned}
f_d(m) &= W\ (h(m) - d), \\
f_p(m) &= \alpha\ L\ (m - m_0), \\
g_d(m) &= W\ (h(m) - d), \\
g_p(m) &= \alpha\ L(m - m_0),
\end{aligned}
\tag{6.2}
$$

where α is the regularization parameter, W is a weighting diagonal matrix, $h(m)$ is the forward measurement, d is the measured data, L is the regularization matrix, m is the model parameter distribution or the primal variables, m_0 is a reference model parameter distribution.

The smoothed PDIPM framework can be formulated as:

$$C_d(m) = f_{d_i}(m) - x_{d_i}\sqrt{f_{d_i}(m)^2 + \beta} = 0,\ \forall i \tag{6.3}$$

$$C_p(m) = f_{p_j}(m) - x_{p_j}\sqrt{f_{p_j}(m)^2 + \beta} = 0,\ \forall j \tag{6.4}$$

$$|x_{d_i}| \leq 1 \quad , \quad |x_{p_j}| \leq 1 \tag{6.5}$$

$$
\begin{aligned}
F_c(m) = {} & \zeta \frac{\partial}{\partial m}(f_d(m))x_d + \eta \frac{\partial}{\partial m}(f_p(m))x_p + \\
(1-\zeta) & \frac{\partial}{\partial m}(\|g_d(m)\|^2) + (1-\eta)\frac{\partial}{\partial m}(\|g_p(m)\|^2) = 0
\end{aligned}
\tag{6.6}
$$

The derived general PD framework above is solved iteratively using an iterative method, such as Newton method, and β decreases from points away from the region defined by the boundary $\|x_{d_i}\| \leq 1$ and $\|x_{p_j}\| \leq 1$ at every iteration.

The Newton system to be iteratively solved to calculate the updates for the primal

variables (m) and the dual variables (x_d and x_p) can be written as:

$$\begin{bmatrix} \frac{\partial}{\delta m}F_c(m) & \frac{\partial}{\delta x_d}F_c(m) & \frac{\partial}{\delta x_p}F_c(m) \\ \frac{\partial}{\delta m}C_d(m) & \frac{\partial}{\delta x_d}C_d(m) & \frac{\partial}{\delta x_p}C_d(m) \\ \frac{\partial}{\delta m}C_p(m) & \frac{\partial}{\delta x_d}C_p(m) & \frac{\partial}{\delta x_p}C_p(m) \end{bmatrix} \begin{bmatrix} \delta m \\ \delta x_d \\ \delta x_p \end{bmatrix} = - \begin{bmatrix} F_c(m) \\ f_d(m) - (\sqrt{f_d(m)^2 + \beta})x_d \\ f_p(m) - (\sqrt{f_p(m)^2 + \beta})x_p \end{bmatrix} \quad (6.7)$$

where $f = h(m) - d$, $F = diag(f)$, $X = diag(x)$, $\kappa = \sqrt{f^2 + \beta}$, $E = diag(\kappa).g = L(m - m_0)$, $G = diag(g)$, $Y = diag(y)$, $s = \sqrt{(L(m - m_0))^2 + \beta}$, $S = diag(s)$. Replacing the objective functions defined in (6.3) into (6.7), the following is obtained:

$$\begin{bmatrix} 2(1-\zeta)J^T W^T W J + 2(1-\eta)\alpha L^T L & \zeta J^T W & \eta\alpha L \\ (I - XE^{-}1F)J & -E & 0 \\ (I - YS^{-}1G)L & 0 & -S \end{bmatrix} \begin{bmatrix} \delta m \\ \delta x_d \\ \delta x_p \end{bmatrix} = - \begin{bmatrix} F_c(m) \\ f - Ex_d \\ g - Sx_p \end{bmatrix} \quad (6.8)$$

The primal variables (m) are updated in every iteration through a line search procedure which is written as $m^{(k+1)} = m^{(k)} + \lambda_m \delta m^{(k)}$, where k is the iteration number, δm is the update value with a descend direction to the optimal point, and λ is the step length (Nocedal and Wright, 1999). In a similar manner, the dual variables (x_d and x_p) are also updated in every iteration. However, the direction of updates in the dual variables can be changed for different value of β at every iteration and may not be always ascending. Therefore, a line search procedure is not an appropriate method to update the dual variables. The *scaling rule* is proposed to update the dual variables as follows (Andersen et al., 2000):

$$x^{(k+1)} = x^{(k)} + \min(1, \varphi^*)\, \delta x^{(k)} \quad (6.9)$$

where φ^* is a scalar value such that:

$$\varphi^* = \sup\left\{\varphi : \left|x_i^{(k)} + \varphi\ \delta x_i^{(k)}\right| \leq 1, \quad i = 1, \ldots, n\right\} \tag{6.10}$$

6.4 Experimental data

EIT is applied to reconstruct a conductivity distribution image of a 2D medium using the injection of electrical current into the medium and the collection of the resulting difference voltages across the electrodes attached to the boundary of the medium. EIT difference imaging was simulated using 16 electrodes with adjacent current stimulation pattern on one electrode plane discretized using a 2D circular finite element model (FEM) for the simulated data. A 2D human thorax-shape mesh was applied for the clinical data. The same clinical data described in chapter 5 is applied in this study.

6.4.1 Simulated data

Figure 6.1(a) shows the 2D phantom used to generate simulated data with 1024 mesh elements. The phantom contains two sharp inclusions with the two different conductivity values (0.9 S/m for the upper object and 1.1 S/m for the lower). The background conductivity value is 1 S/m. The inverse problem used the mesh density of 576 elements, which was different than the mesh density of the forward problem (1024 elements). The performance of the proposed generalized inverse problem, referred as to GPDIPM, for different weighting parameters was assessed based on two measurement conditions: 1) To account for the systematic errors and measurement noise of EIT data acquisition system, a zero mean Gaussian noise was added to EIT simulated data to produce a signal to noise ratio (SNR) of 14 dB, 2) To simulate the electrode error, caused due to electrode movement and electrode malfunction, a measurement failure rate of 0.5% was introduced, which means

one measurement out of 208 measurements needed for one EIT frame was missed.

6.5 Results

6.5.1 Simulated results

This study shows the EIT reconstructed images of the proposed GPDIPM framework with different selection of weighting parameters over both simulated and experimental data. The inverse solution is calculated using the proposed GPDIPM with $\beta = 1 \times 10^{-12}$. The stopping term to terminate the iterations depends on the value of the primal dual gap computed in every iteration of the PDIPM. According to the experiments, 10 iterations for the PDIPM were sufficient to reach to convergence. In the implementation, sixteen different selections for weighting parameters (ζ and η) are considered (figure 6.1(b), 6.3-6.6). The weighting matrix for ζ and η are selected as $[0, 0.3, 0.6, 1]$,including small, medium, and large weighting values. Figure 6.1 (b) presents the EIT reconstruction results for the 2D circular mesh using the proposed generalized PDIPM framework for sixteen different selection of weighting parameters. The lowest conductive region is shown in dark blue and the highest conductive region is colored in dark red. The colors between the dark blue and the dark red are assigned to the regions with conductivity values between the lowest to the highest values. In figure 6.1(b), the upper panel on the left corner shows the result of solving the traditional L2L2 problem where $[\zeta, \eta] = [0, 0]$. The lower panel on the left corner is the solution of the L1L2 problem where $[\zeta, \eta] = [1, 0]$. The upper panel on the right corner represents the solution of the L2L1 problem; and the lower panel on the right corner shows the conductivity distribution image for the L1L1 problem. For every selection of weighting parameters, the hyperparameter α was tuned up using the L-Curve method (Tarantola, 2005). Figure 6.2 shows the L-Curve plots for sixteen different

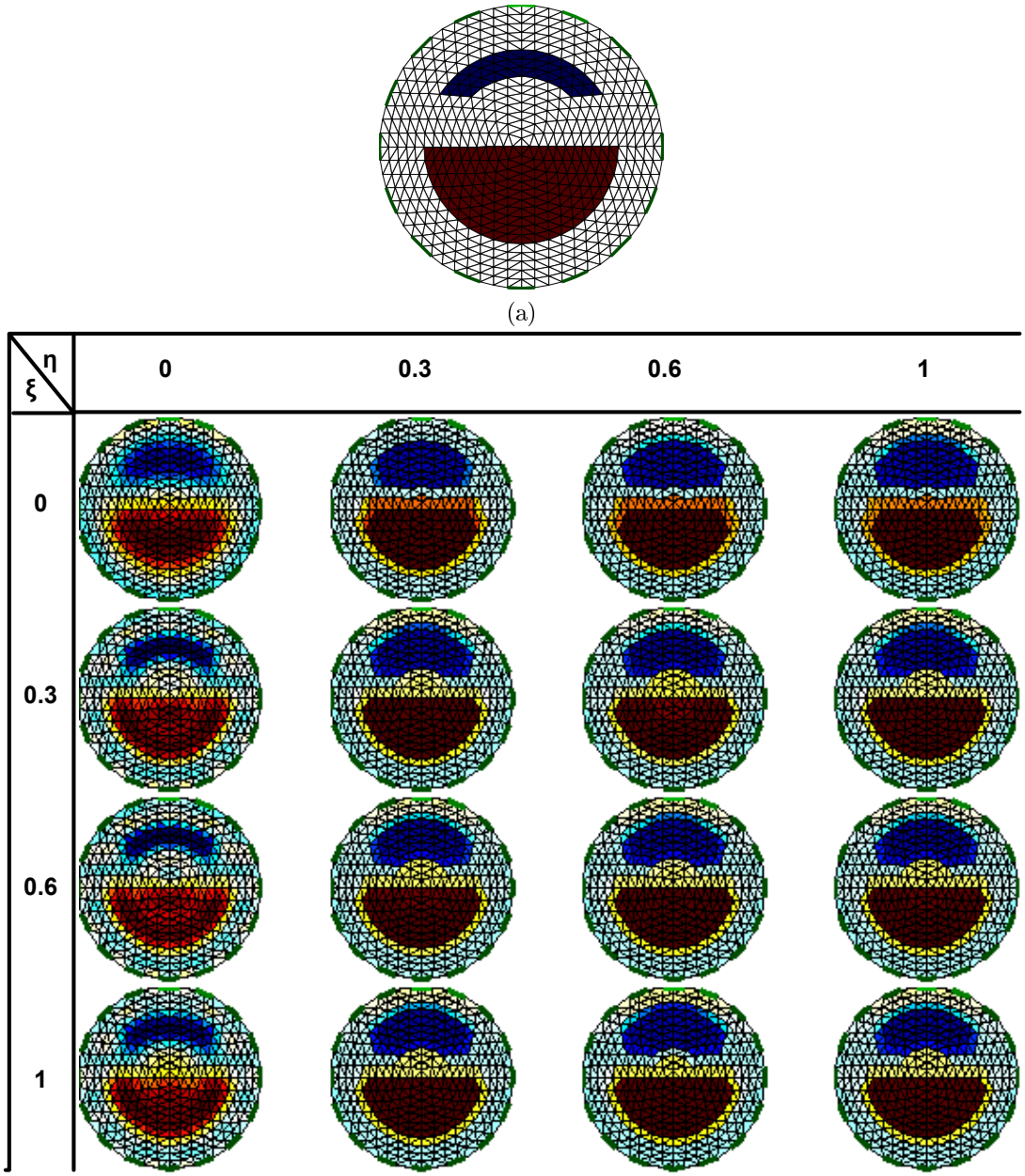

Figure 6.1: EIT Image reconstruction using the proposed GPDIPM with sixteen different weighting parameters for the L1 and L2 norms. (a) 2D circular mesh. (b) The reconstructed images with different weighting parameters ($[\zeta, \eta]$) using EIT simulated data achieved from the 2D mesh in figure6.1(a). From the dark blue to the dark red, the conductivity quantities increases.

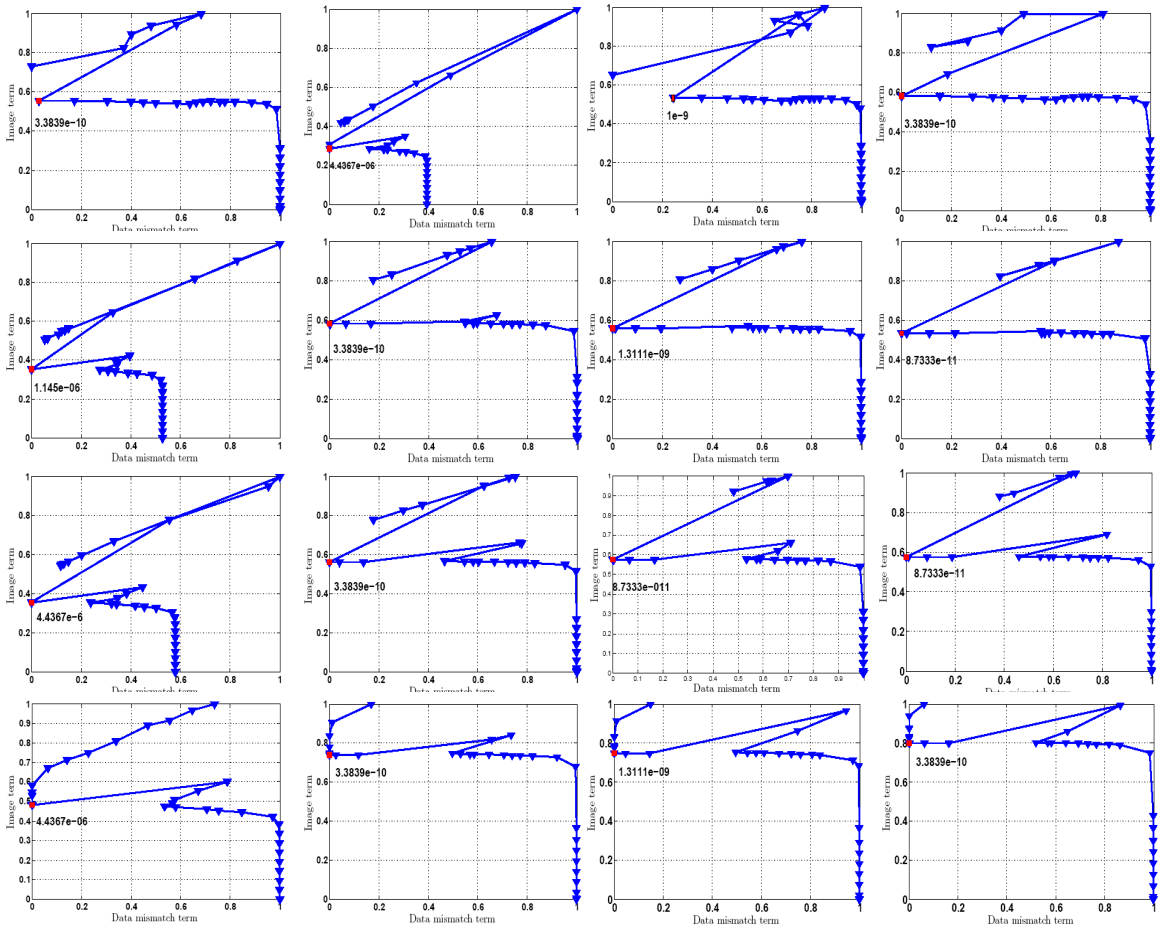

Figure 6.2: L-Curve method applied to tune up the regularization factor in the proposed GPDIPM for sixteen different selection of weighting parameters ($[\zeta, \eta]$).

selection of the weighting parameters in the proposed GPDIPM framework. A wide range of possible hyperparameters ($[10^{-13}, 10^{7}]$) is selected and linearly divided into 35 equally distanced bins. The data mismatch term and the image mismatch term are calculated and normalized for each hyperparameter (bin) within the range. The normalized L-curve is drawn and the optimum hyperparameter, corresponding to the optimal trade-off between the image and data residuals, is marked with a red square at the maximum curvature of the L-curves (figure 6.2). The horizontal axes shows the data mismatch term and the vertical axes represents the image mismatch term. The optimum hyperparameter

minimizes both the data and image mismatch terms simultaneously. The value of the optimum hyperparameter is written next to the red square on each panel in figure 6.2. Figure 6.3 shows the reconstruction results over EIT simulated data when perturbed by a

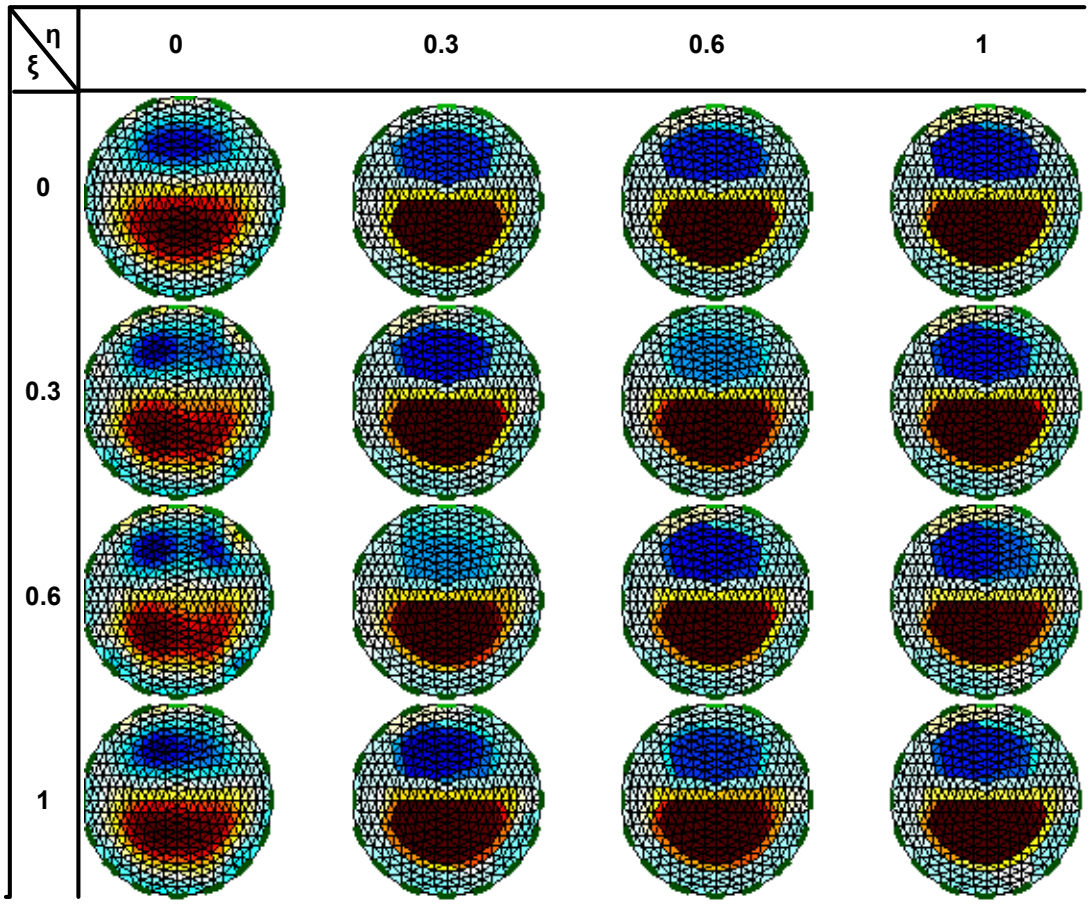

Figure 6.3: EIT Image reconstruction using the proposed GPDIPM with sixteen different weighting parameters ($[\zeta, \eta]$) over EIT simulated data perturbed by zero mean Gaussian noise (-14 dB). From the dark blue to the dark red, the conductivity quantities increases.

zero mean Gaussian noise (-14 dB). As can be seen in figure 6.3, the reconstruction quality drops in the presence of added noise (-14 dB). Adding a zero mean Gaussian noise to EIT simulated data, the reconstructed images with $\eta = 0$ (column 1 in figure 6.3) become blurry and the image quality drops. The reconstructed images with larger weighting parameters (columns 2-4 in figure 6.3) offer slightly higher robustness against the added noise and still

provide sharp edges, as weights of the L1 norms and their contributions in the solution become higher from one column to another. A more challenging measurement condition was tested by perturbing the EIT simulated data by noise (-14 dB) and data outliers, where one measurement out of 208 was missed. Figure 6.4 shows the reconstructed images

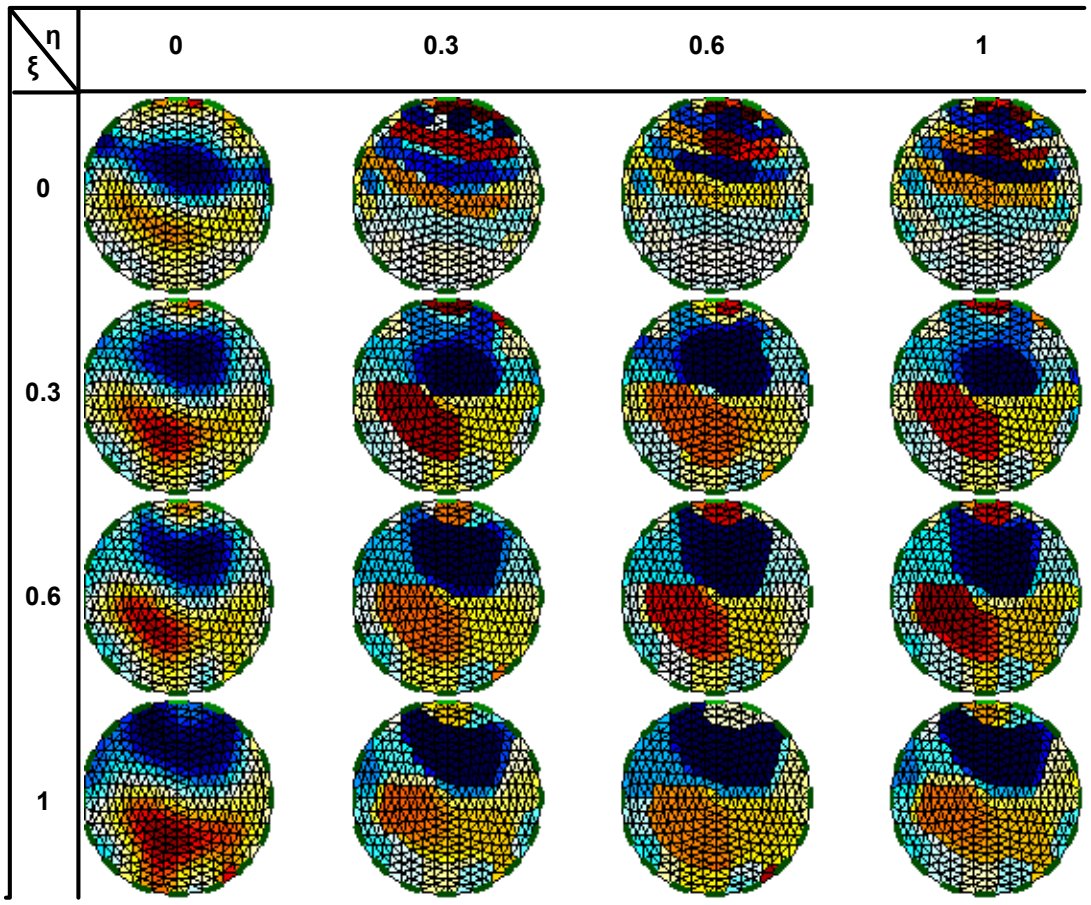

Figure 6.4: EIT Image reconstruction using the proposed GPDIPM with weighted L1 and L2 norms over EIT simulated data perturbed by zero mean Gaussian noise (-14 dB) and strong data outliers. From the dark blue to the dark red, the conductivity quantities increases.

for noise and data outliers test scenario. The weighting selection of either $\zeta = 0$ (row 1 in figure 6.4) or $\eta = 0$ (column 1 in figure 6.4) does not tolerate the imposed noise and outliers. However, the reconstructed images with weighting parameters larger than 0.3

offer higher robustness against noise and outliers.

6.5.2 Clinical results

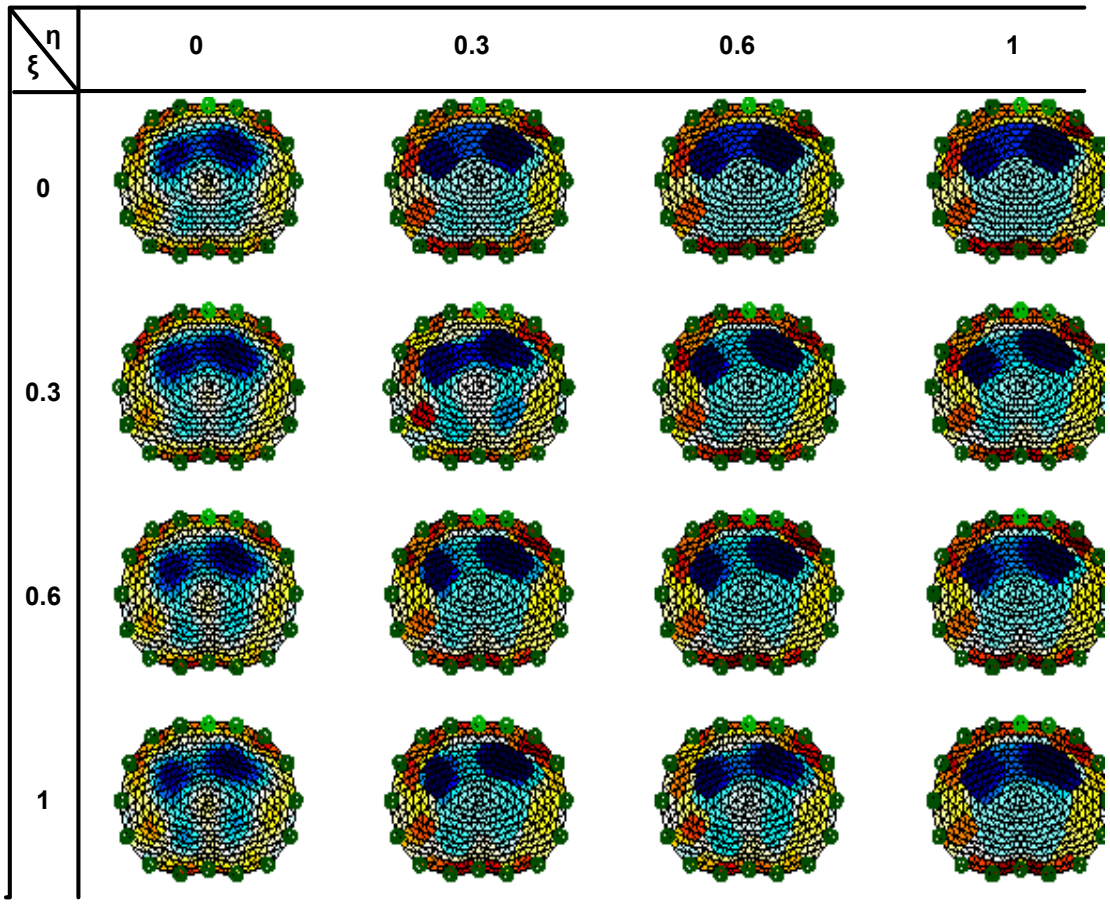

Figure 6.5: Clinical results of applying the proposed GPDIPM with weighted L1 and L2 norms over EIT lung data achieved from a patient with healthy lungs. From the dark blue to the dark red, the conductivity quantities increases.

This study also shows the first clinical results of applying weighted L1 and L2 norms over EIT lung data achieved for a patient with healthy lungs and a patient with acute lung injury (ALI). Positive end-expiratory pressure (PEEP) was applied on 7 patients with healthy lungs and 18 patients with ALI (Pulletz et al., 2011). EIT lung data was acquired

during the PEEP trial. Figure 6.5 represents difference EIT with the proposed GPDIPM framework when applied to EIT lung data frame taken at the maximum airway pressure (35 $cmH2O$) of the PEEP trial for a patient with healthy lungs (patient numbered 7 in our data base). The reconstructed images in figure 6.5 correctly show that the dependent lung areas are evenly filled with air for both the right and left lungs, which is expected at the highest pressure of PEEP trial. The L2 norm based solution, located at the upper panel on the left corner in figure 6.5, is in fact the traditional Gauss-Newton method, where $[\zeta, \eta] = [0, 0]$. The L2 norms smooth out the solution and therefore create blobby images. This also shows the high vulnerability of L2 norm based penalty terms to measurement errors as they overly penalize, by squaring the mismatch terms, both measurement errors and related conductivity changes due to the ventilation. In contrast, the L1 norm based penalty terms sum up the absolute values of mismatch terms and therefore are less prone to measurement errors and create sharp images with clear edges. The larger the weighting parameters, the higher the contribution of the L1 norms in the inverse solution will be. In figure 6.5, the reconstructed images with larger weighting values in columns 2-4 are sharper images due to the higher contribution of the L1 norms in the inverse solution. The higher weighting values for image mismatch terms offer sharper images (row 1 in figure 6.5); however, the images suffer from data outliers (artifacts at the thorax boundary), due to having L2 norms on the data mismatch terms ($\zeta = 0$). The higher weighting values for data mismatch terms (column 1 in figure 6.5) produce robustness against data outliers; however, the images are smoothed out, due to imposing L2 norms on the image mismatch terms ($\eta = 0$). Figure 6.6 demonstrates the effect of different weighting parameters (ζ and η) on the reconstructed image from EIT lung data achieved on the inflation limb of PEEP trial where the airway pressure reaches to its highest value for a patient with ALI (patient numbered 18 in the database). All reconstructed images clearly show the lungs

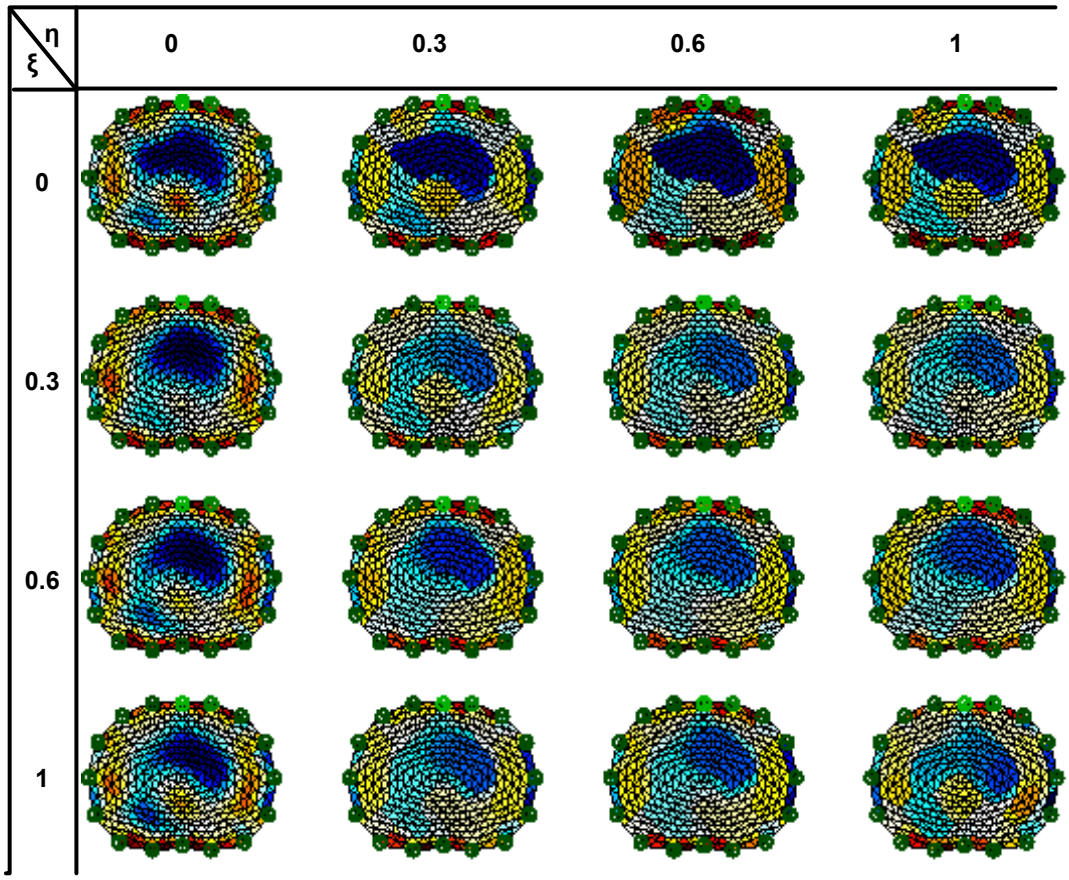

Figure 6.6: Clinical results of applying the proposed GPDIPM with weighted L1 and L2 norms over EIT lung data achieved from a patient with acute lung injury (ALI). From the dark blue to the dark red, the conductivity quantities increases.

malfunction due to a heterogeneous lung disease, which causes collapsed areas mostly in the lung dependent areas. Also, figure 6.6 indicates a decrease in the the lung volume, which is not normal at the plateau of the PEEP trial during the inflation phase.

6.6 Discussion

Positive end-expiratory pressure (PEEP) is applied in mechanically ventilated patients with ALI to help prevent lung damage and mortality. The best level of PEEP in mechanically

ventilated patients should be tuned regularly to prevent alveolar (air sac) strain. There are different preventive strategies to decrease the likelihood of different complications due to the application of mechanical ventilators in patients with ALI. One of the promising lung protective ventilation strategy (LPVS) is to apply a non-invasive imaging modality as a tool to help continuously monitor the ventilation distribution inside the lungs. While lung images from X-ray CT are available, dynamic changes in the lungs cannot be monitored, and X-ray exposure to patient for long term itself causes more complications. Functional EIT is a non-invasive, inexpensive imaging modality to image the regional ventilation distribution for long period of time. Difference EIT monitors lung impedance changes during ventilation and can be applied as a tool to help tune up the PEEP level. This study investigates the first clinical results of applying the GPDIPM with a combination of weighted L1 and L2 norms to produce quality EIT lung image.

In the clinical setting, there are several sources of errors in EIT data measurement, such as patient movement, sweating, and loose electrode connection, which create measurement errors. A reconstruction algorithm with sharp image and low vulnerability to potential uncertainties, such as measurement noise and data outliers is desirable in the clinical applications of EIT. The focus of chapter 8 is to assess and compare the robustness of four competing methods, including different combinations of the L1 and L2 norms on the data and image terms of their inverse problem, with the proposed EPIRMs in this thesis.

Different reconstruction methods can be derived from the proposed generalized inverse problem by selecting appropriate weighting parameters in (6.1). For instance, the GN, TV, and PDIPM are special cases of the proposed generalized inverse problem in ((6.1) where the weighting parameters ($[\zeta, \eta]$) are selected as [0, 0], [0, 1], and [1, 1], respectively. The LSRM, proposed in chapter 5, can also be derived from the proposed generalized inverse problem by introducing the corresponding LS parametrization in (6.1). The next chapter

discusses the mathematical procedure to derive the LSRMs from the proposed generalized inverse problem.

The proposed generalized inverse problem with weighted L1 and L2 norms can be utilized in EIT clinical applications to reconstruct sharp, quality images (figure 6.5, and 6.6). One of the main difficulties of EIT image reconstruction is the high dependency of its inverse solution to the hyperparameter selection. In this study, the L-curve method was implemented to tune the hyperparameter for every weighting combinations (figure 6.2). In the implementation, there was no compensation for the electrode movements and volume changes of the thorax due to breathing. It is expected that the reported results in this chapter become less noisy, especially at the proximity of the thorax boundary, if a motion compensation algorithm is applied.

Chapter 7

A Level Set based Primal Dual - Interior Point Framework for Using the L1-Norm or the L2-Norm on the Data and Regularization Terms of Inverse Problems

7.1 Summary

This chapter is based on the papers –"Level Set Technique for High Contrast Image Reconstruction", Peyman Rahmati, and Andy Adler, *The 36 Annual Conference of the Canadian Medical and Biological Engineering Society*, 2013; and " A Level Set based Regularization Framework for EIT Image Reconstruction", Peyman Rahmati, and Andy Adler, *XV Int. Conf. Electrical Bio-Impedance and XIV Electrical Impedance Tomography*, Heilbad Heiligenstadt, Germany, 2013. An extended version of these published papers is presented in this chapter and will be submitted to IEEE Transaction of Medical Imaging.

The level set technique is shown to generate promising results when applied to solve

a piece-wise constant inverse problem. The common LSRM uses one level set function and considers two different conductivity quantities for the background and the inclusion. The level set function evolves according to the Least Squares fitting (L2 norm) of the data and the regularization terms. The evolution of the level set function continues till the defined quadratic formulations become very small, providing us with the inverse problem solution. As a more solid alternative, we can consider L1 norm either on the data term, on the regularization term, or on the both. The L1 norm produces more robustness against noise and outliers. The PDIPM framework is shown to be successful in minimizing the L1 norms. In this chapter, a novel level set based PDIPM framework (LSPDIPM) for using the L1 norm indifferently on the data and the regularization term of an inverse problem is proposed. The implementation of the derived inverse problem solving framework is discussed and shown by applying the LSPDIPM to reconstruct 2D images from the measured data (forward solution) of an electrical impedance tomography system, which is a standard instance of an ill-posed inverse problem.

7.2 Introduction

Level set technique is shown to be a promising technique in the reconstruction of sharp transitions in piece-wise constant inverse problem, which is an inverse problem with unknown piece-wise parameters. In this chapter, a numerical framework to solve a piece-wise constant inverse problem using a Level Set based Primal Dual - Interior Point Method (LSPDIPM) is proposed. There are two main advantages to applying level set technique in the common PDIPM framework: The level set technique is shown to preserve the edges in high contrast medium, which results in high contrast reconstructed image with well defined interfaces between the background and the foreground; also the level set technique is capable of tracking the propagating interfaces, making it suitable for quickly changing

mediums in real-time applications. The L1 norm on the data term of an inverse problem is shown to provide robust estimations in the presence of data outliers. Also the L1 norm is proved to be an adequate choice to lead to sharp reconstructions when applied on the regularization term of an inverse problem with high level of noise.

As shown in chapters 5 and 6, the forward model indicates the relationship between the data measurements and the model parameters and is written as:

$$d = h(m) \tag{7.1}$$

where m is the vector of model parameters, a subset of the space of parameter values $\mathbb{R}^M$, d is the vector of data measurements, a subset of the space of the data values $\mathbb{R}^D$. It is common to assume that the data measurement and the model parameters follow up a Gaussian distribution (Tarantola, 2005). A primal problem, which is the maximum a posteriori (MAP) of the model parameters, can be written as (Borsic and Adler, 2012)

$$m_{MAP} = \text{argmin} \left\{ \sum_{i=1}^{D} |W_i(h(m)_i - d_i)|^{n_d} + \alpha \sum_{i=1}^{M} |L_i(m - m_0)|^{n_m} \right\} \tag{7.2}$$

where n_d is the order of the Gaussian distribution for the data term, n_m is the order of the Gaussian distribution for the parameter term, σ_{n_d} is the standard deviation for the data term, σ_{n_m} is the standard deviation for the parameter term, m_0 is a priori information of the model parameters, L is the Tikhonov regularization matrix, W is a diagonal matrix with the diagonal entries of $\frac{1}{(\sigma_{n_d})_i^{n_d}}$, and the scalar α is the Tikhonov hyperparameter (Tikhonov and Arsenin, 1977). Depending on the choice of n_m and n_d, four possible primal problems can be defined. L2L2 problem is when $n_m = n_d = 2$, which is the common least square optimization problem where Gauss-Newton method is used to solve for the unknown model parameters (Polydorides and Lionheart, 2002). L1L2 problem is when $n_d = 1$ and $n_m = 2$. L2L1 problem is when $n_d = 2$ and $n_m = 1$. L1L1 problem is when $n_d = 1$ and $n_m = 1$.

L2 norm on the model parameters assumes an inverse problem with smooth coefficients, while the L1 norm on the model parameters assumes a piece-wise constant inverse problem with big step changes. Borsic and Adler (2012) show that the use of L1 norms on the data and the regularization terms is helpful and increases the robustness of the inverse solution against data outliers and spatial noise, respectively. The selection of model orders, n_m and n_d, has to be accomplished independently according to our prior information about the model parameters, and the observations. In the case of having big step changes in the model parameters, the L1 norm on the model parameters and a TV regularization generate robust inverse solutions to spatial noise (Rudin et al., 1992; Chan and Mulet, 1996; Borsic, 2002; Borsic et al., 2010). The L1 norm on the data term generates robust estimates against data outliers (Tarantola, 2005). The L2 norm data and regularization terms are suitable choices for inverse problem with smooth coefficients. However in the context of inverse problem with high step changes in the medium (piece-wise constant inverse problem), the L1 norms on either data, the model parameters or the both are the optimal choices. The difficulty in dealing with the L1 norm optimization problems is where the argument of the absolute values in the MAP objective function is zero, making the term non-differentiable. There are two techniques to resolve the non-differentiability of the L1 norms: Bayesian (Kaipio et al., 2000), and deterministic approaches (Acar and Vogel, 1994; Chan et al., 1995; Vogel and Oman, 1996; Dobson and Vogel, 1997). The Bayesian approach minimizes the total variation regularization instead of minimization of the MAP objective function. Markov Chain - Montecarlo Method is used in the Bayesian approach to converge to the optimal solution. The main drawback of the Bayesian method is its high number of iterations. Instead, the deterministic approaches are easier to be computed (Chan et al., 1995; Borsic, 2002). The non-differentiability of the L1 norm is resolved through using a centering condition which is the replacement of $\|W(h(m) - d)\|^2$

by a quadratic norm as $\sqrt{(L_i(m-m_0))^2+\beta}$, with $\beta > 0$. The value of β depends on the application. The larger the β, the less the accuracy of the sought solution (Borsic and Adler, 2012). A very small value of β causes slow convergence (Chan et al., 1995; Borsic, 2002).

As an alternative approach, the PDIPM framework is shown promising results in the minimization of the sum of absolute values (L1 norms) in the context of non-smooth inverse problem (Chan et al., 1996; Andersen et al., 2000). The superiority of the PDIPM is studied and shown against the standard minimization methods with total variation regularization (Borsic, 2002). Borsic and Adler (2012) show the high performance of the PDIPM when applied to minimize a MAP function with independently selected norm orders (Borsic and Adler, 2012). Furthermore, the level set (LS) method has gained considerable attention in the last decade because of its effectiveness in tracking propagating interfaces in object tracking, image segmentation applications (Kass et al., 1998; Yezzi et al., 1997; Sethian, 2002; Rahmati et al., 2012a), and in the inverse problems (Santosa, 1996; Litman et al., 1998; Dorn et al., 2000; Soleimani et al., 2006a; Rahmati et al., 2012b). This chapter derives a general LS based PDIPM framework to solve the primal problem (7.2) with independently selected norm orders, for instance $[n_d, n_m] = [2, 2]$, $[n_d, n_m] = [1, 2]$, $[n_d, n_m] = [2, 1]$, or $[n_d, n_m] = [1, 1]$. The application of the LS technique to solve a piece-wise constant inverse problem using the combination of the L1 norms and L2 norms on the inverse problem terms has not been previously studied. This chapter proposes a LS based PDIPM framework, hereinafter called LSPDIPM, to compute the numerical solution for a L1 norms based inverse problem. The derived LSPDIPM offers two main advantages: The solution from the proposed LSPDIPM is robust against data outliers and spatial noise because of taking advantage of the L1 norms, which is minimized using the PDIPM framework, and the LS technique helps preserve the edges at the interfaces and reconstructs well defined

shapes as inclusion with high similarity to the actual inclusion (ground truth). Electrical Impedance Tomography (EIT) is applied as an instance of ill-posed inverse problem to show the implementation of the derived LSPDIPM.

The remainder of the chapter is organized as follows: In the next section, the three standard inverse problems (L1L2, L2L1, and L1L1 problems) are solved using the GPDIPM, proposed in the previous chapter (chapter 6). The proposed LSPDIPM framework is derived in section 7.4. Subsection 7.4.1 formulate the LSPDIPM for the case of the inverse problem with the L1 norm on data and the L2 norm on the regularization term (L1L2 problem). Subsection 7.4.2 derives the LSPDIPM for L2L1 problem; and the L1L1 problem is solved using the proposed LSPDIPM in subsection 7.4.3. In section 7.5, the EIT as our inverse problem case study is introduced. EIT reconstructed images for a L1L1 problem solved using the derived LSPDIPM are shown in section 7.6. The derived LSPDIPM offer promising performance in dealing with simulated data using a 2D circular phantom.

7.3 PDIPM for standard inverse problems

The general primal minimization problem defined in (6.1) in chapter 6 can be written in three ways: 1) L1L2 problem: which is when in (6.1) $[\zeta, \eta] = [1, 0]$, 2) L2L1 problem: which is when in (6.1) $[\zeta, \eta] = [0, 1]$, and 3) L1L1 problem: which is when in (6.1) $[\zeta, \eta] = [1, 1]$. In the following, the PD framework is derived for each primal problems (L1L2 problem, L2L1 problem, and L1L1 problem).

7.3.1 PD framework for the primal problem with L1 norm based data mismatch term and L2 norm based regularization term

The primal formulation for the L1L2 problem is as below:

$$(P) = \operatorname{argmin} \left\{ \sum_{i=1}^{D} |f_{d_i}(m) + \|g_p(m)\|^2 \right\} \tag{7.3}$$

the dual problem is

$$(D) = \min_{m} \left\{ \max_{x_d} \quad x_d^T f_d(m) + \|g_p(m)\|^2 \right\}, \quad \text{with} \quad |x_{d_i}| \leq 1 \tag{7.4}$$

interchanging the max and the min, the following is obtained:

$$(D) = \max_{x_d} \quad \min_{m} \left\{ x_d^T f_d(m) + \|g_p(m)\|^2 \right\}, \quad \text{with} \quad |x_{d_i}| \leq 1 \tag{7.5}$$

now the first order conditions can be applied on the primal variable:

$$\frac{\partial}{\partial m} \left\{ x_d^T f_d(m) + \|g_p(m)\|^2 \right\} \tag{7.6}$$

the dual problem is rewritten as follows:

$$\begin{aligned} (D) = \max_{x_d} \quad & \left\{ x_d^T f_d(m) + \|g_p(m)\|^2 \right\} \\ & |x_{d_i}| \leq 1 \\ & \frac{\partial}{\partial m} \left\{ x_d^T f_d(m) + \|g_p(m)\|^2 \right\} = 0 \end{aligned} \tag{7.7}$$

the Primal-Dual gap is written as

$$G_{PD} = \sum_{i=1}^{D} |f_{d_i}(m)| + \|g_p(m)\|^2 - \left[x_d^T f_d(m) + \|g_p(m)\|^2\right] = \sum_{i=1}^{D} \{|f_{d_i}(m)| - x_{d_i} f_{d_i}(m)\} \tag{7.8}$$

the smoothed Primal-Dual framework for L1L2 problem is formulated as below:

$$C_d(m) = f_{d_i}(m) - x_{d_i}\sqrt{f_{d_i}(m)^2 + \beta} = 0 \quad \forall i \tag{7.9}$$

$$|x_{d_i}| \leq 1 \tag{7.10}$$

$$F_c(m) = \frac{\partial}{\partial m}\left\{x_d^T f_d(m) + \|g_p(m)\|^2\right\} = 0 \tag{7.11}$$

the partial derivatives of (7.9) and (7.11) with respect to ∂m and ∂x are calculated and a set of equations can be derived to solve the L1L2 problem as follows:

$$\begin{bmatrix} \frac{\partial}{\partial m}F_c(m) & \frac{\partial}{\partial x_d}F_c(m) \\ \frac{\partial}{\partial m}C_d(m) & \frac{\partial}{\partial x_d}C_d(m) \end{bmatrix} \begin{bmatrix} \delta m \\ \delta x_d \end{bmatrix} = - \begin{bmatrix} F_c(m) \\ f_d(m) - (\sqrt{f_d(m)^2 + \beta})x_d \end{bmatrix} \tag{7.12}$$

the above equations are solved in an iterative manner when using a line search on the primal updates (δm), and a step length procedure on the dual updates (δx_d) .

7.3.2 PD framework for the primal problem with L2 norm based data mismatch term and L1 norm based regularization term

With the same procedure explained in subsection 7.3.1, the smoothed PD framework for the L2L1 problem can be derived as follows:

$$C_p(m) = f_{p_j}(m) - x_{p_j}\sqrt{f_{p_j}(m)^2 + \beta} = 0 \quad \forall j \tag{7.13}$$

$$|x_{p_j}| \leq 1 \tag{7.14}$$

$$F_c(m) = \frac{\partial}{\partial m}(\|g_d(m)\|^2) + \frac{\partial}{\partial m}(x_p^T f_p(m)) = 0 \tag{7.15}$$

The system formulation for the primal update (δm) and the dual update (δx_p) for the L2L1 problem can be written as:

$$\begin{bmatrix} \frac{\partial}{\partial m}F_c(m) & \frac{\partial}{\partial x_p}F_c(m) \\ \frac{\partial}{\partial m}C_p(m) & \frac{\partial}{\partial x_p}C_p(m) \end{bmatrix} \begin{bmatrix} \delta m \\ \delta x_p \end{bmatrix} = - \begin{bmatrix} F_c(m) \\ f_p(m) - (\sqrt{f_p(m)^2 + \beta})x_p \end{bmatrix} \tag{7.16}$$

7.3.3 PD framework for the primal problem with L1 norm based data mismatch term and L1 norm based regularization term

The following smoothed PD framework can be derived for the L1L1 problem:

$$C_d(m) = f_{d_i}(m) - x_{d_i}\sqrt{f_{d_i}(m)^2 + \beta} = 0, \ \forall i \tag{7.17}$$

$$C_p(m) = f_{p_j}(m) - x_{p_j}\sqrt{f_{p_j}(m)^2 + \beta} = 0, \ \forall j \tag{7.18}$$

$$|x_{d_i}| \leq 1, |x_{p_j}| \leq 1 \tag{7.19}$$

$$F_c(m) = \frac{\partial}{\partial m}(f_d(m))x_d + \frac{\partial}{\partial m}(f_p(m))x_p = 0 \tag{7.20}$$

The Newton system for the L1L1 problem using the same procedure explained for the GPDIPM in chapter 6 can be derived as below:

$$\begin{bmatrix} 0 & \frac{\partial}{\delta x_d}F_c(m) & \frac{\partial}{\delta x_p}F_c(m) \\ \frac{\partial}{\delta m}C_d(m) & \frac{\partial}{\delta x_d}C_d(m) & 0 \\ \frac{\partial}{\delta m}C_p(m) & 0 & \frac{\partial}{\delta x_p}C_p(m) \end{bmatrix} \begin{bmatrix} \delta m \\ \delta x_d \\ \delta x_p \end{bmatrix} = - \begin{bmatrix} F_c(m) \\ f_d(m) - (\sqrt{f_d(m)^2 + \beta})x_d \\ f_p(m) - (\sqrt{f_p(m)^2 + \beta})x_p \end{bmatrix} \tag{7.21}$$

As before, the line search procedure is applied to compute the updates for the primal variables (m); and the step length method is used to update the dual variables (x_d and x_p).

7.4 Level Set based Primal Dual - Interior Point Framework

In this section, a novel LS based PDIPM framework is proposed to identify the unknown or difficult to determine model parameters of a system defined as:

$$(P) = \text{argmin} \left\{ \sum_{i=1}^{D_1} |f_{d_i}(m)| + \sum_{j=1}^{D_2} |f_{p_j}(m)| + \|g_d(m)\|^2 + \|g_p(m)\|^2 \right\} \tag{7.22}$$

where $f_d(m)$ is a L1 norm based data mismatch term, $f_p(m)$ is a L1 norm based regularization term, $g_d(m)$ is a L2 norm based data mismatch term, and $g_p(m)$ is a L2 norm based regularization term. The proposed LS based PDIPM framework to solve the primal problem in (7.22) is referred to as LSPDIPM. In the following, the solution of the three standard inverse problems (L1L2 problem, L2L1 problem, and L1L1 problem) are derived using the proposed LSPDIPM.

7.4.1 LSPDIPM for the primal problem with L1 norm based data mismatch term and L2 norm based regularization term

The level set function (Ψ) is a signed distance function which is zero at the optimal solution and nonzero otherwise. The minimum distance from the optimal solution is achieved at zero level set function. An initial zero level set function can be assumed as a circle equation. The evolution of the level set function according to the minimization of a functional objective function (primal problem), which can be a standard least square error function, results in the optimal solution of an inverse problem. A mapping function (Φ) is used to project the 3D level set function into a 2D plane for the purpose of inverse solution calculation using finite element mesh (FEM). The level set evolution function is as follows:

$$\Psi_{k+1} = \Psi_k + \lambda(\Delta\Psi), \tag{7.23}$$

where Ψ_{k+1} is the updated level set function, Ψ_k is the current level set function, $\Delta\Psi$ is the update, Φ is the mapping function, $\Phi(\Psi_{k+1})$ is the updated model parameter distribution, which is the final inverse solution after the final iteration of the level set, $\Phi(\Psi_k)$ is the current model parameter distribution, λ is the regularization factor or hyperparameter which is a constant variable.

The primal formulation (P) is the error function defined as follows:

$$(P) = argmin_{\Phi(\Psi)} \left[\sum_i W_i |h_i(\Phi(\Psi)) - d_i| + \alpha \|L(\Phi(\Psi) - \Phi(\Psi^0))\|^2 \right] \tag{7.24}$$

where W is a weighting diagonal matrix, W_i is the i-th diagonal element, $h_i(\Phi(\Psi))$ is the i-th forward measurement, d_i is the i-th measured data, L is the regularization matrix, $\Phi(\Psi)$ is the model parameter distribution or the primal variables, $\Phi(\Psi^0)$ is a reference model parameter distribution In chapter 5, the LS Jacobian matrix (J_{LS}) was written as

below:

$$J_{LS} = \frac{\partial d}{\partial \Psi} = (\frac{\partial h}{\partial \Phi(\Psi)})(\frac{\partial \Phi(\Psi)}{\partial \Psi}) = (J_{GN})(M), \tag{7.25}$$

where $\frac{\partial h}{\partial \Phi(\Psi)}$ stands for the standard Gauss-Newton (GN) Jacobian matrix (J_{GN}), and $\frac{\partial \Phi(\Psi)}{\partial \Psi} = M$. Matrix M is a sparse matrix, meaning that the number of zero entries are much higher than that of non-zeros. The standard dense-matrix operations can be highly costly and memory consuming if applied on a large sparse matrix, such as matrix M. To prevent from high computational costs, either specialized sparse-matrix algorithms, designed to take advantage of the sparse structure of the matrix, need to be applied, or the sparse matrix must be converted to a dense matrix. The latter is the procedure used in the implementation of the proposed LSPDIPM. To make the algorithm efficient, the Jacobian matrix is calculated within a narrow band containing the data (non-zeros). The imaging domain Ω is discretized using the FEM and the imaging space is divided into many smaller regions, called elements. To construct the narrow band, the level set function, or the signed distance function, is defined to be negative inside its boundary and positive outside. The front (boundary) of the level set function is defined as:

$$\Omega_C(x, y) \; = \; \{ \; (x, y) \mid \Psi(x, y) \; = \; 0 \; \} \tag{7.26}$$

the narrow band width (ϵ) is denoted as:

$$\epsilon \; = \; a \; \cdot \; h \; ; \; a > 0 \tag{7.27}$$

where h is the length of the element edge in the applied mesh, and a is refine factor which is a small arbitrary number selected based on the density of applied mesh. A larger value

for the refine factor is suitable for a fine mesh and a smaller for a course mesh. The narrow band (NB) is written as:

$$\Omega_{NB}(x,y) \;=\; \{\,(x,y)\mid -\epsilon/2 \;<\; \Psi(x,y) \;<\; \epsilon/2\} \tag{7.28}$$

matrix M is non-zero within the narrow band and zero otherwise, which is the notion of Dirac delta function. In every iteration of the level set function (Ψ), the Jacobian matrix (J_{LS}) for the narrow band is computed, and therefore, the computed Jacobian only contains non-zero entries. The dimension of the matrix M is determined by the width of the narrow band (ϵ). The higher the width of the narrow band, the larger the number of elements considered for the Jacobian calculation and the bigger the size of the matrix M will be.

A dual variable x_i in the range $[-1,1]$, depending on the absolute value of $W_i(d - h(\Phi(\Psi)))$ is defined. This gives:

$$|W_i(h(\Phi(\Psi))_i - d_i)| = \max_{x_i:|x_i|\leq 1} x_i(W_i(h(\Phi(\Psi))_i - d_i)) \tag{7.29}$$

using the defined dual variable, and applying it to (P), the dual problem can be written as:

$$(D) = argmin_{\Phi(\Psi)}\left[max_x \quad x^T W(h(\Phi(\Psi)) - d) + \alpha\|L(\Phi(\Psi) - \Phi(\Psi^0))\|^2\right], with|x| \leq 1 \tag{7.30}$$

interchanging the max and the min, the following is achieved:

$$(D) = max_x \quad argmin_{\Phi(\Psi)}\left[x^T W(h(\Phi(\Psi)) - d) + \alpha\|L(\Phi(\Psi) - \Phi(\Psi^0))\|^2\right], with|x| \leq 1 \tag{7.31}$$

from (7.31):

$$\left[x^T W(h(\Phi(\Psi)) - d)\right] = D_1, \tag{7.32}$$

taking the first order derivative of D_1 with respect to the level set function results in:

$$\frac{\partial}{\partial \Psi}\left[D_1\right] = \frac{\partial}{\partial \Phi(\Psi)}\left[D_1\right]\frac{\partial}{\partial \Psi}\left[\Phi(\Psi)\right] = J_{GN}^T M^T W x = J_{LS}^T W x, \tag{7.33}$$

defining:

$$\frac{\partial}{\partial \Psi}\|L(\Phi(\Psi) - \Phi(\Psi^0))\|^2 = D_2, \tag{7.34}$$

taking the first order derivative of D_2 with respect to the level set function gives:

$$\frac{\partial}{\partial \Psi}\left[D_2\right] = 2L^T L(\Phi(\Psi) - \Phi(\Psi^0))M = 2M^T L^T L(\Phi(\Psi) - \Phi(\Psi^0)) \tag{7.35}$$

so the first order condition for the minimization in the dual problem is:

$$J_{LS}^T(\Phi(\Psi))Wx + 2\alpha M^T L^T L(\Phi(\Psi) - \Phi(\Psi^0)) = 0 \tag{7.36}$$

nulling the difference between the primal and dual problems gives us the following Primal-Dual gap:

$$\begin{aligned} G_{PD} = \sum_{i=1}^{D} |W_i(h(\Phi(\Psi))_i - d_i)| + \alpha\|L(\Phi(\Psi) - \Phi(\Psi^0))\|^2 - \\ x^T W(h(\Phi(\Psi)) - d) + \alpha\|L(\Phi(\Psi) - \Phi(\Psi^0))\|^2 = \\ \sum_{i=1}^{D} \{|W_i(h(\Phi(\Psi))_i - d_i)| - x_i W_i(h(\Phi(\Psi)) - d)\} \end{aligned} \tag{7.37}$$

the primal-dual G_{PD} is null if, for each i, either $W_i(h(\Phi(\Psi)) - d) = 0$ or $x_i = W_i(h(\Phi(\Psi)) -$

$d)/|W_i(h(\Phi(\Psi)) - d)|$. The *complementarity condition* that nulls the PD gap is therefore:

$$|W_i(h(\Phi(\Psi))_i - d_i)| - x_i W_i(h(\Phi(\Psi)) - d) = 0 \quad \forall i \tag{7.38}$$

the PD framework can be written as:

$$\begin{aligned} \sum_{i=1}^{M} |W_i(h(\Phi(\Psi)) - d_i)| - x^T W(h(\Phi(\Psi)) - d) = 0 \qquad (7.39) \\ |x_i| \leq 1 \\ J_{LS}^T(\Phi(\Psi))Wx + 2\alpha L^T L(\Phi(\Psi) - \Phi(\Psi)^{ast}) = 0 \end{aligned}$$

which constitutes the level set based PD method applied to the primal problem defined in (7.24). The smoothed version of LS based PD framework in (7.39) can be obtained through applying the *centering condition* which is the replacement of $|W_i(h(\Phi(\Psi)) - d_i)|$ by $\sqrt{(W_i(h(\Phi(\Psi)) - d_i)^2 + \beta}$, with $\beta > 0$. Therefore, the smoothed LS based PD framework is achieved as:

$$|x_i| \leq 1, \tag{7.40}$$

$$F_c(\Phi(\Psi)) = J_{LS}^T(\Phi(\Psi))Wx + 2\alpha M^T L^T L(\Phi(\Psi) - \Phi(\Psi^0)) = 0, \tag{7.41}$$

$$C_d(\Phi(\Psi)) = (h_i(\Phi(\Psi)) - d_i) - x_i\sqrt{(h_i(\Phi(\Psi)) - d_i)^2 + \beta} = 0, \quad \beta > 0, \quad i = 1, \ldots, \tag{7.42}$$

and the GN method is applied to solve for the primal variables (Ψ) and the dual variables (x). To find the optimal solution of the above newton system, the derivatives of (7.42) and (7.41) with respect to $\partial\Psi$ and ∂x is calculated and the first order conditions are imposed. From (7.41):

$$\frac{\partial}{\partial \Psi}\left[J_{LS}^T(\Phi(\Psi))Wx + 2\alpha M^T L^T L(\Phi(\Psi) - \Phi(\Psi^0))\right] =$$
$$\frac{\partial}{\partial \Phi(\Psi)}\left[J_{LS}^T(\Phi(\Psi))Wx\right]\frac{\partial}{\partial \Psi}\left[\Phi(\Psi)\right] +$$
$$\frac{\partial}{\partial \Phi(\Psi)}\left[2\alpha M^T L^T L(\Phi(\Psi) - \Phi(\Psi^0))\right]\frac{\partial}{\partial \Psi}\left[\Phi(\Psi)\right] = 2\alpha M^T L^T LM, \tag{7.43}$$

and,

$$\frac{\partial}{\partial x}\left[J_{LS}^T(\Phi(\Psi))Wx + 2\alpha M^T L^T L(\Phi(\Psi) - \Phi(\Psi^0))\right] = J_{LS}^T(\Phi(\Psi))W, \tag{7.44}$$

for (7.42):

$$\frac{\partial}{\partial \Psi}\left[(h_i(\Phi(\Psi)) - d_i) - x_i\sqrt{(h_i(\Phi(\Psi)) - d_i)^2 + \beta}\right] =$$
$$\frac{\partial}{\partial \Psi}\left[(h_i(\Phi(\Psi)) - d_i)\right] - x_i\frac{\partial}{\partial \Psi}\left[\sqrt{(h_i(\Phi(\Psi)) - d_i)^2 + \beta}\right] \tag{7.45}$$

and also:

$$\frac{\partial}{\partial \Psi}\left[(h_i(\Phi(\Psi)) - d_i)\right] = J_{LS}(\Phi(\Psi)), \tag{7.46}$$

$$\frac{\partial}{\partial \Psi}\left[\sqrt{(h_i(\Phi(\Psi)) - d_i)^2 + \beta}\right] = E^{-1}FJ_{LS}(\Phi(\Psi)), \tag{7.47}$$

where $f_i = h_i(\Phi(\Psi)) - d_i$, $F = diag(f_i)$, $X = diag(x_i)$, $\eta_i = \sqrt{f_i^2 + \beta}$, $E = diag(\eta_i)$. and thus:

$$\frac{\partial}{\partial \Psi}\left[(h_i(\Phi(\Psi)) - d_i) - x_i\sqrt{(h_i(\Phi(\Psi)) - d_i)^2 + \beta}\right] = \tag{7.48}$$
$$J_{LS}(\Phi(\Psi)) - XE^{-1}FJ_{LS}(\Phi(\Psi)) = (I - XE^{-1}F)J_{LS}(\Phi(\Psi))$$

where I is the identity matrix. The partial derivatives of (7.42) with respect to ∂x are:

$$\frac{\partial}{\partial x}\left[(h_i(\Phi(\Psi)) - d_i) - x_i\sqrt{(h_i(\Phi(\Psi)) - d_i)^2 + \beta}\right] = -E, \tag{7.49}$$

if it is assumed that the Jacobian ($J_{LS}(\Phi(\Psi))$) is constant and does not depend on the primal variables ($\Phi(\Psi)$)) at every iteration of the LS based PD framework, the Newton system for solving the primal problem using the derived LSPDIPM can be written as follows:

$$\begin{bmatrix} 2\alpha M^T L^T L M & J_{LS}^T W \\ (I - XE^{-1}F)J_{LS} & -E \end{bmatrix} \begin{bmatrix} \delta\Psi \\ \delta x \end{bmatrix} = - \begin{bmatrix} J_{LS}^T W x + 2\alpha M^T L^T L(\Phi(\Psi) - \Phi(\Psi^0)) \\ f - Ex \end{bmatrix} \tag{7.50}$$

The dependency of J_{LS} on Ψ is dropped in the derived LS based PD framework. The derived set of equations in (7.50) are iteratively solved for the primal variables ($\delta\Psi$) and the dual variables (δx) using an iterative method such as Newton method. The updates of the primal and dual variables can be separately written as follows:

$$\delta\Psi = -[J_{LS}^T W E^{-1}(I - XE^{-1}F)J_{LS} + 2\alpha M^T L^T L M]^{-1}\times \tag{7.51a}$$
$$[J_{LS}^T W E^{-1} f - 2\alpha M^T L^T L(\Phi(\Psi) - \Phi(\Psi^0))]$$
$$\delta x = E^{-1}(f - Ex) + E^{-1}(I - XE^{-1}F)J_{LS}\delta\Psi; \tag{7.51b}$$

a traditional line search procedure (Nocedal and Wright, 1999) can be applied to find an appropriate step length λ_Ψ resulting in the update $\Psi^{(k+1)} = \Psi^{(k)} + \lambda_\Psi \delta\Psi^{(k)}$, where k is the iteration number. A *scaling rule* is applied to compute the updates for the dual variables (x).

7.4.2 LSPDIPM for for the primal problem with L2 norm based data mismatch term and L1 norm based regularization term

In this subsection, the Newton system for the L2L1 problem using the derived LSPDIPM is derived. In a similar manner explained in subsection 7.4.1, the LS based PD framework for the L2L1 problem can be obtained as below:

$$C_p(\Phi(\Psi)) = L_j(\Phi(\Psi) - \Phi(\Psi^0)) - y_j\sqrt{(L_j(\Phi(\Psi) - \Phi(\Psi^0)^2 + \beta} = 0 \quad \forall j \tag{7.52}$$

$$|y_j| \leq 1 \tag{7.53}$$

$$F_c(\Phi(\Psi)) = 2\ J_{LS}^T(\Phi(\Psi))W^TW(h(\Phi(\Psi)) - d) + \alpha M^T L^T y = 0 \tag{7.54}$$

where y is the dual variable, and $g_j = L_j\Phi(\Psi)$, $G = diag(g_j)$, $Y = diag(y_j)$, $s_j = \sqrt{(L_j\Phi(\Psi))^2 + \beta}$, $S = diag(s_j)$. In a similar manner explained in subsection 7.4.1, the Newton system can be written as:

$$\begin{bmatrix} 2\ J_{LS}^T W^T W J_{LS} & \alpha M^T L^T \\ (I - YS^{-1}G)LM & -S \end{bmatrix} \begin{bmatrix} \delta\Psi \\ \delta y \end{bmatrix} = - \begin{bmatrix} 2\ J_{LS}^T W^T W(h(\Phi(\Psi)) - d) + \alpha M^T L^T y \\ g - Sy \end{bmatrix} \tag{7.55}$$

the primal and dual updates are:

$$\delta\Psi = -[2J_{LS}^T W^T W J_{LS} + \alpha M^T L^T S^{-1}(I - YS^{-1}G)LM]^{-1} \times \tag{7.56a}$$

$$[2J_{LS}^T W^T W(h(\Phi(\Psi)) - d) + \alpha M^T L^T S^{-1} g]$$

$$\delta y = S^{-1}(g - Sy) + S^{-1}(I - YS^{-1}G)LM\delta\Psi \tag{7.56b}$$

a line search is used on the primal updates ($\delta\Psi$), a step length procedure on the dual updates (y), and the above equations are iterated to convergence.

7.4.3 LSPDIPM for the primal problem with L1 norm based data mismatch term and L1 norm based regularization term

In this subsection, the Newton system for the L1L1 problem using the derived LSPDIPM is derived. In a similar manner explained in subsection 7.4.1, the smoothed LS based PD framework for the L1L1 problem can be obtained as below:

$$C_d(\Phi(\Psi)) = (h_i(\Phi(\Psi)) - d_i) - x_i\sqrt{(h_i(\Phi(\Psi)) - d_i)^2 + \beta} = 0,\ \forall i \tag{7.57}$$

$$C_p(\Phi(\Psi)) = L_j(\Phi(\Psi) - \Phi(\Psi)^*) - y_j\sqrt{(L_j(\Phi(\Psi) - \Phi(\Psi)^*))^2 + \beta} = 0,\ \forall j \tag{7.58}$$

$$|x_i| \leq 1, |y_j| \leq 1 \tag{7.59}$$

$$F_c(\Phi(\Psi) = J_{LS}^T(\Phi(\Psi))Wx + \alpha M^T L^T y = 0 \tag{7.60}$$

where y and x are the dual variables. The Newton system to be iteratively solved for the primal and dual variables is:

$$\begin{bmatrix} 0 & J_{LS}^T W & \alpha M^T L^T \\ (I - XE^{-1}F)J_{LS} & -E & 0 \\ (I - YS^{-1}G)LM & 0 & -S \end{bmatrix} \begin{bmatrix} \delta\Psi \\ \delta x \\ \delta y \end{bmatrix} = - \begin{bmatrix} J_{LS}^T Wx + \alpha M^T L^T y \\ f - Ex \\ g - Sy \end{bmatrix} \tag{7.61}$$

As for the previous cases, updates for the primal variables and for the two sets of the dual variables can be computed separately as follows:

$$\delta\Psi = -[J_{LS}^T W E^{-1}(I - XE^{-1}F)J_{LS} + \alpha M^T L^T S^{-1}(I - YS^{-1}G)LM]^{-1} \times \tag{7.62a}$$

$$[J_{LS}^T W E^{-1} f + \alpha M^T L^T S^{-1} g]$$

$$\delta x = E^{-1}(f - Ex) + E^{-1}(I - XE^{-1}F)\ J_{LS}\ \delta\Psi \tag{7.62b}$$

$$\delta y = S^{-1}(g - Sy) + S^{-1}(I - YS^{-1}G)\ LM\ \delta\Psi \tag{7.62c}$$

The traditional line search is utilized to update on the primal variables and a step length procedure is used to compute the updates of the two dual variables.

7.5 Simulated Data

In the simulation, the proposed LSPDIPM was applied to reconstruct images from the simulated data of EIT, as a highly ill-posed and challenging inverse problem. Difference EIT was simulated with 16 electrodes on a one electrode plane discretized using a circular FEM. Figure 1 shows the 2D phantom applied to generate simulated data with 1024 mesh elements. The phantom contains two sharp inclusions with the same conductivity located in the upper and the lower part of the mesh. The background conductivity value is 1 S/m and the inclusions have the conductivity of 0.9 S/m. The inverse problem used a mesh density of 576 elements, which was different to the mesh density of the forward problem (1024 elements).

7.6 Results

This chapter shows the EIT reconstructed images of the proposed LSPDIPM when applied to solve a primal problem with the L1 norms on both the data mismatch and the regularization terms (L1L1 problem). The reason for choosing the L1L1 formulation is because the L1 norms has been shown to offer the highest robustness to spatial noise and outliers (Borsic and Adler, 2012). The inverse solution is calculated using the proposed LSPDIPM with $\beta = 1 \times 10^{-12}$. The stopping term for terminating the iterations depends on the value of the primal dual gap computed in every iteration of the LSPDIPM. The single cycle of the proposed LSPDIPM approach requires almost the same computational cost than the GN approach or the PDIPM framework. The only difference is the number of iterations that

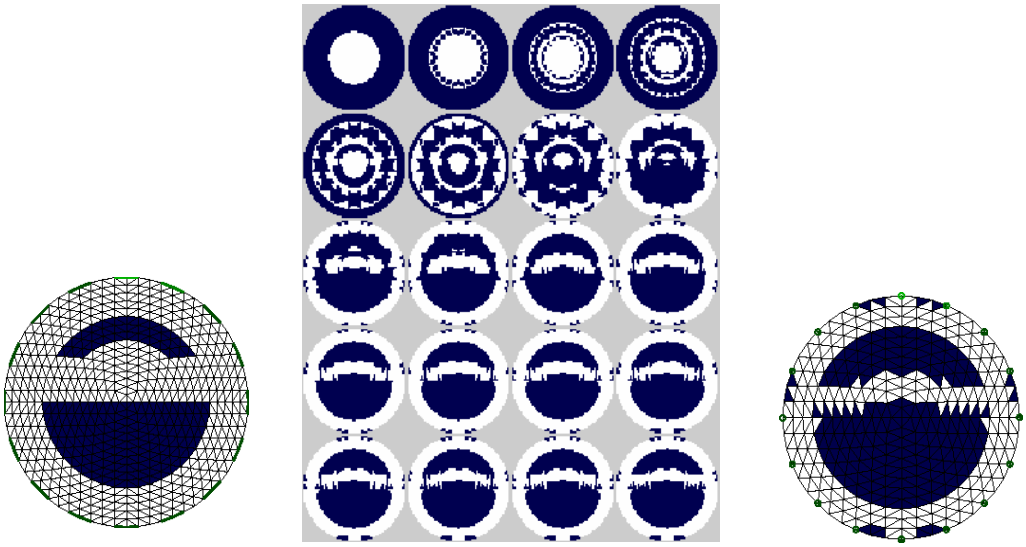

Figure 7.1: EIT Image reconstruction using the proposed LSRM. (a) 2D phantom. (b) The iterations of the LSPDIPM from iteration 1 (the upper corner in the left hand side) to 20 (the lower corner in the right hand side). (c) The final reconstructed image.

each method requires to reach to convergence. According to the results, the GN approach needs 3 to 5 iterations to reach to convergence, vs. 10 to 20 iterations for the PDIPM and 10 to 20 iterations for the proposed LSPDIPM. Figure 7.1(a) shows the applied 2D phantom with two inclusions with conductivity of 0.9 S/m. The reconstructed images for every iteration of the LSPDIPM are shown in figure 7.1(b). The final reconstructed image using the LSPDIPM is demonstrated in figure 7.1(c).

In the next chapter, I compare the the performance of the proposed LSPDIPM with four competing regularization methods, GN with Tikhonov regularization term, GN with NOSER algorithm, TV, and the PDIPM with L1 norms on the data mismatch and regularization terms. To account for the possible systematic and random errors occurring in EIT data acquisition process, four possible measurement conditions are considered as follows: 1) when there is no noise and no data outliers, 2) with the presence of additive 14 dB Gaussian noise, 3) with the presence of strong data outliers, and 4) when there are

both the 14 dB Gaussian noise and data outliers. The proposed LSPDIPM is the winning method which is not highly suffered from the measurement noise and data outliers. The reconstruction images of the LSPDIPM are sharp images with little image artifacts, where the EIT simulated data is perturbed by synthetic additive of 14 dB Gaussian noise and strong data outliers. The proposed LSPDIPM are also compared against the competing methods over EIT human lung data. The LSPDIPM offers high contrast, low noise lung image with highly well defined ventilated regions when comparing with the competing methods.

Moreover, the robustness of the reconstruction methods against the measurement errors are quantitatively evaluated in the next chapter and the proposed LSPDIPM shows the highest robustness when compared with the competing methods.

Chapter 8

Evaluation Framework to Compare the Performance of the State of the Art Image Reconstruction Algorithms with that of the Proposed Image Reconstruction Methods

This chapter assesses qualitatively and quantitatively the performance of the proposed reconstruction methods in this thesis when compared with four competing methods. The robustness of the proposed reconstruction methods against noise and data outliers are measured and compared with that of competing methods under the same measurement conditions. The four competing methods are:

- **Iterative GN with Tikhonov regularization term:** which applies L2 norms on both the data and image terms of the inverse problem,
- **GN with Noser algorithm:** which calculates the inverse solution faster when compared with Tikhonov regularization method and applies the L2 norms on the data and image terms,
- **Total variation method:** which is known to be effective in the reconstruction of

sharp interfaces due to applying the L1 norm on the image term (the data term is based on the L2 norm),

- **L1 norm based inverse problem using the PDIPM framework:** which is referred to as the PDIPM method in this thesis and has been proposed by Borsic and Adler (2012). The PDIPM applies the L1 norms on both the data and image terms of the inverse problem. It has been shown that the PDIPM is beneficial to rebuild the sharp interfaces in the medium and also it is robust against noise and data outliers due to applying the L1 norms (Borsic and Adler, 2012).

The quantitative comparisons between competing methods are accomplished by applying five morphological features and two shape features to assess the accuracy of the reconstructed images, obtained from EIT simulated data, when compared with the real profile (ground truth). To evaluate the robustness of the reconstruction methods against the potential uncertainties, such as measurement noise and data outliers, a robustness metric (noise measurement) is considered which measures the extent to which a random input measurement noise is amplified in the reconstructed image (output).

8.1 Simulated data

The comparison between the reconstruction methods was accomplished over EIT simulated data. The difference EIT system is simulated with 16 electrodes on one electrode plane discretized using a circular FEM. Figure 8.1 shows the 2D phantom applied to generate EIT simulated data with 1024 mesh elements. The phantom contains two sharp inclusions with the same conductivity located in the upper and the lower part of the mesh. Two objects with different shapes (big object and narrow object) are selected in order to challenge the performance of the applied image reconstruction methods in reconstructing a correct

shape. The applied phantom is already implemented and used in EIDORS, which provides free software algorithms for tomographic imaging and diffusion based optical tomography (Adler and Lionheart, 2005). The narrower the object, the harder the reconstruction will be. This is because the traditional image reconstruction methods fail to reconstruct the shape of a high contrast inclusion and usually create a blubby shape. When compared with a big circular object, a narrow object challenges more an image reconstruction method in producing an accurate shape representation of the object. The conductivity value of the homogeneous background is 1 $\frac{S}{m}$ and the inclusions have the conductivity of 0.5 $\frac{S}{m}$. The inverse problem used the mesh density of 576 elements, which was different than the mesh density of the forward problem (1024 elements). For every reconstruction method, the optimum hyperparameter is selected using the L-curve method. For the four competing methods, a post-processing is also accomplished to obtain an ROI, which defines the main inclusions in the medium.

Figure 8.1: 2D circular phantom used to generate EIT simulated data.

8.2 Quantitative comparison results

To evaluate the accuracy of the reconstructed images obtained from the competing reconstruction methods as well as the proposed ones, a quantitative evaluation using morpholog-

ical and shape features is accomplished. The proposed LSRMs automatically reconstructs the main inclusions (ROIs) in the medium with high contrasts. Therefore, there is no need to a post processing for the proposed LSRMs in order to produce the ROI. For the four competing methods, a binary image to determine the ROI in the image is generated. The ROI is defined to contain those pixels which have an amplitude more or equal to 10% of either the highest amplitude in the image containing a highly conductive inclusion when compared with the background conductivity, or the lowest amplitude in the image including an inclusion with lower conductivity than the background. The ROI is defined as follows:

$$ROI = \begin{cases} \{(x,y)|I(x,y) \geq \frac{10}{100}\ I_{max}\}, & \textit{High conductive inclusion} \\ \{(x,y)|I(x,y) \leq \frac{10}{100}\ I_{min}\}, & \textit{Low conductive inclusion} \end{cases}, \tag{8.1}$$

where $I(x,y)$ is the pixel amplitude at coordination (x,y), I_{max} is the maximum amplitude in the image, and I_{min} is the minimum amplitude in the image. The following five morphological features are considered to evaluate the accuracy of the reconstructed images:

Area (A): which is a scalar indicating the number of the pixels in the ROI.

Perimeter (P): which is a scalar calculating the distance around the border of the ROI.

Axis Ratio (AR): which is a scalar computed as follows:

$$AR = \frac{L_{Major}}{L_{Minor}}, \tag{8.2}$$

where L_{Major} is a scalar and calculated as the length of the major axis of an ellipse that possesses the same normalized second central moments as the ROI, L_{Minor} is a scalar and measured as the length of the minor axis of an ellipse that has the same normalized second central moment as the ROI.

Eccentricity (ECC): which is a scalar showing the extend to which an ROI deviates from

being circular. The eccentricity is defined as:

$$ECC = \frac{D}{L}, \tag{8.3}$$

where D is the distance between the focus points (foci) of an ellipse enclosing the ROI, and L is the ellipse major axis length.

Bounding box (BB): is the smallest box enclosing the ROI. The bounding box is formed as:

$$BB = [x, y, w, h], \tag{8.4}$$

where x and y are the coordination of the upper-left corner of the bounding box and the w and h are the width and the height of the bounding box.

The two shape features are as follows:

Compactness(CF): which is a normalized shape feature calculated as:

$$CF = 1 - \frac{4\pi A}{P^2}, \tag{8.5}$$

where P and A are the perimeter and the area of the ROI, respectively.

Overlap (OV): which is a scalar identifying the overlap between two ROIs as follows:

$$OV = \frac{|A \cap B|}{|A \cup B|}, \tag{8.6}$$

where A is the ground truth, and B is the ROI obtained by the reconstruction algorithm. $OV = 1$ when A and B match perfectly.

Table 8.1 shows the five morphological features (A, P, AR, ECC, BB) as well as the two shape features (CF, OV) calculated for the four competing methods (GN, Noser, TV, and PDIPM) and the proposed LSRMs (LSPDIPM$_{L2-L2}$ and LSPDIPM$_{L1-L1}$).The LSPDIPM$_{L2-L2}$ applies the L2 norms on the data and image terms of the inverse prob-

Table 8.1: Quantitative comparison between the reconstruction methods using statistical metrics

Reconstruction Algorithms	Inclusion	Morphological Features					Shape Features	
		Area	Perimeter	Axis-Ratio	Eccentricity	Bounding-Box	Compactness	Overlap
Ground Truth	Big object	734	113	1.889	0.848	[10.5,32.5,44,22]	0.2747	1
	Narrow object	200	82.4	3.571	0.960	[14.5,10.5,36,11]	0.6301	1
Tikhonov	Big object	925	142	1.757	0.822	[8.5,28.5,48,27]	0.4262	0.7781
	Narrow object	421	111	2.415	0.910	[14.5,7.5,36,17]	0.5654	0.4681
Noser	Big object	964	144	1.692	0.807	[9.5,28.5,46,28]	0.4148	0.7578
	Narrow object	432	91.6	2.291	0.9	[14.5,8.5,36,17]	0.3530	0.4630
TV	Big object	682	104	1.859	0.843	[12.5,32.5,40,21]	0.2067	0.9292
	Narrow object	370	84.3	2.66	0.927	[14.5,8.5,36,14]	0.3455	0.5405
PDIPM	Big object	780	121	1.709	0.811	[9.5,32.5,46,25]	0.3307	0.8878
	Narrow object	481	96.2	2.099	0.879	[14.5,7.5,36,18]	0.3466	0.4158
LSPDIPM$_{L2L2}$	Big object	676	137	1.854	0.843	[11.5,29.5,42,24]	0.55	0.889
	Narrow object	188	78.4	3.604	0.961	[15.5,11.5,34,10]	0.6159	0.8131
LSPDIPM$_{L1L1}$	Big object	602	98.8	1.92	0.854	[12.5,32.5,39,20]	0.2245	0.8202
	Narrow object	321	82.4	2.701	0.929	[14.5,11.5,35,14]	0.4063	0.4158

lem which was discussed in chapter 5 and the LSPDIPM$_{L1-L1}$ utilizes the L1 norms on the inverse problem terms, discussed in chapter 7. The PDIPM is a special state of the proposed GPDIPM, discussed in chapter 6, where the weighting parameters are selected as $[\zeta, \eta]$=[1, 1]. For every feature in table 8.1, three winning methods are highlighted in light gray, medium gray, and dark gray according to their performance. The method which offers the closest feature quantity to the feature value of the ground truth is selected as the best performing method. The highest score of 3 is assigned to the method and its cell in table8.1 is shaded in light gray. The cells for the second best performing method is shaded in medium gray and a score of 2 is assigned to the method. Finally, the cell for the third best performing method is colored in dark gray and a score of 1 is assigned to the method. A similar procedure is applied to all seven features in table 8.1 and the scores are stored to be plotted for the performance comparison. In the case of bounding-box feature, the method with the vector which has the smallest Euclidean distance to the vector of the ground truth is selected as the winning method. Figure 8.2 represents the scores for the

top three best performing methods in the reconstruction of the big object in the medium. The LS and TV with an average score of 2.14 , averaged over the seven features, offer the best performance in the reconstruction of the big object. The PDIPM is the second best performing method with an average score of 1.71. For the big object reconstruction, the GN with Tikhonov regularization method and the GN with the Noser algorithm are not as competitive as the LS, TV, and PDIPM and therefore have not been plotted.

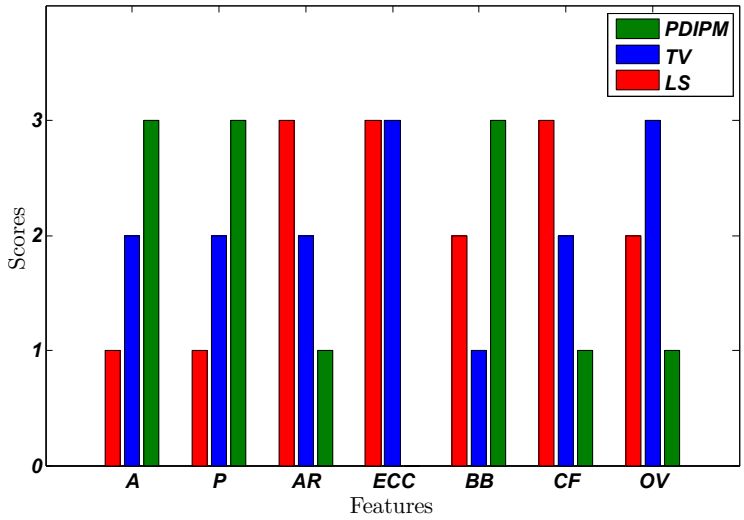

Figure 8.2: Top three best performing reconstruction methods in the reconstruction of the big object in the medium.The higher the score, the higher the reconstruction performance will be. The horizontal axes is the seven features listed in table 8.1

.

Figure 8.3 shows the top three methods (LS, TV, and Tikhonov) which performs well in the reconstruction of the narrow object in the medium. The LS is the winning method with an average score of 3, averaged over the seven features. The LS is always the winning method in the reconstruction of the narrow object and offers the closest feature values to the feature quantities of the ground truth. Specifically, the LSPDIPM$_{L2-L2}$ outperforms the competing methods with a feature vector of $[188, 78.4, 3.604, 0.961, [15.5, 11.5, 34, 10], 0.6159, 0.8131]$ which is close to the feature vector of the ground truth $[200, 82.4, 3.571, 0.960, [14.5, 10.5, 36, 11], 0.6301, 1]$. The TV is the second best performing method in the

reconstruction of the narrow object with an average score of 1.42. The GN with Tikhonov regularization term is the third best performing method with an average score of 0.42. In total, the proposed LSRM offers the highest overall average accuracy score of 2.57 (out of 3), averaged over the achieved accuracy scores in the reconstruction of the big and narrow objects. The TV is the second best performing method with an overall average accuracy score of 1.78. In figure 8.2 and figure 8.3, the LSRM has the highest score of 3 for the shape feature CF. The highest score for the shape features verify that the LSRMs preserve the shape of the inclusions. In the following section, the qualitative analysis again confirms that the LSRMs provides a better shape representation of the inclusions, which is indeed more similar to the actual profile (ground truth) in the medium, when compared with the competing methods, see figure 8.4.

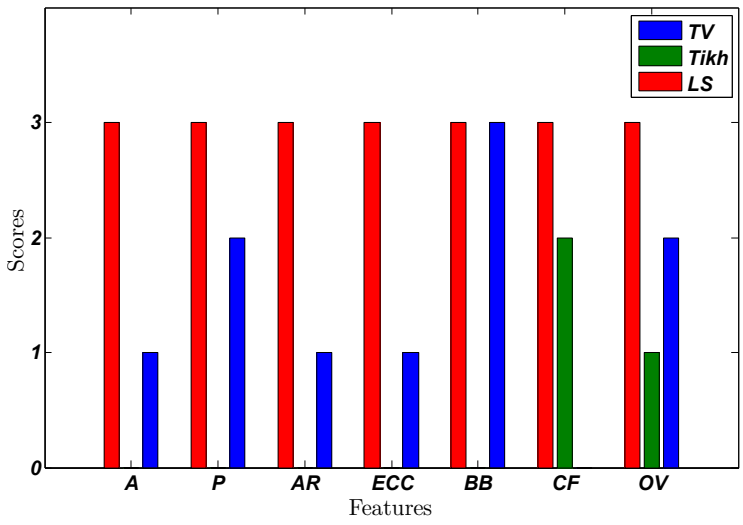

Figure 8.3: Top three best performing reconstruction methods in the reconstruction of the narrow object in the medium.The higher the score, the higher the reconstruction performance will be. The horizontal axes is the seven features listed in table 8.1

.

8.3 Qualitative comparison results

Figure 8.4 compares the performance of the developed LS-PDIPMs with the four state of the art regularization methods. The ROIs for the four competing methods are achieved according to the formulation in (8.1). To account for the possible systematic and random errors occurring in EIT data acquisition process, four possible measurement conditions is considered as follows:

measurement condition#1: which is when there is no measurement noise and no data outliers (figure 8.4(a)),

measurement condition#2: which is when an additional 14 dB zero-mean Gaussian noise is added to EIT simulated data (figure 8.4(b)),

measurement condition#3: which is when there is loss in EIT data due to the presence of strong data outliers (figure 8.4(c)),

measurement condition#4: which is when there are both the 14 dB zero-mean Gaussian noise and data outliers (figure 8.4(d)).

The quantitative performance of the six reconstruction methods when there is no noise and data outliers, the first row of figure 8.4, is previously compared in table 8.1. The visual analysis of the reconstructed images from the six methods, presented in the first row of figure 8.4, indicates that the methods offer an acceptable reconstruction results with two inclusions in the upper and lower section of the medium, which is similar to the actual profile in figure 8.1. However when compared with other competing methods, the LSPDIPM$_{L2-L2}$ method visually provides a better shape representation of the inclusion, especially for the narrow object such that the reconstructed profile is highly similar to the actual profile. In the presence of measurement conditions#3, 4, GN methods fail and do not provide understandable reconstruction results. TV is slightly robust to the measurement condition#2 (figure 8.4(b)); however, it fails in the presence of data outliers (figure 8.4(c)).

PDIPM shows robust results when either noise or data outliers are present (figure 8.4(b) and (c)); however, it fails when the EIT simulated data is perturbed with 14 dB Gaussian noise and strong data outliers (figure 8.4(d)). The proposed LSPDIPM$_{L2-L2}$ is sensitive to the additional noise and data outliers due to the application of the L2 norms in its implementation. The proposed LSPDIPM$_{L1-L1}$ is the winning method which applies the L1 norms on the data and image terms of the inverse problem and therefore does not highly suffer from the measurement noise and data outliers (figure 8.4(d)). The reconstruction images of the LSPDIPM$_{L1-L1}$ (the last column in figure 8.4) are sharp images with little image artifacts, where the EIT simulated data is perturbed by synthetic additive of 14 dB Gaussian noise and strong data outliers. The proposed LSPDIPM was also compared against the competing methods over EIT human lung data (figure 8.4 (e)). The LSPDIPM offers a high contrast, low noise lung image with well defined ventilated regions when comparing with the competing methods. The PDIPM with the L1 norms and the TV show high contrast images; however, fail to properly define the shape of the ventilation and offers a uniform air distribution for the upper and the lower parts of the lungs, which are normally not ventilated uniformly in tidal volume. The LSPDIPM$_{L1-L1}$ show a plausible representation of the lung ventilation in the tidal volume so that the upper and lower part of the lungs are not uniformly ventilated.

8.4 Method robustness against potential uncertainties

In this section, the robustness of the four competing reconstruction methods and the two proposed reconstruction methods are evaluated against potential uncertainties, such as measurement noise and data outliers. The measurement conditions #2, 3, and 4 are considered and the robustness of each method is assessed against the applied measurement condition. The noise measurement (NM) is considered as the robustness metric to measure

the robustness against the possible uncertainties. The NM determines the extend to which a reconstructed image (output) is affected by a random measurement noise (n), occurring in the input, and is defined as follows:

$$NM = \frac{area(I_\Delta)}{\|n\|}; I_\Delta = xor(ROI_t, ROI_n), \tag{8.7}$$

where $area(I_\Delta)$ is a scalar identifying the number of the pixels in the difference image I_Δ, the ROI_t is the ROI achieved from the reconstructed image when there is no noise and data outliers, ROI_n is the ROI obtained from the reconstructed image in the presence of either the noise, data outliers or the both. The NM can be calculated in dB as follows:

$$NMB = 10\ log(NM), \tag{8.8}$$

Table 8.2 shows the quantities of the two robustness metrics (NM, NMB) for the four competing methods as well as the proposed reconstruction methods (LSPDIPM$_{L2-L2}$ and LSPDIPM$_{L1-L1}$) under three different measurement conditions (measurement condition# 2,3, and 4). In most of the measurement conditions, the proposed LSRMs and the PDIPM shows the highest robustness against the uncertainties with lower quantities for the NM and the NMB when compared with other competing methods. In table 8.2, the two successful methods with high robustness against the uncertainties are scored and shaded. For every measurement condition, the cells of the method which possesses the lowest values for the NM and the NMB are colored in light gray and a score of 3 is assigned to the method. The cells of the second method which is successful in dealing with the uncertainties are colored in medium gray and a score of 2 is assigned to the method. In all the measurement conditions, the LSPDIPM$_{L1-L1}$ offers the lowest values for the NM and the NMB and is considered as the winning method with an average robustness score of 3, averaged over three different measurement conditions. The PDIPM with an average robustness score of 1.33 is the second

Table 8.2: Robustness measurement for different image reconstruction methods

Measurement Conditions	Reconstruction Algorithms	Robustness Metrics	
		NM	NMB (dB)
Additional Noise	Tikhonov	3551	81.7
	Noser	2219	77.04
	TV	4006	82.95
	PDIPM	2718	79.07
	LSPDIPM$_{L2L2}$	2408	77.86
	LSPDIPM$_{L1L1}$	1398	72.42
Data Outliers	Tikhonov	1020	69.2
	Noser	882	67.8
	TV	1133	70.3
	PDIPM	112	47.1
	LSPDIPM$_{L2L2}$	919	68.2
	LSPDIPM$_{L1L1}$	79	43.6
Noise and Outliers	Tikhonov	973	68.8
	Noser	862	67.6
	TV	874	67.7
	PDIPM	414	60.2
	LSPDIPM$_{L2L2}$	929	68.3
	LSPDIPM$_{L1L1}$	307	57.2

successful method with a high robustness against the applied uncertainties. In table 8.2, the objective is to measure the robustness of different image reconstruction methods against the same measurement condition. Each measurement condition is independently generated, which means that each sample of the noise is different from one measurement condition to another. Therefore, the values for the NMB should be compared between different image reconstruction methods which have the same measurement condition. The visual analysis of the reconstructed images in figure 8.4 verifies that the LSPDIPM$_{L1-L1}$ (the last column in figure 8.4) always reconstructs the two inclusions under different measurement conditions. After the LSPDIPM$_{L1-L1}$, it is the PDIPM (the fourth column in figure 8.4) which offers high robustness against the measurement errors. The reason for the high

robustness against the uncertainties for the LSPDIPM$_{L1-L1}$ and the PDIPM is because they apply the sum of absolutes (or L1 norms) on the data and image term of the inverse problem.

8.5 Discussion

This chapter proposes an evaluation framework to compare the performance of the image reconstruction methods with that of the proposed image reconstruction methods in this thesis. The proposed evaluation frameworks requires an ROI to be defined over the image plane for the four competing methods. The ROI acts similar to a low pass filter and helps remove the possible image artifacts due to either inherent specifications of the reconstruction algorithm or any possible error in the selection of the optimum hyperparameter. The ROI calculation is considered as a post-processing procedure which indeed acts in favor of the four competing reconstruction methods in the reconstruction of sharper images with well defined boundaries. For instance, the post-processing of the four competing methods removes the ringing effects (the regions surrounding the main inclusions including pixel amplitudes with the opposite sign to those of the main inclusions), and the small image artifacts close to the medium boundary where the surface electrodes are placed.

Two low conductive inclusions with different shapes (one big inclusion, one narrow inclusion) were simulated in a 2D circular phantom and the morphological and shape features are applied to determine the reconstruction accuracy of the competing reconstruction methods. Due to taking advantage of the LS technique in the reconstruction of the inclusion, the proposed LSRMs precisely reconstruct the shape of the narrow inclusion (e.g. the LSPDIPM$_{L2-L2}$ in the first row of figure 8.4) and achieve the highest score of 3 in figure 8.3, while the competing methods mostly over-segment the narrow inclusion. The accuracy measurements for the proposed EPIRMs are achieved for a coarse mesh (578

elements). The accuracy values increases if a fine mesh is applied; however, in the cost of higher computational time.

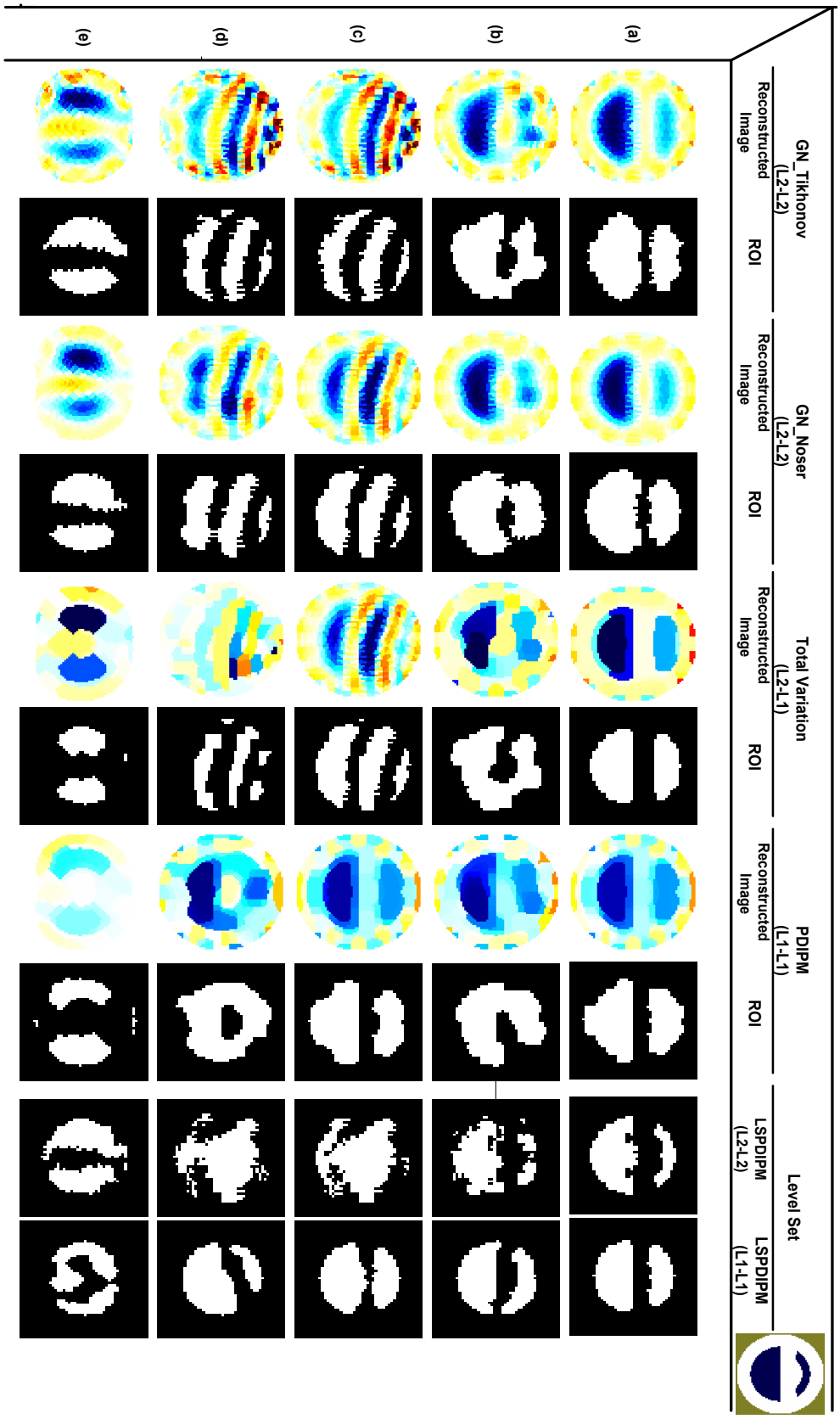

Figure 8.4: Qualitative comparison between the competing methods and the proposed level set based reconstruction methods.

Chapter 9

Conclusion and Future Work

This thesis aims at the improvement of image reconstruction algorithms in terms of the image quality and robustness against potential uncertainties, such as measurement noise and data outliers, by proposing three novel variants of the EPIRMs. This thesis shows that the proposed EPIRMs can be applied to practical inverse problems, such as clinical EIT data (chapter 5), to produce plausible images. The results suggest that such edge preserving approaches help address the blurring of edges inherent in regularized algorithms. The proposed EPIRMs show promising results to help spur interest in using novel edge-preserving algorithms to practical inverse problem applications.

This thesis proposes a generalized inverse problem solving framework (GPDIPM), discussed in chapter 6, which offers a general primal problem including more constraints over the inverse problem terms through introducing weighting parameters. The proposed GPDIPM can be helpful to understand the effect of different combinations of the L1 and L2 norms on the reconstructed image. The clinical results show that the GPDIPM is useful to determine certain spatial inhomogeneities in lung function, which may occur in ALI patients. This thesis shows the mathematical procedure to derive the four standard combinations of the L1 and L2 norms (L2L2, L1L2,L2L1, and L1L1 primal problems). The derivation of the LSRM using the proposed GPDIPM is also discussed in chapter 7.

The inverse solutions for the four standard primal problems are also calculated using the proposed LSPDIPM.

9.1 Conclusions

The aims of this thesis are achieved through the realization of the following four objectives:

- **A level set based reconstruction method using a difference solver.**

  In chapter 5, this thesis proposes the LSRM in difference mode for clinical EIT data of patient ventilation over the inflation manouevre. The first clinical results of applying the LSRM to monitor the air distribution inside the lungs using EIT are investigated. The objective is to measure the shape of the lung ventilation during an incremental PEEP trial in the situation that there is no natural a priori information about the shape of the lung ventilation. The assumption of having a priori shape information about the shape and location of the lungs may not be possible in the case that the a priori information can not be achieved using an X-ray (CT) image, due to the vulnerability of a patient to the X-ray radiation.

  In the proposed difference mode LSRM, the inverse solution of Gauss-Newton formula updates the sensitivity matrix and consequently the LSF with every iteration. In the first iteration, the Ψ is chosen as initial guess. The initial guess is an arbitrary function, for example the definition of a circle. The updated LSF converges to a conductivity map that minimizes the error between measured and simulated data. The minimization of the error function finally leads to the division of the medium into two regions: the background and the foreground. The difference imaging LSRM depicts the capability of finding the big conductivity changes at the interface between lung and the background (figure 5.3 on page 77). A narrow band level set method is

followed up, such as the value of the level set function is thresholded and it is zero at the interface between two materials. The advantage of the narrow band level set method is that it allows the shape evolution without the need to re-formulate the geometrical boundaries of the inclusions. The mapping function is used to discourage the reconstruction of the disconnected contours located at different levels. The update sensitivity matrix has been calculated on a narrow band region, involving the elements sharing an edge with the interface between foreground and background (see figure 5.2 on page 75). The narrow band region causes the LSRM runs faster when comparing with the LSRM calculating the sensitivity matrix over the whole elements for every iteration.

To achieve a more accurate interface where there are more than two highly different conductivities inside the medium, such as lungs, heart, and the peripheral tissues, it is suggested to apply two different LSFs in defining the medium (Dorn and Lesselier, 2009; DeCezaro et al., 2009).

The results represent that the difference formulation of LSRM is suitable to be applied for clinical EIT data of patient ventilation over lung inflation(figure 5.3 on page 77, figure 5.4 on page 78, figure 5.5 on page 80). Comparing with the VBRM, the LSRM shows high contrast lung images corresponding to the physiologically known shape of lung air distribution in these patients (figure 5.4 on page 78, third row, and figure 5.5 on page 80, third row).The NSEC curves (figure 5.6 on page 81) are similar in shape in the LSRM to the VBRM, but show a slower start at the low lung inflation, reflecting perhaps some non-linearity for small conductivity changes.

- **A generalized primal-dual interior point method.**

  In chapter 6, this thesis derives a generalized inverse problem framework which mixes the L1 norms and the L2 norms on both the data and the regularization terms of an

inverse problem. To reach to the maximum generality, the norms are weighted to enclose the maximum number of possible categories of inverse problems. The classical inverse problems such as L2L2, L1L2, L2L1, and L1L1 problems are a sub-domain of the proposed generalized inverse problem where the weighting factors are selected accordingly. The generalized solution of the proposed inverse problem is derived using the PDIPM framework. EIT is selected as an instance of ill-posed non-linear inverse problem. The chapter discusses the effectiveness of different combination of weighted norms (L1 and L2 norms) under two different measurement conditions on EIT simulated data (added noise and outliers). Moreover, the performance of the proposed GPDIPM is assessed on clinical data achieved from the EIT system. This chapter shows that the achieved clinical results of the proposed GPDIPM are plausible and also found that the assignment of larger values to the weighting parameters (ζ and η) is beneficial to produce sharp and less noisy images in clinical application of EIT for lung imaging.

- **A level set based primal-dual interior point method.**

  In chapter 7, this thesis derives a novel level set based regularization method, called LSPDIPM, that allows any possible combination of norms (L1 norm or L2 norm) on the data term and the regularization term. The proposed LSPDIPM incorporates the benefit of applying level set technique to reconstruct sharp images as well as using the L1 norms in the formulation of inverse problems. The L1 norm in inverse problem is beneficial because it provides high robustness against outliers and spatial noise. However, the L1 norm is not differentiable everywhere. In the derived LSPDIPM, the non-differentiability of L1 norm based term in the primal problems has been resolved through the centering condition.

  Moreover, the numerical solution of three standard inverse problems (L1L2 problem,

L2L1 problem, and L1L1 problem) are calculated using the proposed LSPDIPM framework.

The proposed LSPDIPM can be applied to solve inverse problems raised in many sciences. This thesis shows the implementation of the proposed LSPDIPM using Electrical Impedance Tomography as a test case. Electrical Impedance Tomography is an ill-posed inverse problem used to image the spatial distribution of electrical conductivity within a volume. I believe that the proposed LSPDIPM can be successfully applied in a variety of inverse problem applications.

- **A solid evaluation framework to compare the performance of the image reconstruction methods.**

  Finally in chapter 8, this thesis proposes a solid evaluation framework to qualitatively and quantitatively compare the performance of the proposed edge-preserving image reconstruction algorithms, discussed in chapters 5, 6, and 7, with that of four competing methods. The four competing methods considered for the comparison are as follows: 1) GN with Tikhonov regularization term, 2) GN with Noser algorithm, 3) Total variation method, and 4) The PDIPM. The proposed edge preserving image reconstruction methods offer the highest accuracy in the reconstruction of two low conductive inclusions with an overall average accuracy score of 2.57 (out of 3), vs. 1.78 for TV as the second best performing method. The robustness of the methods against potential uncertainties, such as measurement noise and data outliers, was assessed using two robustness metrics (noise factor, and noise figure). The results represent that the proposed edge preserving image reconstruction method with the L1 norms on the image and data terms of the inverse problem offers the highest robustness against measurement errors with an average robustness score of 3 (out of 3), averaged over three different measurement conditions. The PDIPM with the L1

norms on the data and image terms offers an average robustness score of 1.33 and is the second robust method in dealing with the uncertainties. The qualitative comparison in figure 8.4 on page 135 also confirms the achieved quantitative robustness results. A visual analysis over the last column of figure 8.4 on page 135 verifies that the reconstructed inclusions form the LSPDIPM with the L1 norms on the data and image terms of the inverse problem are more similar to the actual inclusions (ground truth) in the presence of both zero-mean Gaussian noise and data outliers, when compared with the reconstructed inclusions from other competing methods.

The computational complexity of the proposed EPIRMs can be compared with that of the traditional GN method in terms of the number of the iterations required to reach to convergence. According to the experimental results, the proposed EPIRMs need 15 to 20 iterations to reach to convergence, vs. 3 to 5 iterations for the non-linear GN method.

9.2 Future work

This thesis proposes three novel variants of the EPIRMs in chapters 5, 6, and 7. The idea of applying the LS technique to solve an inverse problem has been studied for a decade now. This thesis applies the LS technique to calculate the inverse solution of a non linear inverse problem containing different combinations of the L1 and L2 norms, applied independently over the inverse problem terms. In chapters 5, and 7, the LS parameterizations are introduced into a non linear inverse problem to reconstruct sharp interfaces. During the contextual development of this thesis, several interesting research areas to discover the benefits of applying the LS technique to an inverse problem have been concerned. The following subjects are most significant areas of future work that can be considered beneficial in improving the capabilities and integrity of the proposed EPIRMs.

- **Deformable model regularization method.**

  In the literature, there are several studies which focus on the undesired effect of the electrode displacements in the EIT reconstructed image. To resolve the effect of the electrode displacements, the traditional regularization method is reformulated in order to calculate the electrode displacements as part of the inverse solution (Lionheart, 1998; Kiber et al., 1990; Kolehmainen et al., 2005). The electrode displacements are compensated for in the reconstruction methods proposed by Blott et al. (1998); Kolehmainen et al. (2005). An iterative inverse problem to calculate the deformable boundary shape is investigated in the past by Blott et al. (1998). However due to the boundary movement, it is not only the electrodes which change their coordinations but the nodes inside the mesh too. Therefore, it is essential for the reconstruction algorithm to take into account the calculation of the following three model parameters from the measured data: 1) The conductivity image, 2) The electrode displacements, and 3) The node displacements inside the mesh. The formulation of such reconstruction method is proposed as an extended research work for this thesis. In the following, the idea of calculating the three aforementioned model parameters in the framework of a non-linear inverse problem is briefly presented.

  The proposed deformable model regularization method is described for an EIT system which is considered as a non-linear inverse problem. A model of a conductive medium can be obtained through applying the FEM to divide the medium into N_e elements and N_n nodes. The electrodes are shown as nodes at the boundary of the mesh and the number of the electrodes is determined by N_E. Difference EIT is considered due to its benefit in reconstructing the conductivity changes in the tissues in medical applications, which is prone to high level of measurement errors such as electrode movements and shape deformation. The difference data vector at

frame t_1 is calculated as: $V_{t_1} = v_{t2} - v_{t1}$, where v_{t_1} and v_{t_2} are vectors of differential voltage measurements, with a dimension of $N_E \times 1$ at frame t_1 and t_2, respectively. The conductivity changes vector is written as: $\Delta\sigma_{t_1} = \sigma_{t_2} - \sigma_{t1}$, where σ_{t_1} and σ_{t_2} are the conductivity vectors, with a dimension of $N_e \times 1$, at frame t_1 and t_2, respectively. Shape deformation causes two displacements in the model: 1) Electrode displacements, 2) Node displacement. An electrode displacement vector d_e and a node displacement vector d_n for the described model between frame t_1 and t_2 can be written as:

$$\begin{aligned} d_e^k &= (x_{t_2}^k - x_{t_1}^k)\hat{\mathbf{i}} + (y_{t_2}^k - y_{t_1}^k)\hat{\mathbf{j}} + (z_{t_2}^k - z_{t_1}^k)\hat{\mathbf{k}}; k = 1, \ldots, N_E, \\ d_n^l &= (x_{t_2}^l - x_{t_1}^l)\hat{\mathbf{i}} + (y_{t_2}^l - y_{t_1}^l)\hat{\mathbf{j}} + (z_{t_2}^l - z_{t_1}^l)\hat{\mathbf{k}}; l = 1, \ldots, N_e, \end{aligned} \tag{9.1}$$

where $(x_{t_1}^k, y_{t_1}^k, z_{t_1}^k)$, and $(x_{t_2}^k, y_{t_2}^k, z_{t_2}^k)$ are the node coordinates of the electrode numbered k at the boundary of the medium at frames t_1 and t_2, respectively, $(x_{t_1}^l, y_{t_1}^l, z_{t_1}^l)$, and $(x_{t_2}^l, y_{t_2}^l, z_{t_2}^l)$ are the node coordinates of the element numbered l inside the medium at frames t_1 and t_2, respectively.

A forward deformable model can be written as follows:

$$V = h(m), \tag{9.2}$$

where V is the difference data vector, h is the forward operator based on the FEM, m is the system parameters which includes: 1) The conductivity changes image σ, 2) Node displacement d_n, and 3) Electrode displacement d_e,. Matrix m is assembled as three sub-matrices as follows:

$$m = [\sigma d_n d_e]^T, \tag{9.3}$$

where m is a single column vector with the length of $(N_k + N_D N_n + N_D N_E)$, N_D is the dimension of the FEM and is 2 for 2D mesh and 3 for 3D mesh. The objective is to reconstruct an image, modeled as m, which represents the conductivity changes, node displacements, and the electrode displacements using an inverse calculation framework. In the following the inverse calculation for the forward deformable model in (9.2) is described.

An inverse solution for the forward deformable model can be written using the regularized MAP method (Polydorides, 2002):

$$m_{MAP} = (J^T \sum\nolimits_n^{-1} J + \sum\nolimits_m^{-1})^{-1} (J^T \sum\nolimits_n^{-1} V + \sum\nolimits_m^{-1} m_{prior}), \tag{9.4}$$

where J is a Jacobian matrix, $\sum_m^{-1}$ is the a priori covariance estimates of the image m, $\sum_n^{-1}$ is the a priori covariance estimates of measurement noise n, and m_{prior} is the a priori bias for the inverse solution which is zero in the case there is no a priori information, which is the assumption in the rest of the inverse calculation procedure. Similar to the image matrix, the Jacobian matrix J is constituted as three sub-matrices as follows:

$$J = [J_\sigma J_N J_E], \tag{9.5}$$

where J_σ is a sensitivity matrix to the conductivity changes with the dimension of $[N_M \times N_e]$, J_N is a sensitivity matrix to the node displacements with the size $[N_M \times N_n]$, and J_E is a sensitivity matrix to the electrode displacements with the

size of $[N_M \times N_E]$. The Jacobian sub-matrices J_σ, J_N, and J_E can be written as:

$$J_\sigma = \begin{pmatrix} \frac{\partial V_1}{\partial \sigma_1} & \cdots & \frac{\partial V_1}{\partial \sigma_{N_e}} \\ \cdots & \cdots & \cdots \\ \frac{\partial V_{N_M}}{\partial \sigma_1} & \cdots & \frac{\partial V_{N_M}}{\partial \sigma_{N_e}} \end{pmatrix} J_N = \begin{pmatrix} \frac{\partial V_1}{\partial N_1} & \cdots & \frac{\partial V_1}{\partial N_{N_D N_n}} \\ \cdots & \cdots & \cdots \\ \frac{\partial V_{N_M}}{\partial N_1} & \cdots & \frac{\partial V_{N_M}}{\partial N_{N_D N_n}} \end{pmatrix}, J_E = \begin{pmatrix} \frac{\partial V_1}{\partial E_1} & \cdots & \frac{\partial V_1}{\partial E_{N_D N_E}} \\ \cdots & \cdots & \cdots \\ \frac{\partial V_{N_M}}{\partial E_1} & \cdots & \frac{\partial V_{N_M}}{\partial E_{N_D N_E}} \end{pmatrix} \tag{9.6}$$

Each Jacobian sub-matrix can be calculated using the perturbation method. For example, J_N is the ratio of the change in the measured data to a very small displacement of nodes along dimension N_D. The Jacobian matrix J can be calculated using the forward model with a small perturbation $m \to m + \Delta m$ as follows:

$$J = \frac{h(m + \Delta m)}{\Delta m}, \tag{9.7}$$

where the single column vectors $m = [\sigma d_n d_e]$, and $\Delta m = [\Delta\sigma \Delta d_n \Delta d_e]$. An assumption of an additive zero-mean Gaussian noise with the following statistical properties: $En = 0$, and $Enn^T = \sum_n = w_n^2 I$, where w_n is a scaling factor of the noise amplitude and I is an identity matrix, can be considered. The a priori covariance estimates of the image $\sum_m = Em^2$. A regularization matrix $R = \sum_m^{-1}$ with the size of $[N_e + N_D N_n + N_D N_E \times N_e + N_D N_n + N_D N_E]$ and a weighting matrix $W = \sum_n^{-1}$ with the size of $[N_M \times N_M]$ are defined. In the case that the conductivity elements, node displacement components, and electrode displacement components are uncorrelated, the cross-correlation between σ, d_n, and d_e is zero and the regularization matrix can be written as follows:

$$R = \begin{pmatrix} R_\sigma^* & 0 & 0 \\ 0 & R_N^* & 0 \\ 0 & 0 & R_E^* \end{pmatrix} \tag{9.8}$$

where R_σ^* is the covariance sub-matrix with the size of $[N_e \times N_e]$ for the conductivity

change image, R_N^* is the covariance sub-matrix with the size of $[N_D N_n \times N_D N_n]$ for the node displacements, and R_E^* is the covariance sub-matrix with the size of $[N_D N_E \times N_D N_E]$ for the electrode displacements. The covariance of the image m is written as:

$$\sum\nolimits_m^{-1} = R = \frac{1}{w_\sigma^2} R_\sigma + \frac{1}{w_N^2} R_N + \frac{1}{w_E^2} R_E, \tag{9.9}$$

where w_σ, w_N, and w_E are the a priori amplitude of conductivity change image, node displacement, and electrode displacement, respectively, and:

$$R_\sigma = \begin{pmatrix} R_\sigma^* & 0 & 0 \\ 0 & 0 & 0 \\ 0 & 0 & 0 \end{pmatrix}, R_N = \begin{pmatrix} 0 & 0 & 0 \\ 0 & R_N^* & 0 \\ 0 & 0 & 0 \end{pmatrix}, R_\sigma = \begin{pmatrix} R_\sigma & 0 & 0 \\ 0 & 0 & 0 \\ 0 & 0 & R_E^* \end{pmatrix}, \tag{9.10}$$

Adler and Guardo (1996) proposes a discrete Laplacian filter, which acts as a spatial high pass filter, for R_σ^* such that the diagonal elements of the matrix R_σ^* are set to $N_D + 1$, the off-diagonal, adjacent elements with N_D shared nodes are set to -1 , and other elements are set to zero. The same idea can be applied for R_N^*, and R_E^*. In (Soleimani et al., 2006b), the inter-element displacement correlation are assumed to be non-zero and therefore the electrode displacement covariance matrix is constituted as follows: The diagonal elements in R_E^* are set to 2.1, the off-diagonal elements for adjacent electrodes are set to -1, and are otherwise set to 0. The node displacement covariance matrix R_N^* can be formed as follows: The diagonal elements in R_N^* are set to 2.1, the off-diagonal elements for adjacent nodes are set to -1, and are otherwise set to 0. By introducing the covariance matrices into (9.4), the regularized MAP solution for the deformable model can be obtained as:

$$m_{MAP} = (J^T \frac{1}{w_n^2} IJ + \frac{1}{w_\sigma^2} R_\sigma + \frac{1}{w_N^2} R_N + \frac{1}{w_E^2} R_E)^{-1} (J^T \frac{1}{w_n^2} IV + \frac{1}{w_n^2} I m_{prior}), \tag{9.11}$$

Assuming that there is no a priori information to bias the solution, i.e. $m_{prior} = 0$, the inverse solution is as:

$$\begin{aligned} m_{MAP} &= (J^T \frac{1}{w_n^2} IJ + \frac{1}{w_\sigma^2} R_\sigma + \frac{1}{w_N^2} R_N + \frac{1}{w_E^2} R_E)^{-1} J^T \frac{1}{w_n^2} IV \\ &= (J^T J + \frac{w_n^2}{w_\sigma^2} R_\sigma + \frac{w_n^2}{w_N^2} R_N + \frac{w_n^2}{w_E^2} R_E)^{-1} J^T V \\ &= (J^T J + \frac{w_n^2}{w_\sigma^2} (R_\sigma + \frac{w_\sigma^2}{w_N^2} R_N + \frac{w_\sigma^2}{w_E^2} R_E))^{-1} J^T V, \end{aligned} \tag{9.12}$$

we define:

$$\lambda = \frac{w_n}{w_\sigma}, \eta = \frac{w_\sigma}{w_N}, \zeta = \frac{w_\sigma}{w_E}, \tag{9.13}$$

where λ is Tikhonov regularization factor, or hyperparameter, η is the node displacement regularization factor, ζ is the electrode displacement regularization factor. By replacing the regularization factors into (9.12), the inverse solution of the proposed deformable model regularization method is achieved as:

$$\begin{aligned} m_{MAP} &= (J^T J + \lambda^2 (R_\sigma + \eta^2 R_N + \zeta^2 R_E))^{-1} J^T V \\ &= (J^T J + \lambda^2 R_\alpha)^{-1} J^T V, \end{aligned} \tag{9.14}$$

where $R_\alpha = R_\sigma + \eta^2 R_N + \zeta^2 R_E$ is the regularization matrix and can be written as:

$$[R_\alpha]^{(i,j)} = \begin{cases} N_D + 1 & i = j \ \& \ i \leq N_e \\ -1 & \text{elements } i,j \text{ are adjacent } \& \ i \leq N_e \\ 2.1\eta^2 & i = j \ \& \ i > N_e \\ -\eta^2 & \text{nodes } i,\ j \text{ are adjacent } \& \ i > N_e \\ 2.1\zeta^2 & i = j \ \& \ N_e < i \leq (N_e + N_D N_n) \\ -\zeta^2 & \text{electrodes } i,\ j \text{ are adjacent } \& \ N_t < i \leq (N_t + N_D N_E) \\ 0 & \text{otherwise.} \end{cases} , \tag{9.15}$$

where $N_t = N_e + N_D N_n$.

- **Shape reconstruction using a level set based deformable regularization method.**

  The LS technique is well-known to track fast changing interfaces and is able to reconstruct topological changes in a structure. This thesis applies the proposed LSRMs on EIT lung data to reconstruct the air distribution inside the lungs. However, the reconstruction algorithms apply a fixed thorax model to reconstruct the ventilated regions inside the lungs. In a practical situation, the thorax volume changes by breathing in and out. It is beneficial to simulate a deformable thorax model so that all elements within the model have displacement in accordance to the breathing. It is expected that a significant imaging enhancement is achieved by applying a deformable thorax model. To realize an level set based deformable regularization method, the level set parameterizations, introduced in chapter 5, have to introduced into the proposed deformable regularization method in (9.14). Given the difference measurement

data V, an image $m = [\Phi(\Psi)d_n d_e]$ with the size of $[(N_k + N_D N_n + N_D N_E) \times 1]$ is reconstructed, where Ψ is the level set function and Φ is the applied mapping function which assigns the given Ψ to the corresponding conductivity distribution σ by $\sigma = \Phi(\Psi)$. The proposed level set based deformable regularization method applies the level set technique, described in chapter 5, to reconstruct the conductivity change image $\Phi(\Psi)$. The reconstruction of node displacement d_n and electrode displacement d_e is accomplished with the same procedure explained in the previous section. By introducing the level set parameterizations into the forward model $V = h(\Phi(\Psi))$, the inverse solution of the proposed level set based deformable regularization method using the MAP estimator can be obtained as:

$$m_{MAP} = (\tilde{J}^T \tilde{J} + \lambda^2 (R_\Psi + \eta^2 R_N + \zeta^2 R_E))^{-1} \tilde{J}^T V \tag{9.16}$$

where $\tilde{J} = [J_{LS} J_N J_E]$. J_N, and J_E is computed with the same procedure explained in the previous section for the proposed deformable regularization method; however, J_{LS} has to be calculated using the following chain rule as:

$$J_{LS} = \frac{\partial V}{\partial \Psi} = (\frac{\partial h}{\partial \Phi(\Psi)})(\frac{\partial \Phi(\Psi)}{\partial \Psi}) = (J_\sigma)(M), \tag{9.17}$$

where $\frac{\partial h}{\partial \Phi(\Psi)}$ stands for the traditional Tikhonov sensitivity matrix (J_σ), and $\frac{\partial \Phi(\Psi)}{\partial \Psi} = M$.

- **A hybrid regularization framework.**

The common LSRM is applied to solve an inverse problem with constant piece-wise coefficients using one level set function and considers the assumption of having two different pixel illumination values for the background and the inclusion (two constant piece-wise coefficients). The assumption of constant piece-wise pixel illumination val-

ues is to discriminate between two regions with sharp intensity transition; however, it may not be a realistic assumption when there are smooth conductivity gradients inside each region as well. A hybrid regularization method (HRM), which is a two steps solution, to solve ill-posed, non-linear inverse problem containing both sharp and smooth coefficients can be proposed. The proposed HRM acts in a similar way as a *source type* inversion method (Dorn et al., 2000), which divides a non-linear inverse problem into two stand-alone subproblems. The first step of the proposed hybrid inversion framework plays the role of an initializing procedure for the second step. In the first stage, the LSRM with one level set function is applied to determine an ROI, defined as the region with sharpest interface. Then in the second stage, an inverse solver with penalty terms based on the sum of absolute values (L1 norms), which are highly robust against measurement errors, is applied to reconstruct the smooth intensity values inside the determined ROI. The generated forward solution in the final iteration of the level set is fed to the second stage where the L1 norm based penalty terms are minimized using the PDIPM framework. The PDIPM framework has been shown to be a successful optimization framework in minimizing the L1 norms. To show the implementation of the proposed HRM and to assess its performance, EIT system, as an instance of ill-posed, non-linear inverse problem, can be applied. It is expected that the EIT reconstructed images using the proposed HRM maintain the sharp edges as well as the smooth intensity variations, a trait absent in all previously established LSRMs. A preliminarily study has been already accomplished on the proposed HRM. The achieved results were published in a conference paper entitled as *A Hybrid Regularization Method for Image Reconstruction of Electrical Impedance Tomography*, *Peyman Rahmati, and Andy Adler*, *17th International Conference on Image Processing, Computer Vision, and Pattern Recognition*, Las Vegas, US, 2013.

Bibliography

R. Acar and C. R. Vogel. Analysis of bounded variation penalty methods for ill-posed problems. *Inverse Problems*, page 1217, 1994.

A. Adler and R. Guardo. Electrical impedance tomography: Regularized imaging and contrast detection. *IEEE Trans Med Imgaging*, page 170, 1996.

A. Adler and W. R.B. Lionheart. Eidors: Towards a community-based extensible software base for eit. *6th Conference on Biomedical Applications of Electrical Impedance Tomography*, page 53, 2005.

A. Adler and W.R.B. Lionheart. Uses and abuses of eidors: an extensible software base for eit. *Physiological measurement*, page 25, 2006.

A. Adler, R. Guardo, and Y. Berthiaume. Imaging of gastric emptying with electrical impedance tomography. *Canadian Medical and Biolological Eng. Soc.*, page 14, 1994.

A. Adler, R. Guardo, and Y. Berthiaume. Impedance imaging of lung ventilation: Do we need to account for chest expansion? *IEEE Trans. Biomed. Eng.*, page 414, 1996.

A. Adler, R. Amyot, R. Guardo, J. H. Bates, and Y. Berthiaume. Monitoring changes in lung air and liquid volumes with electrical impedance tomography. *Journal of Applied Physiology*, page 1762, 1997.

A. Adler, T. Dai, and Lionheart. Temporal image reconstruction in electrical impedance tomography. *Physiological measurement*, page 1, 2007.

A. Adler, J. H. Arnold, R. Bayford, A. Borsic, B. Brown, P. Dixon, T. J. C. Faes, I. Frerichs, H. Gagnon, Y. GÃďrber, B. Grychtol, G. Hahn, W. R. B. Lionheart, A. Malik, R. P. Patterson, J. Stocks, A. Tizzard, N. Weiler, and G. K. Wolf. Greit: a unified approach to 2d linear eit reconstruction of lung images. *Physiological Measurement*, page 35, 2009.

K. D. Andersen, E. Christiansen, A. Conn, and M. L. Overton. An efficient primal-dual interior-point method for minimizing a sum of Euclidean norms. *SIAM J. on Scientific Computing*, page 243, 2000.

D. Augusto, B. Oliveira R. Queiroz Feitosa, and M. Correia. Liver segmentation using level sets and genetic algorithms. *Proceedings of the Fourth International Conference on Computer Vision Theory and Applications*, page 5, 2009.

R. Banasiak and M. Soleimani. Shape based reconstruction of experimental data in 3d electrical capacitance tomography. *NDT&E International*, page 241, 2010.

A. Binley and W. Daily. The performance of electrical methods for assessing the integrity of geomembrane liners in landfill caps and waste storage ponds. *J. Environ. Engng Geophys.*, page 227, 2004.

B. H. Blott, G. J. Daniell, and S. Meeson. Nonlinear reconstruction constrained by image properties in electrical impedance tomography. *Phys. Med. Biol.*, page 1215, 1998.

B. Borchers. Total variation regularisation. *Technical Report. New Mexico Institute of Mining and Technology, USA*, page 224, 2000.

A. Borsic and A. Adler. A primal dual - interior point framework for using the l1-norm or

the l2-norm on the data and regularization terms of inverse problems. *Journal of Inverse Problems*, page 112, 2012.

A. Borsic, C. N. McLeod, and W. R. B. Lionheart. Total variation regularisation in EIT reconstruction. *Proceedings of the 2nd World Congress on Industrial Process Tomography*, page 741, 2001.

A. Borsic, W.R.B. Lionheart, and C. N. McLeod. Generation of anisotropic-smoothness regularization filters for EIT. *IEEE Transactions on Medical Imaging*, page 579, 2002.

A. Borsic, B.M. Graham, A. Adler, and W.R.B. Lionheart. In Vivo Impedance Imaging with Total Variation Regularization. *IEEE Transaction on Medical Imaging*, page 44, 2010.

Andrea Borsic. *Regularisation Methods for Imaging from Electrical Measurements*. PhD thesis, Oxford Brookes University, School of Engineering, 2002.

S. J. Bourke. *Respiratory medicine*. Wiley-Blackwell, Chapter 11, 2003a.

S. J. Bourke. *Respiratory medicine*. Wiley-Blackwell, Chapter 1, 2003b.

G. Boverman, M. Khames, and E. L. Miller. Recent work in shape-based methods for diffusive inverse problems. *Review of Scientific Instruments*, page 2580, 2003.

G. Boverman, B. S. Kim, D. Isaacson, and J. C. Newell. The complete electrode model for imaging and electrode contact compensation in electrical impedance tomography. *Engineering in Medicine and Biology Society, 2007. EMBS 2007. 29th Annual International Conference of the IEEE*, page 3462, 2007.

M. Bruhl. Explicit characterization of inclusions in electrical impedance tomography. *SIAM J Math Anal*, page 1327, 2001.

T. Chan and P. Mulet. Iterative methods for total variation restoration. *UCLA CAM*, page 221, 1996.

T. Chan, G. Golub, and P. Mulet. A nonlinear primal-dual method for total variation-based image restoration. *ICAOS'96*, page 241, 1996.

T. F. Chan and X. C. Tai. Level set and total variation regularization for elliptic inverse problems with discontinuous coefficients. *Journal of Computational Physics*, page 40, 2004.

T. F. Chan, H. M. Zhou, and R. H. Chan. A continuation method for total variation denoising problems. *UCLA CAM Report 95-18*, page 553, 1995.

M. Cheney, D. Isaacson, J. C. Newell, S. Simake, and J. Goble. NOSER: An algorithm for solving the inverse conductivity problem. *Int J Imag Sys Technol*, page 66, 1990.

P. Church, J. E. McFee, S. Gagnon, and P. Wort. Electrical impedance tomographic imaging of buried landmines. *IEEE Transaction of Geoscience and Remote Sensing*, page 2407, 2006.

A. DeCezaro, A. LeitÃčo, and X. C. Tai. On multiple level-set regularization methods for inverse problems. *Inverse Problem*, page 34, 2009.

D. C. Dobson and C. R. Vogel. Convergence of an iterative method for total variation denoising. *SIAM J. on Numerical Analysis*, page 1779, 1997.

O. Dorn and D. Lesselier. Level set methods for inverse scattering-some recent developments. *Inverse Problems*, page 11, 2009.

O. Dorn, E. L. Miller, and C. M. Rappaport. A shape reconstruction method for electro-

magnetic tomography using adjoint fields and level sets. *Inverse problems*, page 1119, 2000.

I. Frerichs. Electrical impedance tomography (eit) in applications related to lung and ventilation: a review of experimental and clinical activities. *Physiological Measurement*, page 1, 2000.

I. Frerichs, T. Dudykevych, J. Hinz, M. Bodenstein, G. Hahn, and G. Hellige. Gravity effects on regional lung ventilation determined by functional eit during parabolic flights. *Journal of Applied Physiology*, page 39, 2001.

I. Frerichs, S. Pulletz, G. Elke, G. Zick, and N. Weiler. Electrical impedance tomography in acute respiratory distress syndrome. *The Open Nuclear Medicine Journal*, page 110, 2010.

N. Gao, S. A. Zhu, and B. He. A new resonance electrical impedance tomography (mreit) algortihm: the rsm–merit algorithm with applications to estimation of human head conductivity. *Phys. Med. Biol.*, page 3067, 2006.

T. Grabowski. *Principles of Anatomy and Physiology*. Wiley, Chapter 23, 2000.

JB. Grotberg. Respiratory mechanics and gas exchange. *Handbook of Biomedical Engineering and Design*, page 873, 2004.

L. He, C. Kao, and S. Osher. Incorporating topological derivatives into shape derivatives based level set methods. *Journal of Computational Physics*, page 1016, 2007.

J. P. Kaipio, V. Kolehmainen, M. Vauhkonen, and E. Somersalo. Construction of nonstandard smoothness priors. *Inverse Problems*, page 713, 1999.

J. P. Kaipio, V. Kolehmainen, E. Somersalo, and M. Vauhkonen. Statistical inversion and monte carlo sampling methods in electrical impedance tomography. *Inverse Problems*, page 1487, 2000.

M. Kass, A. Witkin, and D. Terzopoulos. Snakes: Active contour models. *International journal of Computer Vision*, page 321, 1998.

A. Kiber, D.C. Barber, and B.H. Brown. Estimation of object boundary shape from the voltage gradient measurements. *In Proc. Meet. on Electrical Impedance Tomography*, page 52, 1990.

V. Kolehmainen, M. Lassas, and P. Ola. The inverse conductivity problem with an imperfectly known boundary. *SIAM J. Appl. Math.*, page 365, 2005.

M. Kutz, RS. Adrezin, RE. Barr, C. Batich, RV. Bellamkonda, AJ. Brammer, TS. Buchanan, AM. Cook, JM. Currie, and AM. Dolan. *Standard handbook of biomedical engineering and design*. McGraw-Hill, 2003.

W. R. B. Lionheart. Boundary shape and electrical impedance tomography. *Inverse Problems*, page 139, 1998.

A. Litman, D. Lesselier, and F. Santosa. Reconstruction of a two-dimensional binary obstacle by controlled evolution of a level-set. *Inverse Prob.*, page 685, 1998.

M. H. Loke and R. D. Barker. Rapid least-squares inversion of apparent resistivity pseudosections using quasi-newton method. *Geophysical Prospecting*, page 181, 1996a.

M. H. Loke and R. D. Barker. Practical techniques for 3d resistivity surveys and data inversion. *Geophysical Prospecting*, page 499, 1996b.

AB. Lumb. *Nunn's Applied Respiratory Physiology. 2005.* Oxford: Butterworth-Heinemann, 2005.

P. Manwaring, R Halter, Y. Wan, A. Borsic, A. Hartov, and K. Paulsen. Arbitrary geometry patient interfaces for breast cancer detection and monitoring with electrical impedance tomography. *Conf Proc IEEE Eng Med Biol Soc.*, page 1178, 2008.

Moussavi. *Fundamentals of respiratory sounds and analysis.* Morgan and Claypool, Chapter 1, 2006.

J. Nocedal and S. J. Wright. *Numerical Optimization.* Springer, 1999.

R. Ogilvy, P. Meldrum, J. Chambers, and G. Williams. The use of 3d electrical resistivity tomography to characterise waste and leachate distribution within a closed landfill. *J. Environ. Engng Geophys.*, page 11, 2002.

S. Osher and N. Paragios. Level set methods. *Geometric Level Set Methods in Imaging, Vision, and Graphics*, page 1, 2003.

S. Osher and S. Sethian. Fronts propagation with curvature dependent speed: Algorithms based on hamilton-jacobi formulations. *J. Computational Phys.*, page 12, 1998.

N. Polydorides. *Image Reconstruction Algorithms for Soft-Field Tomography.* PhD thesis, University of Manchester, 2002.

N. Polydorides and W. R. B. Lionheart. A MATLAB based toolkit for three dimensional electrical impedance tomography: A contribution to the EIDORS project. *Meas. Sci. Technol.*, page 1871, 2002.

N. Polydorides, W. R. B. Lionheart, and H. McCann. Krylov subspace iterative techniques:

On the detection of brain activity with electrical impedance tomography. *IEEE Trans Med Imaging*, page 596, 2002.

S. Pulletz, A. Adler, M. Kott, G. Elke, B. Gawelczyk, D. SchÃd'dler, G. Zick, N. Weiler, and I. Frerichs. Regional lung opening and closing pressures in patients with acute lung injury. *Journal of Critical Care*, 2011.

P. Rahmati, A. Adler, and Gh. Hamarneh. Mammography segmentation with maximum likelihood active contours. *Journal of Medical Image Analysis*, page 1167, 2012a.

P. Rahmati, M. Soleimani, S. Pulletz, I. Frerichs, and A. Adler. Level-set-based reconstruction algorithm for eit lung images: first clinical results. *Journal of Physiological Measurement*, page 739, 2012b.

J. M. Reynolds. An introduction to applied and environmental geophysics. *Chichester: John Wiley & Sons*, page 553, 1997.

L. I. Rudin, S. Osher, and E. Fatemi. Nonlinear total variation based noise removal algorithms. *Physica D*, page 259, 1992.

V. Santosa. A level-set approach for inverse problems involving obstacles. *in ESAIM: Control, Optimization and Calculus of Variations*, page 17, 1996.

J. A. Sethian. *Level Set Methods and Fast Marching Methods: Evolving Interfaces in Computational Geometry, Fluid Mechanics, Computer Vision, and Materials Science.* Cambridge University Press, 2002.

BA Shapiro, RA Harrison, and CA Trout. *Clinical Application of Respiratory Care.* Northwestern University Medical School, Year Book Medical Publishers, Inc, Chicago, 1982.

M. Soleimani. Level-set method applied to magnetic induction tomography using experimental data. *Research in Nondestructive Evaluation*, page 1, 2007.

M. Soleimani, O. Dorn, and W. R. B. Lionheart. A narrow-band level set method applied to eit in brain for cryosurgery monitoring. *IEEE Trans. Bio. Eng.*, page 2257, 2006a.

M. Soleimani, C. Gómez-Laberge, and A. Adler. Imaging of conductivity changes and electrode movement in EIT. *Physiol. Meas.*, page S103, 2006b.

M. Soleimani, W. R. B. Lionheart, and O. Dorn. Level set reconstruction of conductivity and permittivity from boundary electrical measurements using experimental data. *Inverse Problems in Science and Engineering*, page 193, 2006c.

M. Soleimani, W.R.B. Lionheart, and O. Dorn. Level set reconstruction of conductivity and permittivity from boundary electrical measurements using experimental data. *Inverse Problems in Science and Engineering*, page 193, 2006d.

E. Somersalo, J.P. Kaipio, M. Vauhkonen, and D. Baroudi. Impedance Imaging and Markov Chain Monte Carlo Methods. *Proc. SPIE's 42nd Annual Meeting*, page 175, 1997.

A. Tamburrino and G. Rubinacci. A new non-iterative inversion method in electrical resistance tomography. *Inverse Problems*, page 1809, 2002.

A. Tarantola. *Inverse problem theory and methods for model parameter estimation*. Society for Industrial Mathematics, 2005.

A. N. Tikhonov. Solution of incorrectly formulated problems and the regularisation method. *Dokl. Akad. Nauk SSSR*, page 501, 1963.

A. N. Tikhonov and V. Y. Arsenin. *Solutions of Ill-Posed Problems*. Winston & Sons, Washington D.C., 1977.

C. R. Vogel and M. E. Oman. Iterative methods for total variation denoising. *SIAM J. Sci. Computing*, page 227, 1996.

JB. West. Respiratory physiology, the essentials 7th ed. *Journal of Applied Physiology*, page 353, 2005.

A. Yezzi, Jr. S. Kichenassamy, A. Kumar, P. Olver, and A. Tannenbaum. A geometric snake model for segmentation of medical imagery. *IEEE Transactions on Medical Imaging*, page 199, 1997.